

Copyright
by
Maryia Halubok

2018

**The Dissertation Committee for Maryia Halubok certifies that this is the approved
version of the following dissertation:**

**Understanding and Modeling the Relationship between Solar-Induced
Chlorophyll Fluorescence, Carbon, Water, and Vegetation**

Committee:

Zong-Liang Yang, Supervisor

Robert E. Dickinson

Bridget R. Scanlon

Joanna Joiner

Jay L. Banner

**Understanding and Modeling the Relationship between Solar-Induced
Chlorophyll Fluorescence, Carbon, Water, and Vegetation**

by

Maryia Halubok

Dissertation

Presented to the Faculty of the Graduate School of The

University of Texas at Austin

in Partial Fulfillment of

the Requirements for the

Degree of

Doctor of Philosophy

The University of Texas at Austin

August 2018

Dedication

To my parents who have supported me in my endeavors,
And to my sister who has made the journey much more fun

Acknowledgements

First and foremost, I would like to extend my sincere gratitude to my supervisor, Dr. Zong-Liang Yang. I am deeply grateful for his guidance, encouragement and patience that helped me in the search of my path in science. The door to his office was always open whenever I had a question about my research, writing or ran into a trouble spot. I have thoroughly enjoyed doing and discussing research, writing, and learning about academic life under his supervision. Without his persistent help this dissertation would not have been possible.

I would like to express my appreciation to my committee members, Dr. Robert Dickinson, Dr. Bridget Scanlon, Dr. Joanna Joiner and Dr. Jay Banner, for serving on my committee as well as sharing their knowledge and opinions. I would also like to thank Dr. Lianhong Gu whose help in planning and developing my research was invaluable.

I also thank my former and current group members for their help, beneficial discussions and motivating environment they've created. Many thanks to the research and administrative staff in the department, Dr. Muhammad Shaikh, Mr. Philip Guerrero, Mr. David Spindler, and Mr. Adrian Huh.

I want to thank all my professors at UT Austin for enriching my knowledge and encouraging me to ask questions which is undoubtedly an important skill to foster for practicing scientists.

I would especially like to thank my family members for the love, support, and constant encouragement I have gotten over the years. Thank you to all my friends in Austin.

My graduate studies were financially supported by funds from the Jackson School of Geosciences at the University of Texas at Austin and ASTRO program at Oak Ridge National Laboratory. Computing resources were provided by the Texas Advanced Computing Center. The data sources are acknowledged at the end of each chapter.

Understanding and Modeling the Relationship between Solar-Induced Chlorophyll Fluorescence, Carbon, Water, and Vegetation

Maryia Halubok, Ph.D.

The University of Texas at Austin, 2018

Supervisor: Zong-Liang Yang

Abstract

Our ability to understand how global vegetation uptakes atmospheric CO₂ is crucial for closing the Earth's carbon budget and predicting feedbacks under a changing climate, but this understanding has been poor primarily due to limited observations and analyses. Recently, satellite retrievals of solar-induced chlorophyll fluorescence (SIF) have provided a highly credible opportunity to estimate gross primary production (GPP) and for monitoring droughts. Despite this exciting progress, there are limited studies on how SIF is related to precipitation, soil moisture and GPP. Ultimately, it remains unknown how SIF is emitted from vegetation canopies before it can be detected by satellites from space.

This dissertation aims to address the following questions: (1) How can SIF in conjunction with other environmental variables be used to estimate plant production?
(2) What are possible implications of SIF-based GPP for drought detecting and monitoring? How effective is SIF in capturing the onset and demise of a drought event?
(3) How can simulations of solar-induced chlorophyll fluorescence radiative transfer be improved with the use of Monte Carlo ray tracing approach and what are the advantages and limitations of

this method? Is it feasible to employ this approach in addressing issues with satellite-based SIF related to the configuration of satellites?

The main scientific findings are as follows: (1) Multiple linear regression estimates of GPP using SIF, precipitation and soil moisture and accounting for the lead–lag relationship between SIF, precipitation and soil moisture, are produced and agree well with FLUXNET flux tower data; (2) SIF is unlikely to be useful as an early meteorological drought indicator; in addition, SIF apparently does not respond to the stress conditions faster than common remotely-sensed vegetation indices (VIs); (3) The Monte Carlo ray tracing model can successfully simulate fluorescence emitted from the top of a canopy and provides useful insights into how global scale SIF satellite retrievals can be clarified.

Table of Contents

Abstract	vi
Table of Contents	viii
List of Tables.....	x
List of Figures	xi
Chapter 1 : Introduction	1
1.1 Chlorophyll Fluorescence Mechanism.....	1
1.2 SIF Satellite Retrievals	2
1.3 SIF-GPP Connection	3
1.4 Research Objectives and Outline of the Dissertation.....	4
Chapter 2 : Estimating crop and grass productivity over the United States using solar- induced chlorophyll fluorescence, precipitation and soil moisture data from space	6
2.1 Abstract	6
2.2 Introduction	7
2.3 Data and Methodology	11
2.3.1 Observational and Model Data	11
2.3.2 Framework for quantifying GPP, SIF, precipitation and soil moisture relationships	15
2.4 Results	28
2.5 Conclusions and Discussion.....	23
2.6 Acknowledgements	25
Chapter 3 : Using SIF as an indicator of drought onset and demise	38
3.1 Abstract	38
3.2 Introduction	39
3.3 Data and Methodology	42
3.1.1 Observational Data	42
3.1.2 Methodology.....	44
3.4 Results	45
3.5 Conclusions and Discussion.....	50
Acknowledgments	52

Chapter 4 : A Monte Carlo ray tracing model for simulating canopy-level emissions of solar-induced chlorophyll fluorescence.. 59

- 4.1 Abstract 59
- 4.2 Introduction 60
- 4.3 Model Description 64
- 4.4 Results 67
- 4.5 Conclusions and Discussion..... 72
- Acknowledgements 74

Chapter 5 : Conclusions and future research..... 84

- 5.1 Summary 84
- 5.2 Future Work 87

References 89

Vita 98

List of Tables

Table 2.1 Table 2.1. Basic information regarding the FLUXNET sites used in this study	14
Table 3.1 Days of drought onset and demise as inferred from rainfall, SIF and NDVI	50

List of Figures

Figure 1.1 Idealized Jablonski diagram illustrating the electronic states of chlorophyll *la* molecule and the transitions between them..... 1

Figure 2.1 Percentage of C3 non-arctic grasses (PFT 13 in CLM) (a), crops (PFT 15) (b), and their combination (c) over the contiguous US. PFT maps were derived from the 1-km IGBP (International Geosphere-Biosphere Program) DISCover dataset and the 1-km University of Maryland tree cover dataset (Bonan et al. 2002). This PFT product is modified by re-labeling the IGBP classes of MODIS Land Cover Type 1 product. Red dots indicate FLUXNET station locations..... 27

Figure 2.2 Lead–lag correlation between SIF and precipitation (top row), precipitation and soil moisture (middle row) and SIF and soil moisture (bottom row) for US-Ne3 (left column) and US-KFS (right column) stations respectively. Dashed lines denote 95% confidence level..... 28

Figure 2.3 Relationship of mean monthly GPP (gC/m²/day) measured at FLUXNET stations with C3 crop vegetation (Table 2.1) used in this study and (a) GOME-2 SIF; (b) SIF-based GPP; (c) SIF- and precipitation-based GPP; (d) MLR-based GPP (SIF, precipitation, soil moisture as predictors); (e) MLR-based GPP with lead–lag. The Pearson’s correlation coefficient **R** and root-mean-square error **RMSE** are shown..... 29

Figure 2.4 Relationship of mean monthly GPP (gC/m²/day) measured at FLUXNET stations with C3 non-arctic grass vegetation (Table 2.1) used in this study and (a) GOME-2 SIF; (b) SIF-based GPP; (c) SIF- and precipitation-based GPP; (d) MLR-based GPP (SIF, precipitation, soil moisture as predictors); (e) MLR-based GPP with lead–lag. The Pearson’s correlation coefficient **R** and root-mean-square error **RMSE** are shown 30

Figure 2.5 Relationship of mean monthly GPP ($\text{gC}/\text{m}^2/\text{day}$) measured at FLUXNET stations with C4 grass vegetation (Table 2.1) used in this study and (a) GOME-2 SIF; (b) SIF-based GPP; (c) SIF- and precipitation-based GPP; (d) MLR-based GPP (SIF, precipitation, soil moisture as predictors); (e) MLR-based GPP with lead-lag. The Pearson’s correlation coefficient **R** and root-mean-square error **RMSE** are shown..... 31

Figure 2.6 Relationship of mean monthly GPP ($\text{gC}/\text{m}^2/\text{day}$) measured at US-Tw3 FLUXNET station characterized by alfalfa vegetation (Table 2.1) and (a) GOME-2 SIF; (b) SIF-based GPP; (c) SIF- and precipitation-based GPP; (d) MLR-based GPP (SIF, precipitation, soil moisture as predictors); (e) MLR-based GPP with lead-lag. The Pearson’s correlation coefficient **R** and root-mean-square error **RMSE** are shown..... 32

Figure 2.7 Relationship of mean monthly GPP ($\text{gC}/\text{m}^2/\text{day}$) measured at US-Twt FLUXNET station with rice as a characteristic plant species (Table 2.1) and (a) GOME-2 SIF; (b) SIF-based GPP; (c) SIF- and precipitation-based GPP; (d) MLR-based GPP (SIF, precipitation, soil moisture as predictors); (e) MLR-based GPP with lead-lag. The Pearson’s correlation coefficient **R** and root-mean-square error **RMSE** are shown 33

Figure 2.8 Mean total GPP ($\text{gC}/\text{m}^2/\text{month}$) within a CLM grid box surrounding US-ARM, US-AR1 and US-AR2 stations in 2007–2012. Total GPP is calculated as a sum of C3 non-arctic grass GPP, C4 grass GPP and crop GPP 34

Figure 2.9 Spatial patterns of monthly total (C3/C4 grass plus crop) predicted GPP based on SIF, precipitation and soil moisture (Equation 2.8) over Texas in summer 2007, chosen as reference year (a–c), and summer 2011 – drought year in Texas) (d–f)..... 35

Figure 2.10 Spatial patterns of monthly total (C3/C4 grass plus crop) predicted GPP (Equation 2.8) based on SIF, precipitation and soil moisture for summer

2007, chosen as reference year (a–c); summer 2011 – drought year in Texas (d–f); and summer 2012 – the Great Plains drought (g–i) 36

Figure 2.11 Gross primary production ($\text{gC}/\text{m}^2/\text{month}$) from MOD17A2 data product in summer 2007 (a–c), summer 2011 (d–f), and summer 2012 (g–i) ... 37

Figure 3.1 Mean pentad rainfall (a,c) and mean rainfall (b,d) over the Great Plains and Texas as per CPC precipitation data from 1979–2016. Rainfall is in mm/day. Dry and wet years are identified on the basis of the departure of rainfall values from multi-year mean for each individual week. The eight driest years over the Great Plains region in 1979-2016 are as follows: 1980, 1985, 1988, 1989, 2002, 2003, 2006, 2012; over Texas region: 1980, 1988, 1998, 2001, 2005, 2006, 2011, 2012. The eight wettest years over the Great Plains region are 1981, 1982, 1990, 1995, 1999, 2008, 2010, 2015; over Texas region: 1979, 1981, 1987, 1989, 1991, 1992, 2004, 2015..... 53

Figure 3.2 Mean pentad soil moisture (a,c) and mean soil moisture (b,d) over the Great Plains and Texas as inferred from ESA CCI data over the period of 1984–2014. Soil moisture is in m^3/m^3 54

Figure 3.3 Mean weekly SIF (a,c) and SIF anomalies (b,d) over the Great Plains and Texas as inferred from GOME-2 data over the period of 2007–2016 55

Figure 3.4 Mean 16-day composite NDVI (a,c) and NDVI anomalies (b,d) over the Great Plains and Texas as inferred from MODIS data over the period of 2002–2018..... 56

Figure 3.5 Hovmueller diagram showing propagation of drought-related SIF and GPP anomaly. GPP is calculated according to Equations 2.5, 2.6, 2.7, and 2.8 from Chapter 2. Rainfall is represented by contour lines with an interval of 0.5 mm/day..... 57

Figure 3. Hovmueller diagram of SIF composite (2007–2016) over the Great Plains region (a) and Texas (b). Rainfall is represented by the black contour lines with 0.5 mm/day interval..... 58

Figure 4.1 Schematic diagram showing the layout of the Monte Carlo ray tracing model presented in this study 75

Figure 4.2 Schematic diagram of calculations for satellite efficiency for fluorescence..... 76

Figure 4.3 Top view of canopy emitting fluorescent photons under different solar zenith angle conditions..... 77

Figure 4.4 Modeled top canopy fluorescence dependence on leaf angle distribution..... 78

Figure 4.5 Fluorescence emitted from the top of the canopy a) leaf angle = 0°, SZA = 75°; b) leaf angle..... 79

Figure 4.6 Schematic of photon intensity dependence of SZA and leaf angle cosines..... 79

Figure 4.7 Fluorescence emitted from the top of the spherical canopy of different size..... 80

Figure 4.8 Percentage of modeled top-of-canopy SIF as registered by satellites, assuming scan angle of 55° 81

Figure 4.9 Percentage of modeled top-of-canopy SIF as registered by satellites, assuming scan angle of 32° 81

Figure 4.10 Top-of-canopy fluorescence at z-direction cross section with leaf and solar zenith angle changing from 0 to 45°: black color indicates total modeled fluorescence (in mW/m²/nm/sr); blue color – fluorescence registered by a satellite (mW/m²/nm/sr), red color – satellite efficiency equal to the percentage of total TOC fluorescence registered by satellite..... 82

Figure 4.11 Top-of-canopy fluorescence at z-direction cross section with leaf and solar zenith angle changing from 0 to 45°: black color indicates total modeled fluorescence (in $\text{mW}/\text{m}^2/\text{nm}/\text{sr}$); blue color - fluorescence registered by a satellite ($\text{mW}/\text{m}^2/\text{nm}/\text{sr}$), red color – satellite efficiency calculated as percentage of total TOC fluorescence registered by satellite..... 83

Chapter 1: Introduction

1.1 CHLOROPHYLL FLUORESCENCE MECHANISM

Solar energy that is re-emitted at longer wavelengths after being absorbed by chlorophyll molecules in plants is commonly referred to as solar-induced chlorophyll fluorescence. Chlorophyll *a* molecules, which are very efficient in absorbing visible light, have two absorption peaks around 430 nm (blue region of spectrum) and 662 nm (red), while chlorophyll *b* peaks are slightly shifted to the green region (453 and 642 nm respectively). Upon absorption of a blue light

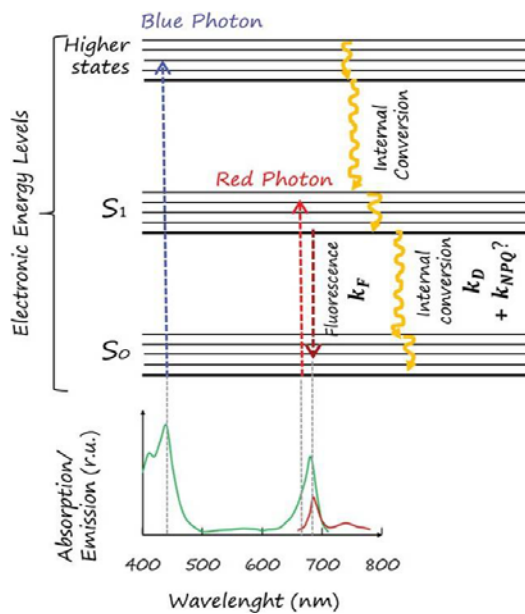


Figure 1.1 Idealized Jablonski diagram illustrating the electronic states of a chlorophyll *a* molecule and the transitions between them (Porcar-Castell et al. 2014)

photon one of the electrons in chlorophyll molecules is excited from its ground state (S_0) to the second molecular orbital (S_2). From S_2 energy is rapidly dissipated as heat by internal conversion and the electron relaxes to the first molecular orbital (S_1). In case of a photon of red light, the electron is brought to the S_1 state directly.

It is S_1 from which the excitation energy can take different paths. Intrinsically, there are three main de-excitation pathways: (1) the energy can be used to drive photochemical reactions (photosynthesis), (2) can be lost via non-photochemical quenching or undergo radiationless decay, and (3) can be reemitted as fluorescence (Fig. 1.1) (Baker 2008). Typically, only a small fraction (1-2%) of absorbed photons is reemitted as fluorescence. However, as chlorophyll fluorescence emission is linked to the other two processes, it is an exceptionally

useful indicator of the actual state of the plant photosynthetic machinery and plant physiological state in general at the leaf scale.

1.2 SATELLITE SIF RETRIEVALS

In the past few decades, chlorophyll fluorescence has been used in laboratory studies of photosynthesis (Krause and Weis 1991; Maxwell and Johnson 2000) . It has also been used in studies of the effect of nutrient stress on marine productivity (Behrenfeld and Milligan 2013). However, variable reflectance of terrestrial vegetation in the band where chlorophyll is registered has previously hindered use of this method for land photosynthesis.

Recently, with the introduction of new methods of spectroscopy, satellite-based SIF monitoring has become available. In particular, it was found out that chlorophyll fluorescence may be retrieved from high resolution spectra (≈ 0.025 nm) around 757 nm from Greenhouse gases Observing SATellite (GOSAT) (Frankenberg et al. 2011). In addition to GOSAT mission, other satellite instruments such as the Global Ozone Monitoring Experiment 2 (GOME-2) (Joiner et al. 2013), the Orbiting Carbon Observatory 2 (OCO-2) (Frankenberg et al. 2014; Sun et al. 2017a; Sun et al. 2017b), and the SCanning Imaging Absorption spectromETER for Atmospheric CHartographY (SCIAMACHY) (Joiner et al. 2012), have been used to measure solar-induced chlorophyll fluorescence on the global scale.

Satellite-based SIF measurements are possible with the use of several retrieval strategies employing absorption features within the Earth's reflected spectrum. Such approaches are based on the use of strong absorption lines caused by telluric atmosphere absorption (Meroni et al. 2009) and the Fraunhofer lines of solar spectrum (Joiner et al. 2011; Plascyk and Gabriel 1975). Due to the existence of these features, retrieval of SIF from remotely-based hyperspectral measurements was enabled (Meroni et al. 2009). Kohler et al. (2015) presented a linear approach to SIF retrieval

on the example of GOME-2 and SCIAMACHY data: the details of the solution for the number of principal components were changed, while methodology comparable to those of Guanter et al. (2013) and Joiner et al. (2013) is being employed. It is also to be noted that although currently space-based SIF retrievals are based on capturing the far-red fluorescence signal, combined usage of far-red and red fluorescence might provide a further insight into water stress effect on vegetation and canopy structure importance for far-red fluorescence signal, among other applications (Joiner et al. 2016).

1.3 SIF-GPP CONNECTION

In order to better close the Earth's carbon budget we need to know when, where and how carbon dioxide is exchanged between the atmosphere and land. Thus, gross primary production (GPP), which is defined as rate of carbon fixation through the process of vegetation photosynthesis, is an important parameter for carbon budget and climate change research. Several studies have demonstrated that GPP constitutes the largest global land carbon flux (Beer et al. 2010; Zhao and Running 2010).

GOSAT measurements have confirmed that the intensity of chlorophyll fluorescence exhibits a strong linear correlation with gross primary production (Guanter et al. 2014). Hence, satellite-based SIF retrievals may provide the most directly measurable signal of ecosystem GPP. Such a strong relationship with photosynthesis and GPP is not necessarily obvious for the remotely-sensed vegetation indices (e.g., NDVI or EVI) or even more complex carbon models (Guanter et al. 2014). It was also discovered that during drought episodes (i.e. water-stressed conditions) fluorescence decreases indicating change in plant machinery efficiency while vegetation indices (NDVI, EVI) often fail to capture transition from normal to stressed state

(Daumard et al. 2010; Lee et al. 2013). Hence, changes in SIF may serve as an indicator of changes in GPP associated with episodes of stress and SIF may detect the development of stress before traditional vegetation indices become capable of capturing it.

Until recently, existing methods of quantifying GPP did not rely on fluorescence data, with the main groups of approaches being (1) meteorologically-driven land surface carbon cycle models (Friedlingstein et al. 2006; Sitch et al. 2008); and (2) remote sensing data-driven models focusing on GPP or NPP (Beer et al. 2010; Jung et al. 2011). However, GPP estimates produced by such models are prone to large uncertainties (Wagle et al. 2016). As solar-induced chlorophyll fluorescence and GPP are related by the chlorophyll *a* absorption in the plant photosynthetic apparatus (MacBean et al. 2018) and can be conceptualized in a similar way (Monteith 1972), incorporation of SIF data in calculations shows promise in providing us with more accurate GPP values. However, since GPP is influenced by a range of atmospheric, hydrological and biogeochemical factors, statistically justified inclusion of these variables along with SIF in calculations may further improve GPP estimates.

1.4 RESEARCH OBJECTIVES AND OUTLINE OF THE DISSERTATION

This dissertation includes three main chapters, followed by a conclusion chapter.

In Chapter 2, we explore the relationship of SIF, precipitation and soil moisture on one side with the gross primary production (GPP) on the other. While there is a link between SIF and GPP as previously highlighted, additional studies are required to ascertain potential of SIF in estimating GPP. We use a suite of remotely-sensed data to establish and statistically assess the connection between SIF, precipitation, soil moisture, and GPP. In Chapter 2 we evaluate the performance of

the proposed approach linking the above mentioned variables and compare the outputs against the available ground-based observations.

Chapter 3 aims to investigate applicability of satellite-based chlorophyll fluorescence for drought detection and characterization. With the use of available satellite datasets for SIF and NDVI (Normalized Difference Vegetation Index) we explore the suitability of use of both of them for the drought identification with the special attention to the drought onset, demise, and duration. We employ statistical methods to show whether changes demonstrated by SIF and NDVI in response to drought conditions are significant enough. We have also looked at how newly derived GPP values from Chapter 2 can be helpful in capturing drought effects and providing an estimate for the drought onset, end and, therefore, duration.

Chapter 4 introduces a Monte Carlo (MC) ray tracing approach for the purposes of SIF modeling on the canopy level. The presented method is based on a sequence of scattering and absorption events incurred by a photon on its path from the light source. In addition, the new model features a weighing mechanism whose implementation is aimed at preventing ‘all-or-nothing’ type of interaction between a photon packet and a canopy element, thus creating a realistic representation of photon interaction within and outside a canopy. The MC model is then used to investigate how the satellite scan angle and, correspondingly, field of view impact satellite efficiency in registering chlorophyll fluorescence.

Chapter 5 summarizes the conclusions and findings from this dissertation. This chapter ends with directions for future work.

CHAPTER 2: Estimating crop and grass productivity over the United States using solar-induced chlorophyll fluorescence, precipitation and soil moisture data from space

2.1 ABSTRACT

This study investigates how gross primary production (GPP) estimates can be improved with the use of solar-induced chlorophyll fluorescence (SIF) based on the interdependence between SIF, precipitation, soil moisture and GPP. We have used multi-year (2007–2012) datasets from Global Ozone Monitoring Experiment-2 (GOME-2), Tropical Rainfall Measuring Mission (TRMM), European Space Agency Climate Change Initiative Soil Moisture (ESA CCI SM), and FLUXNET observations from ten stations in the continental United States. Over the Great Plains and Texas, fluorescence levels lag precipitation events from about two weeks for grasses to four weeks for crops. Using these lead–lag relationships, we estimate GPP using SIF, precipitation and soil moisture data for grasses and crops over the US by applying multiple linear regression technique. GPP values estimated from our lead–lag based SIF in a CLM gridbox surrounding US-ARM, US-AR1 and US-AR2 FLUXNET stations have shown the closest possible match with the respect to the observational data from the corresponding FLUXNET crop and grass stations. Our GPP estimates also capture the drought impact over the US better than those from MODIS. During the drought year of 2011 over Texas, our GPP values show a decrease by 50-75 gC/m²/month as opposed to the normal yielding year of 2007. In 2012, a drought year over the Great Plains, we observe a significant reduction in GPP, especially in the areas of high production (with GPP>400 gC/m²/month), as opposed to 2007. Hence, estimating GPP using specific SIF-GPP relationships, and different plant functional types and their interactions with precipitation and soil moisture over the Great Plains and Texas regions can help produce more reasonable GPP estimates.

2.2 INTRODUCTION

Knowledge of how global vegetation uptakes the atmospheric carbon dioxide is crucial for understanding the Earth's carbon cycle processes. Gross primary production (GPP), which is equivalent to ecosystem gross photosynthesis, constitutes the largest global land carbon flux that maintains ecosystem functions such as growth and respiration (Al-Kaisi et al. 2009; Beer et al. 2010; Running et al. 2004). GPP is also closely related to crop yield and hence it can be considered the basis for food production supporting human welfare. Despite the model simulations to provide GPP estimates (Friedlingstein et al. 2006; Sitch et al. 2008; Sitch et al. 2003; Xu and Hoffman 2015), the lack of observational datasets and analyses limit our capability to validate these model outputs.

As drought events are projected to increase over both the US and other regions (Cook et al. 2015; Dai 2013; Sheffield and Wood 2008; Wang 2005) in future, it is important to quantify their effects on the reduction of plant productivity (Ciais et al. 2005; Zhao and Running 2010). Challenges remain due to the complexity of plant biophysical and physiological processes associated with droughts (Liao and Zhuang 2015).

Many researchers have tried to use solar-induced chlorophyll fluorescence (SIF) in studies of plant photosynthesis. As a fraction of solar energy that is re-emitted at longer wavelengths after being absorbed by chlorophyll molecules, SIF can provide information on plant functional state. As a result, SIF measurements have been used to assess changes in plant physiology associated from the stress events, both in lab- and field-scale studies (Krause and Weis 1991; Maxwell and Johnson 2000).

Over the past decade, satellite SIF retrievals have demonstrated that chlorophyll fluorescence intensity exhibits a strong correlation with GPP (Guanter et al. 2014). This high

correlation was found to hold for both natural vegetation (Frankenberg et al. 2011) and croplands (Guanter et al. 2014); in addition, it was also shown to be valid from an individual leaf level (Meroni et al. 2008) to the ecosystem level (Guanter et al. 2012). It is recognized that the relationship between SIF and GPP is mainly driven by the absorbed photosynthetically active radiation (APAR) as both SIF and GPP depend on it. In addition, the light use efficiencies for photochemistry and fluorescence are expected to co-vary in absence of other protective mechanisms' effects (Damm et al. 2010; Guanter et al. 2014). Thus, SIF might be regarded as the most direct physiology-based measure of terrestrial photosynthetic activity which can be expressed as plant production, thus, GPP.

Guanter et al. (2014) and Guan et al. (2016) have shown that the linear regression method using SIF and GPP as independent and dependent variables respectively produces reasonably good GPP estimates for croplands and grasslands over the US and Europe. These estimates are shown to produce good agreement with GPP at flux tower sites, as well as NPP based on the agricultural yield statistics provided by the US Department of Agriculture (USDA)(Wagner et al. 2012). Guanter et al. (2014) used GPP observations from FLUXNET stations over Europe and the US to derive the global crop and grass GPP estimates using a linear SIF-based equation, and it was demonstrated that data- and process-based biogeochemistry models, unlike the above mentioned SIF-based approach, tend to underestimate crop GPP by 50-75%. Given this level of success, a question remains as to whether such a linear relationship can be further improved?

Currently the mechanistic link between SIF and GPP remains unclear (Porcar-Castell et al. 2014) and such SIF–GPP relationship might vary from region to region due to local differences such as prevalent crop types and meteorological conditions. Leff et al. (2004) have demonstrated that wheat and corn are the most common crop plant over the US, while rice is a major crop in

South and Southeast Asia, mainly India and China; barley and rye are most extensively cultivated in European Russia. Moreover, temperature and rainfall conditions, which also vary over different locations, affect crop growth and development. Precipitation and its distribution are an important factor influencing plant production. For instance, over South Asia temporal distribution of precipitation is different from that over North America, with the major proportion of annual rainfall (as much as 75%) received during the summer monsoon season (Dhar and Nandargi 2003; Kumar et al. 1999). As a result, crop production will necessarily be influenced by these factors and the relationship between SIF and GPP might be different over different regions owing to these variations in meteorological conditions and crop types.

As it was shown previously, GPP is influenced by a range of atmospheric, hydrological and biogeochemical factors such as precipitation amount and soil moisture. The relationship between SIF and GPP would also reflect impacts of all other parameters that influence SIF. For example, one of the major physiological limits controlling plant functioning is water availability (Churkina and Running 1998; Nemani et al. 2003; Running et al. 2004) which translates to soil moisture availability as plants do not ingest water from the atmosphere directly. The drought-induced deficit in soil moisture causes stomatal closure and reduction in photosynthesis and transpiration which affect fluorescence yield (Baker 2008). Therefore, precipitation and soil moisture can exert significant influence on SIF and be highly correlated with it.

While it is assumed that effects of precipitation and soil moisture are implicitly included in the SIF signal, it might be needed to explore whether soil moisture and precipitation can also have an independent impact, which is not through SIF, on GPP. In such a case, it might be found out that using only SIF to estimate GPP takes into account only a fraction of the impacts that come from precipitation and soil moisture. In this study we intend to explore and investigate influence

of soil moisture and precipitation along with SIF on GPP prediction. Accordingly, we need a statistical tool to establish such dependent-independent parameters relationships. Owing to the inclusion of multiple factors as predictors, this study aims to use multiple linear regression analysis (MLR) by statistically justified inclusion of SIF, precipitation and soil moisture along with SIF. In this study, we propose to use SIF-based GPP equations constrained by local conditions; therefore, we develop equations that are pertinent to the crop and grass plant production, respectively, over the US. We focus on high crop producing areas over the Great Plains and Texas where crops, as well as grasses, are abundant.

It is also to be noted that plant water need varies with the stage of crop development. According to FAO (Brouwer and Heibloem 1986), a typical crop has four development stages, namely, initial stage, crop development, mid-season, and late season. At planting and during the initial stage crop water need is estimated at 50 percent of the crop water need during the mid-season stage (Brouwer and Heibloem 1986). During the crop development stage water need gradually increases and reaches its peak by the end of the crop development stage (Brouwer and Heibloem 1986). For grain producing crops, which are allowed to dry out or sometimes even die at the end of their life cycle, the water need in late season, when ripening and harvesting occur, drops to 25%, lower than that needed during the initial stage. The importance of water availability for a plant is such that if a water stress event occurs in a critical growth development period, the resulting crop GPP and quality later in the season will be reduced (Al-Kaisi et al. 2009). In this connection, it would be necessary to factor in precipitation and soil moisture from earlier in the season to be able to produce meaningful estimates of plant productivity at the end of the season. Therefore, in order to investigate the possibility of using SIF in conjunction with other parameters for GPP quantification, it is necessary to look into the link between the timing of a precipitation

event in the crop development season and response from the plant machinery in the late season as reflected in photosynthesis and fluorescence levels. Thus, we have tested the relationship between the GPP and precipitation and soil moisture with the inclusion of a lead–lag effect.

In this study, we propose to use datasets from FLUXNET stations for GPP, GOME-2 satellite data for SIF, TRMM 3B42 and 3B43 products for precipitation, and ESA CCI soil moisture data product for soil moisture over the period of 2007 to 2012, primarily due to the availability of GOME-2 SIF data for this period. We apply the MLR method to derive equations and estimate GPP using SIF. We also look at the lead–lag relationships between SIF and other parameters controlling SIF, namely, precipitation and soil moisture. We estimate such GPP values using SIF, precipitation and soil moisture for the crop and grass separately as the drought appeared over Texas in 2011 and the Great Plains in 2012. We did not estimate GPP for other vegetation types such as mixed forests along the East Coast or shrublands over the Southwestern US and other US regions (Dyer 2006; Mao et al. 2012).

2.3 DATA and METHODOLOGY

2.3.1 Observational and Model Data

GOME-2 (Global Ozone Monitoring Experiment-2) terrestrial chlorophyll fluorescence data product is the primary dataset being used in this study. GOME-2 provides retrievals of solar-induced chlorophyll fluorescence peaking at 740 nm which is based on the measurements from a broader spectral range of 734–758 nm (Joiner et al. 2013; Joiner et al. 2014). GOME-2 SIF data have been successfully used to obtain the plant functional states related to gross primary production (Guanter et al. 2014; Joiner et al. 2014; Sun et al. 2015; Walther et al. 2016; Yang et al. 2015). GOME-2 v25 level 3 dataset we use in this study covers time period from 2007 to 2012 and has a spatial resolution of $0.5 \times 0.5^\circ$.

TRMM (Tropical Rainfall Measuring Mission) 3B42 rainfall data will be further used to quantify the relationship between SIF, precipitation, soil moisture, and GPP. TRMM 3B42 and 3B43 gridded estimates are on a spatial resolution of $0.25 \times 0.25^\circ$ in the belt extending from 50°N to 50°S . We will also use TRMM 3B43 monthly precipitation based on 3-hourly rainfall estimates summed for the calendar month with rain gauge data applied for large-scale bias adjustment. In this study TRMM 3B43 product is used to produce SIF predictions based on dependence between SIF and precipitation.

In order to provide information on soil moisture impact on SIF and GPP, we have used the ESA CCI SM combined daily dataset (1978–2014) at $0.25 \times 0.25^\circ$ spatial resolution. This dataset represents the most comprehensive global time series of satellite based soil moisture applicable at up to top 5 cm of the soil. The CCI Soil Moisture product combines passive Level 2 radiometer-based products from Scanning Multichannel Microwave Radiometer (SMMR), Special Sensor Microwave Imager (SSM/I), TMI, and Advanced Microwave Scanning Radiometer for EOS (AMSR-E) with active scatterometer-based products from European Remote Sensing satellite (ERS-1/2) and Advanced Scatterometer (ASCAT). As shown in several studies (Dorigo et al. 2012; Hirschi et al. 2014; Nicolai-Shaw et al. 2015; Pratola et al. 2015; Pratola et al. 2014), ESA CCI SM data have been successfully used for a variety of applications.

We relate GPP from FLUXNET measurements at five crop (US-Ne3, US-ARM, US-Twt, US-Tw2, US-Tw3) and five grass stations (US-KFS, US-AR1, US-AR2, US-Cop, US-Wkg) to SIF, precipitation and soil moisture (Table 2.1). Data available from FLUXNET have been extensively used in various studies investigating processes related to the exchange of CO_2 between the land surface and atmosphere (Falge et al. 2002a; Falge et al. 2002b; Jung et al. 2011; Schwalm et al. 2010; Zhou et al. 2016). It was previously demonstrated that ecosystem-level GPP can be

accurately estimated from measurements of CO₂ fluxes at eddy covariance towers (Baldocchi 2003). FLUXNET GPP values, which are calculated as a difference between total ecosystem respiration and net ecosystem exchange, are obtained at a half-hourly step and expressed in $\mu\text{mol}/\text{m}^2/\text{s}$; therefore, we have converted GPP measurements to $\text{gC}/\text{m}^2/\text{day}$ and $\text{gC}/\text{m}^2/\text{month}$ that are the units used throughout this study.

GPP data are also available from MODIS, a key instrument onboard Terra (originally EOS AM-1) satellite which started providing global GPP products in 2000 (Zhao et al. 2005). We use monthly MOD17A2 data product available at 1×1 km spatial resolution. The primary purpose of including these data into analysis is using them as a reference to evaluate the performance of SIF-, precipitation- and soil moisture-based GPP estimates.

MODIS GPP algorithm is based on the light use efficiency (LUE) concept (Monteith 1972), according to which:

$$GPP = PAR \times FPAR \times LUE, \quad (2.1)$$

$$LUE = LUE_{max} \times f(VPD) \times g(T_{min}), \quad (2.2)$$

$$FPAR = 1 - e^{-k \times LAI}, \quad (2.3)$$

where PAR is photosynthetically active radiation, $FPAR$ is fractional absorption of PAR , LUE is the efficiency with which absorbed radiation is converted to fixed carbon, $f(VPD)$ is the scalar of daily vapor pressure deficit (VPD) and $g(T_{min})$ is the scalar of daily minimum air temperature (T_{min}). Biome physiological parameters are specified with the use of a biome property look-up table (BPLUT) which was modified to agree with GPP derived from flux towers and synthesized net primary production (NPP) (Zhao and Running 2010).

Table 2.1. Basic information regarding the FLUXNET sites used in this study.

	Site name and code	State	Latitude (°N)	Longitude (°E)	Land cover	Available period
1	ARM Southern Great Plains site- Lamont (US-ARM)	OK	36.61	-97.49	CRO	2003–2012
2	ARM USDA UNL OSU Woodward Switchgrass 1 (US-AR1)	OK	36.42	-99.42	GRA	2009–2012
3	ARM USDA UNL OSU Woodward Switchgrass 2 (US-AR2)	OK	36.64	-99.60	GRA	2009–2012
4	Corral Pocket (US-Cop)	UT	38.09	-109.39	GRA	2001–2007
5	Kansas Field Station (US-KFS)	KS	39.06	-95.19	GRA	2007–2012
6	Mead - rainfed maize-soybean rotation site (US-Ne3)	NE	41.18	-96.44	CRO	2001–2013
7	Twitchell Corn (US-Tw2)	CA	38.10	-121.64	CRO	2012–2013
8	Twitchell Alfalfa (US-Tw3)	CA	38.12	-121.65	CRO	2012–2013
9	Twitchell Island (US-Twt)	CA	38.11	-121.65	CRO	2009–2014
10	Walnut Gulch Kendall Grasslands (US-WKG)	AZ	31.74	-109.94	GRA	2004–2014

While MODIS algorithm provides spatial patterns of GPP reasonably well and captures its temporal variability across various biome types (Gitelson et al. 2012), accurate GPP estimates over certain biomes are still difficult to achieve (Heinsch et al. 2006; Turner et al. 2005; Turner et al.

2006). Recently, it was demonstrated that standard MOD17 GPP product substantially underestimates GPP over croplands (Wagle et al. 2015; Wagle et al. 2016; Zhu et al. 2016), especially in summer, which is likely due to the prescribed LUE being too low (Heinsch et al. 2006; Wagle et al. 2014).

One limitation of MOD17 product is related to the fact that it does not take into account the influence exerted on the photosynthetic capacity and consequently GPP estimation by leaf quality expressed as photosynthetic rate of an individual leaf (Zhang et al. 2017).

Newly available GPP products such as Vegetation Photosynthesis Model (VPM) (Zhang et al. 2017) and FLUXCOM (Jung et al. 2017) can potentially serve as better benchmarks for comparison of GPP estimates and might be used for future research.

2.3.2 Framework for quantifying GPP, SIF, precipitation and soil moisture relationships

As stated in the introduction section, precipitation and soil moisture influence both SIF and GPP. Therefore, in order to avoid the replication of soil moisture and precipitation effects in SIF and GPP, we have turned to the multiple linear regression (MLR) analysis.

We have used the multiple linear regression method to estimate relative importance of fluorescence, precipitation and soil moisture for GPP. Multiple linear regression is a technique widely applied in the atmospheric sciences (Fourty and Baret 1997; Soukharev and Hood 2006). Multiple regression is an extension of linear regression with two or more predictor variables. It is also known to take into account interdependence between independent parameters by regulating the weights assigned to them. Coefficients of independent parameters can be high but negative depending on the relationships between them (Chakraborty et al. 2015). This is due to the fact that the parameters can have a strong correlation with GPP while being not totally independent. MLR

accounts for this interdependence so that the impacts from precipitation and soil moisture are not replicated in SIF and GPP.

The multiple linear regression equation is as follows:

$$Y = b_0 + b_1x_1 + b_2x_2 + \dots + b_px_p, \quad (2.4)$$

where Y is the predicted or expected value of the dependent variable, x_1 through x_p are p distinct independent or predictor variables, b_0 is the value of Y when all of the independent variables (x_1 through x_p) are equal to zero, and b_1 through b_p are the estimated regression coefficients (Garofalo et al. 2016). To derive the equations, we use weekly averaged values of precipitation, SIF, soil moisture, and FLUXNET GPP in order to have a larger number of data points to achieve a better statistical significance. A predictor contributing the most to the equation is automatically chosen at first (here, fluorescence) and then other predictors are added automatically until and unless a predictor is statistically insignificant. To validate the equations based on the regressed coefficients and y-intercept, we again used GPP data from the FLUXNET stations.

The relationship between SIF and GPP is deemed a biome-dependent one (Damm et al. 2015; Porcar-Castell et al. 2014). Therefore, we have calculated the equations separately for both grass and crop vegetation types using remotely-sensed SIF, precipitation and soil moisture data along with station-based GPP measurements. Our goal was to derive an equation that explains the relationships between the predicting parameters (SIF, precipitation, and soil moisture) and the predictant (GPP) the best in terms of standard error analysis and explained variance. Starting from a subset of one predictor (here, SIF), we have extended our analysis using a combination of two and three different predictors (for example, SIF and precipitation) to identify the subset of independent variables that maximizes the variance of GPP explained. We also tested our model

using temperature as a predictor; however, we didn't observe the model to make any significant improvement in the explained variance of GPP.

We used a fraction of our data to derive MLR equations and the rest to validate the proposed equations – namely, we chose a combination of six FLUXNET stations with the longest record to derive the model and the remaining stations to validate. This approach was selected due to the fact that not all the FLUXNET stations in this study have a record over the entire period of interest, i.e. 2007 – 2012; e.g. Twitchell corn (US-Tw2) station has available data for the period of 2 years only. Using the explained variance, analysis of the error values, and the coefficient of correlation between predicted GPP and actual GPP, the equations were derived from the FLUXNET stations with C3 crop, C3 non-arctic and C4 grasses.

While estimating GPP within each gridcell, we have multiplied GPP for grass and crop by corresponding PFT fractions from CLM to avoid an overestimation of predicted GPP. This is because the rainfall inside the grid cell is shared by different PFTs and recorded SIF is a combination of SIF emitted from different plant types. Therefore, we have multiplied the GPP equations with the grass and crop PFT fractions since grass and crop responses to SIF and precipitation are different and have been already accounted for by different coefficients obtained in the equations based on 100% grass or crop stations as stated above.

It has long been recognized that water stress produces a large effect on chlorophyll fluorescence parameters, indicating plant structural and functional damage (Mena-Petite et al. 2000). In this analysis we focused on temporal dependence between SIF, precipitation and soil moisture. As stated earlier, such relationships appear not to be simultaneous, presumably due to the fact that the water need by the plants reaches its maximum at the end of the development stage of their life cycle, whereas SIF and GPP maximize at the later stages, i.e. ripening and harvesting

during the late season. Thus, production from crops received at the late season, when ripening and harvesting take place, may not be related to the soil moisture availability during the same period. Hence, we performed lead–lag correlation analysis using the above independent variables of SIF, precipitation and soil moisture to ascertain the temporal relationship between them.

We then introduced a new method of GPP quantification, which is based on the knowledge of the lead–lag between precipitation and SIF. MLR equations quantifying GPP were formulated for crop and grass vegetation types separately and produced GPP estimates for JJA in 2007, 2011 and 2012.

Since all the equations linking GPP, SIF, precipitation and soil moisture were generated for C3 non-arctic grasses, C4 grasses and crops only, we expect the estimates based on them to be the most robust in the areas with high percentage of these vegetation types, such as the Great Plains and Texas (Fig. 2.1).

Over regions where crop and grass PFT percentage is low (such as East Coast or Southwest), our GPP estimation approach may not be accurate since we have not formulated equations for other PFTs. Therefore, we primarily investigate and evaluate the performance of MLR equations over the Great Plains. We principally focus on finding the relationships between SIF and GPP that are hypothesized to be vary for different plant types and be pertinent to similar meteorological conditions over a specific region.

2.4 RESULTS

To better understand the relationship between GPP and other parameters, we have developed an approach to estimate grass and crop GPP as the predictant and SIF, precipitation and soil moisture as the predictors using multiple linear regression analysis. We have provided GPP estimates based on the MLR equations derived for different combinations of predictors. Thus, we

have estimated correlation and root-mean-square error (RMSE) for the following cases: SIF-based GPP, SIF- and precipitation-based GPP, SIF-, precipitation- and soil moisture based GPP (MLR-based GPP). In addition to the three above cases we have looked into how SIF itself correlates with GPP.

For the final case we have explored SIF-precipitation-soil moisture relationship using the lead-lag correlation analysis. Figure 2.2 demonstrates the lead-lag relationship between precipitation and SIF, soil moisture and precipitation, and SIF and soil moisture for US-Ne3 and US-KFS stations respectively. It can be inferred from Figure 2.2 that for US-Ne3 station with the dominant crop vegetation the lag between precipitation and corresponding SIF is on the scale of 4 weeks (Fig. 2.2a), while over US-KFS station, where grass is prevalent, this lag is about 2 weeks (Fig. 2.2b). There is no significant lag between precipitation and soil moisture values for both US-Ne3 and US-KFS stations (Figs. 2.2c–2d). Similar temporal relationships between SIF, precipitation and soil moisture have also been found for the remaining FLUXNET stations used in this research.

We have obtained GPP-predicting equations separately for crop and grass because of the differences in the response of crops and grass to soil moisture and precipitation as well as the difference in plant functional types as per CLM PFT dataset. The equations for crop and grass are as follows (hereinafter, predicted GPP, or MLR-based GPP with lead-lag):

$$GPP_{crop} = PFT_{crop} \times (6.21SIF - 2.26PPT + 14.81SM - 1.01), \quad (2.5)$$

$$GPP_{C3grass} = PFT_{C3grass} \times (2.01SIF + 5.09PPT + 1.03SM - 0.02) \quad (2.6)$$

$$GPP_{C4grass} = PFT_{C4grass} \times (1.04SIF + 0.57PPT + 1.99SM - 0.02) \quad (2.7)$$

$$GPP_{predictedgrid-scale} = GPP_{crop} + GPP_{C3grass} + GPP_{C4grass}, \quad (2.8)$$

It is necessary to emphasize that plant functional type classification from CLM (Community Land Model), their percentage and spatial patterns have been used to estimate GPP over the continental US. Since crop PFT in CLM is treated as C3 vegetation and therefore total crop GPP is calculated as that of C3 vegetation, we have not performed the analysis for C4 crops.

Thereupon, we use SIF, precipitation, and soil moisture data to produce predicted GPP estimates over the Great Plains and Texas using the approach described above. Calculation of predicted GPP is only performed if and when SIF, as an indicator of the activity of plant photosynthetic machinery, is greater or equal to zero. In case of a negative SIF value it is considered equal to zero and in the process of GPP calculation and mapping GPP is regarded to be equal to zero in the areas where SIF amounts to zero.

Figure 2.3 demonstrates correlation between GPP measured at the FLUXNET stations with C3 crop vegetation and GPP calculated with the use of the above mentioned five combinations of predictors. Such correlations are based on GPP values derived and estimated over the entire vegetation period of a year for 2007–2012. It can be noted that correlation coefficient R increases with the addition of predictor parameters while RMSE shows an opposite tendency, which is expected. While correlation coefficient seems to be increasing rather monotonically as more predictors are added, the most significant rise in R is noted when MLR equation is enhanced by the introduction of lead–lag (Fig. 2.3d, 2.3e) – R grows from 0.82 to 0.98

Figure 2.4 illustrates changes in the tightness of correlation between FLUXNET GPP and C3 grass GPP calculated with the use of the same methods as in Figure 2.3. Similarly to Figure 2.3, calculated GPP estimates and FLUXNET GPP become more significantly correlated as the independent variables are introduced; it is also shown that initially correlation between SIF and FLUXNET GPP without any ancillary data is relatively high ($R = 0.77$, Fig.2.4a) while that for

the case of C3 crops was only 0.65. Similar pattern of increasing correlation and decreasing RMSE is also characteristic for C4 grasses (Figure 2.5).

Overall, GPP estimates derived with the use of MLR along with taking the lead-lag relationship into consideration are close to those from FLUXNET network: at the crop stations peak mean monthly GPP can be up to 20 gC/m²/day while for the grass sites mean monthly GPP does not exceed 10 gC/m²/day. These findings agree well with those reported by Guanter et al. (2014).

We have also explored how inclusion of lead-lag into relationship between predictors influences GPP estimates for individual plant species. Alfalfa and rice, both C3 crop species grown at the non-rotational US-Tw3 and US-Twt stations, have been selected for this purpose. Figures 2.6a and 2.7a reveal that correlation between SIF and flux tower GPP estimates demonstrate moderate strength of relationship (0.57 and 0.41 for alfalfa and rice, respectively). It can be seen that for the rice station addition of precipitation into the equations has a substantial role in the improvement of the correlation between MLR GPP estimates and respective FLUXNET GPP values (Figs. 2.7b and 2.7c), while such change in R is not noted for alfalfa vegetation. Overall, as in the previous cases, individual plant GPP estimates demonstrate an analogous response to the introduction of more predictor variables used in MLR-based plant production quantification.

In order to provide more support for the proposed framework aimed at better MLR GPP estimation, we have calculated mean values and errors for the predicted GPP (MLR equation with lead-lag), and the reference datasets MOD17A2 GPP data product and FLUXNET GPP, within the CLM gridbox surrounding US-ARM, US-AR1 and US-AR2 stations. Figure 2.8 shows that our mean monthly (for JJA of all the years) value of predicted GPP for crop and grass within the gridbox (315 gC/m²/month) is consistent with FLUXNET stations observations

(394 gC/m²/month). Although MODIS captures the drought trend, the observed values of GPP within the gridbox surrounding the stations are only 123 gC/m²/month. This shows that our predicted (MLR-based with lead–lag) GPP estimates are the closer to plant production as inferred from FLUXNET flux tower observations.

Figures 2.9 and 2.10 show total (grass and crops combined) predicted GPP over Texas and the contiguous US respectively. Similarly, in Figure 2.11 we show GPP estimated from MODIS satellite retrievals. Figure 2.9 shows that predicted GPP over Texas (within 30–36°N/95–105°W gridbox) in the year 2011 is significantly lower than that of 2007. The area with GPP values higher than 75 gC/m²/month have decreased significantly both from 2007 to 2011 and from June 2011 to August 2011 which is not typical for a normal yielding year over both Texas and the Great Plains. Figures 2.9d–9f demonstrate that in 2011 drought conditions were limited to Texas as there was no significant change in GPP over the Great Plains (Figs. 2.10d–10f).

Figure 2.10 shows that maximum GPP values found over the Great Plains (Figs. 2.10a–10c) in the normal yielding year amount to about 500 gC/m²/month which agrees well with FLUXNET data (Guanter et al. 2014). Predicted GPP indicates that 2012 was a severe drought year over the Great Plains as compared to 2007. The impact of the drought is clearly seen in 2012 as GPP decreased significantly compared to 2007 and 2011 (Figs. 2.10g–10h). The area with GPP values greater than 400 gC/m²/month shrank to a smaller domain in 2012 over the Great Plains.

Figure 2.11 shows that MODIS GPP values are about 50% lower than those of predicted gross primary production. GPP values provided by MODIS range between 200–300 gC/m²/month over the Great Plains. However, as seen from Figures 2.11d–11f, MODIS is able to detect a drought signal over Texas in 2011 and that over the Great Plains in 2012 (Figs. 2.11g–11i). MODIS observations also provide evidence of no reduction in GPP over the Great Plains in 2011.

Moreover, MODIS GPP over the Great Plains in August 2011 was higher than that in August 2007 and is consistent with our trend in predicted GPP (Figs. 2.10c and 2.10f). Thus, our predicted GPP agrees well with MODIS produced values in terms of capturing the drought conditions effect on plant production.

2.5 CONCLUSIONS AND DISCUSSION

To our knowledge, this is the first study that quantitatively assesses the lead-lag relationship between SIF, precipitation and soil moisture. In this study, we have also derived separate equations quantifying relationships between SIF and GPP based on the differences in grass and crop plant functional types and taking into account precipitation and soil moisture conditions over the contiguous US. Our results demonstrate that GPP values based on various combinations of predictors tend to have lower correlation coefficient and higher RMSE until and unless lead-lag relationship between the mentioned predictors is considered. We believe this is primarily due to the discrepancy between crop water need timing and the period of maximum productivity. Since a plant is most vulnerable to water stress in the development period and water demand is the highest at this stage, we expect that plant production at the end of the season would depend on precipitation and soil moisture during development rather than at ripening and harvesting stages when water demand reaches its minimum. Thus, we expect a lead-lag relationship between precipitation and soil moisture on one side and GPP and SIF on the other.

Our results indicate that SIF lags rainfall and soil moisture by about 4 weeks for the crops and 2 weeks for grasses. We calculated GPP using the lead-lag relationship between SIF, precipitation, soil moisture and GPP (Equations 2.5, 2.6, 2.7, and 2.8). Mean monthly GPP value calculated for JJA in 2007–2012 with the use of predicted SIF is $315 \text{ gC/m}^2/\text{month}$, which is comparable to the FLUXNET measurement of $394 \text{ gC/m}^2/\text{month}$. At the same time, reference

MODIS dataset demonstrates a tendency to underestimate GPP: mean monthly GPP value is only 123 gC/m²/month which is approximately 50% lower than GPP estimates produced by the MLR approach and those provided by the flux tower station in FLUXNET network.

It is viable that consideration of plant water uptake properties ahead of the late season is instrumental in providing meaningful estimates of plant production. Thus, our study significantly advances understanding of satellite retrieved SIF and its relationship with precipitation and soil moisture, all of which influence plant productivity. This study is the first to demonstrate that incorporation of plant physiological variations associated with water demand at different stages of its lifetime can play an important role in the relationships that we want to understand, such as that of SIF and GPP.

Tendencies in GPP based on the predicted SIF and considering the lead–lag relationships also capture the drought trends successfully and are consistent with the observational trends from MODIS (Fig. 2.11). We found that in 2011 predicted GPP over Texas is typically approximately 50–75 gC/m²/month lower than in a normal yielding year of 2007. Over the Great Plains such departure is comparable to this over Texas and the area with production greater than 400 gC/m²/month is reduced significantly in July and August 2012.

This study supports the claim that relationships between SIF and GPP are different for crops and grasses; using the statistically justified inclusion of regional precipitation and soil moisture, such relationships can be derived and used to improve GPP estimates and drought trend detection. Our results indicate that GPP values based on multiple linear regression using SIF, precipitation and soil moisture as predictors are of plausible magnitude as compared to other sources represented in this study.

This study can be extended to estimate GPP for different biomes; however, the lead–lag relationship can be different for various biomes represented by different PFTs as shown in our analysis. For example, deciduous trees might exhibit more resistance to drought conditions compared to crops due to their trunk water storage, which may result in a longer delay between precipitation and fluorescence levels. Hence, there might be a different lead–lag relationship between tree growth and precipitation, which, however, warrants further analysis.

It is also important to investigate possible differences in GPP quantification related to the fact that most plants follow C3 or C4 photosynthetic pathways. For instance, as C3 plants are expected to be more sensitive to precipitation than C4 vegetation (Bi and Xie 2015), such differential plant response might need to be accounted for in further research focused on plant production.

We have performed GPP estimation and prediction and employed precipitation and soil moisture datasets pertinent to the contiguous US. Similarly, as seen from this study, FLUXNET measurements from other regions such as Europe, East and Southeast Asia, South America can be used depending on prevalent biome types, precipitation, and soil moisture content to establish such SIF–GPP relationships.

Acknowledgements

This study was supported by funds from the Jackson School of Geosciences at the University of Texas at Austin. We thank Dr. Joanna Joiner for helpful discussions and Dr. Muhammad Shaikh for assistance with CLM simulations. GOME-2 v26 level 3 SIF data are available at <http://avdc.gsfc.nasa.gov>. TRMM 3B42 and 3B43 products are obtained from <https://mirador.gsfc.nasa.gov/>. MODIS and FLUXNET GPP data are publicly available at

<https://lpdaac.usgs.gov/> and <https://fluxnet.ornl.gov/>, respectively. ESA CCI soil moisture products are provided by the European Space Agency at <http://www.esa-soilmoisture-cci.org/>.

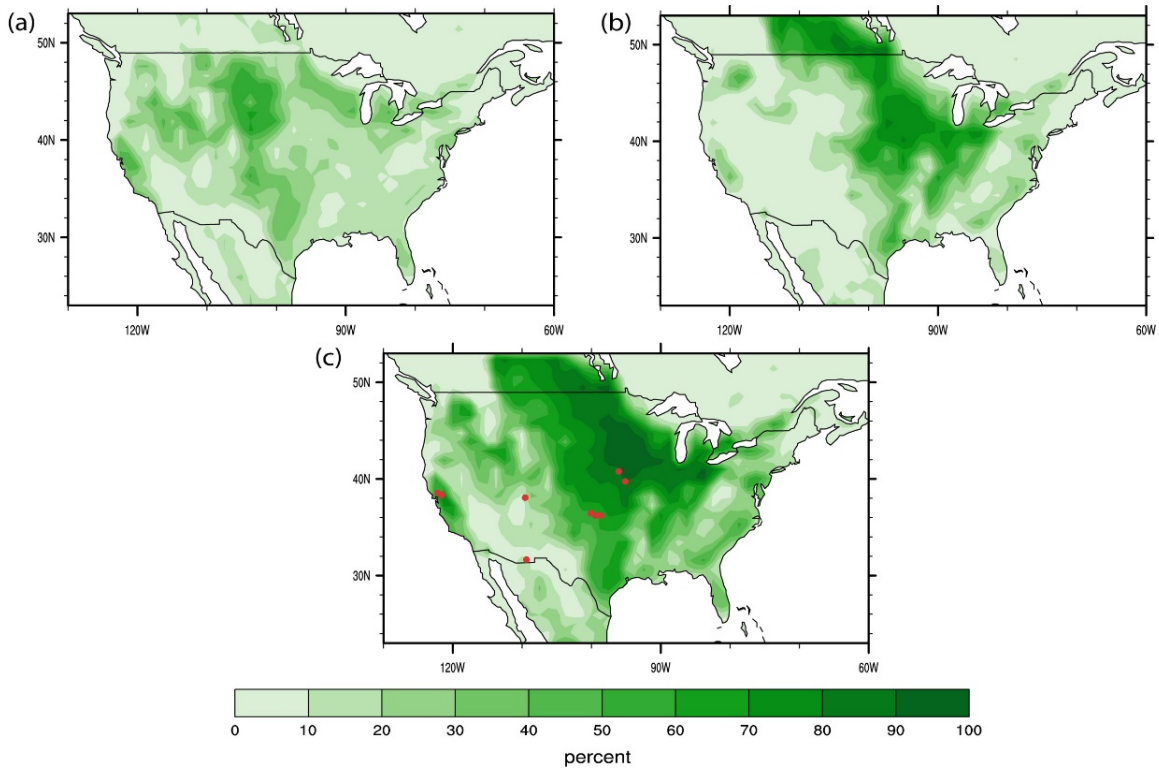


Figure 2.1 Percentage of C3 non-arctic grasses (PFT 13 in CLM) (a), crops (PFT 15) (b), and their combination (c) over the contiguous US. PFT maps were derived from the 1-km IGBP (International Geosphere-Biosphere Program) DISCover dataset and the 1-km University of Maryland tree cover dataset (Bonan et al. 2002). This PFT product is modified by re-labeling the IGBP classes of MODIS Land Cover Type 1 product. Red dots indicate FLUXNET station locations.

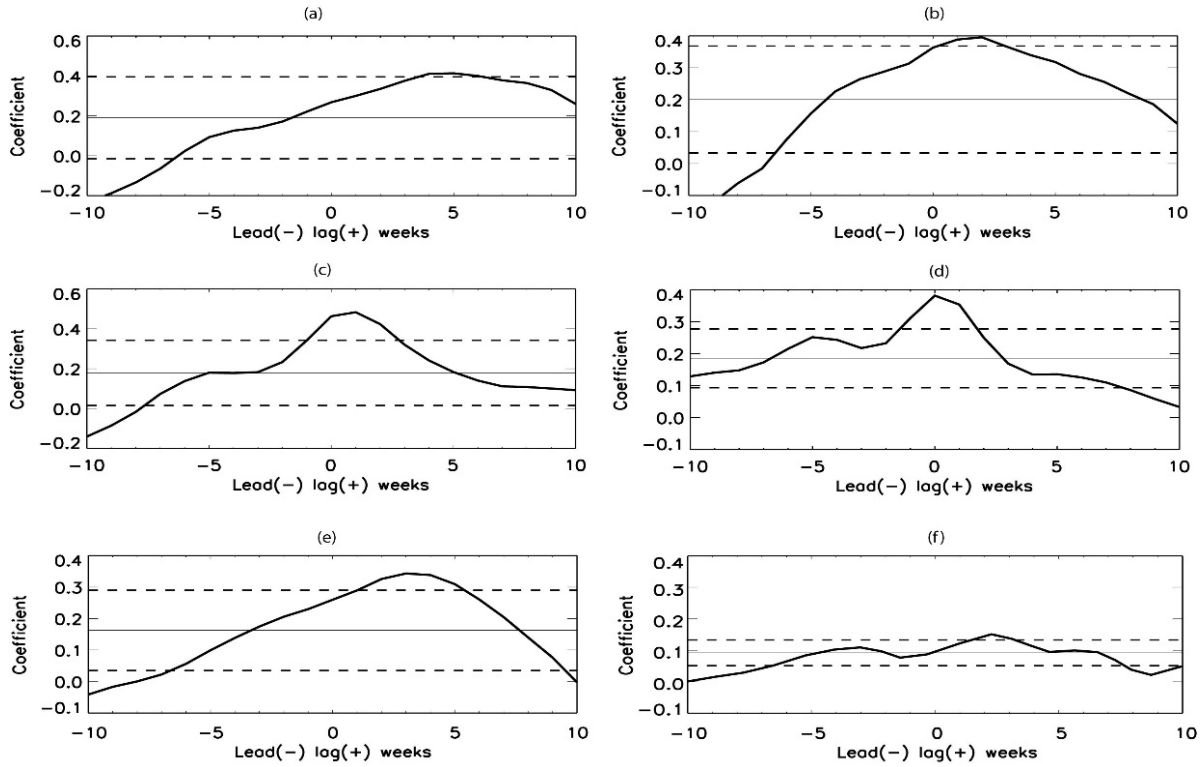


Figure 2.2 Lead-lag correlation between SIF and precipitation (top row), precipitation and soil moisture (middle row) and SIF and soil moisture (bottom row) for US-Ne3 (left column) and US-KFS (right column) stations respectively. Dashed lines denote 95% confidence level.

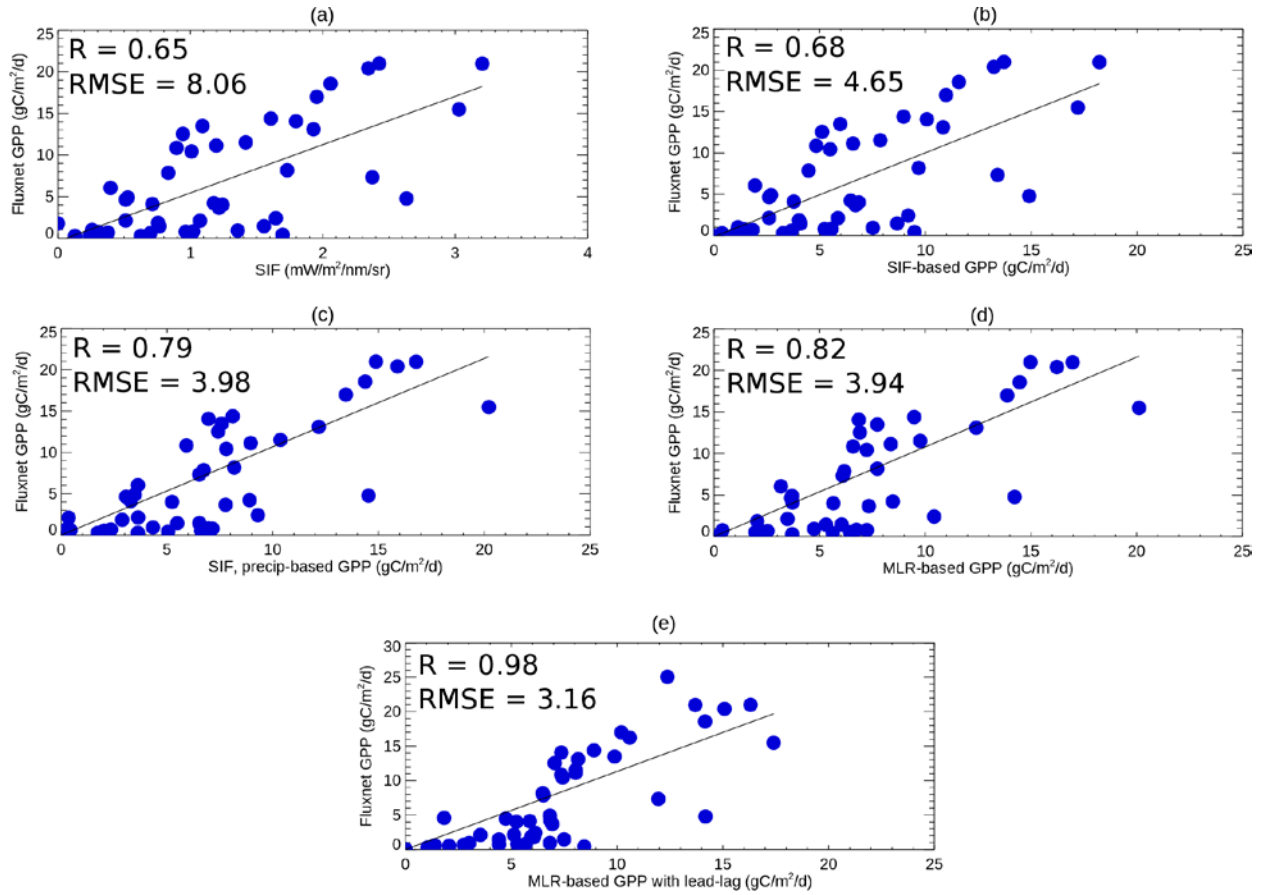


Figure 2.3 Relationship of mean monthly GPP (gC/m²/day) measured at FLUXNET stations with C3 crop vegetation (Table 2.1) used in this study and (a) GOME-2 SIF; (b) SIF-based GPP; (c) SIF- and precipitation-based GPP; (d) MLR-based GPP (SIF, precipitation, soil moisture as predictors); (e) MLR-based GPP with lead-lag. The Pearson's correlation coefficient **R** and root-mean-square error **RMSE** are shown.

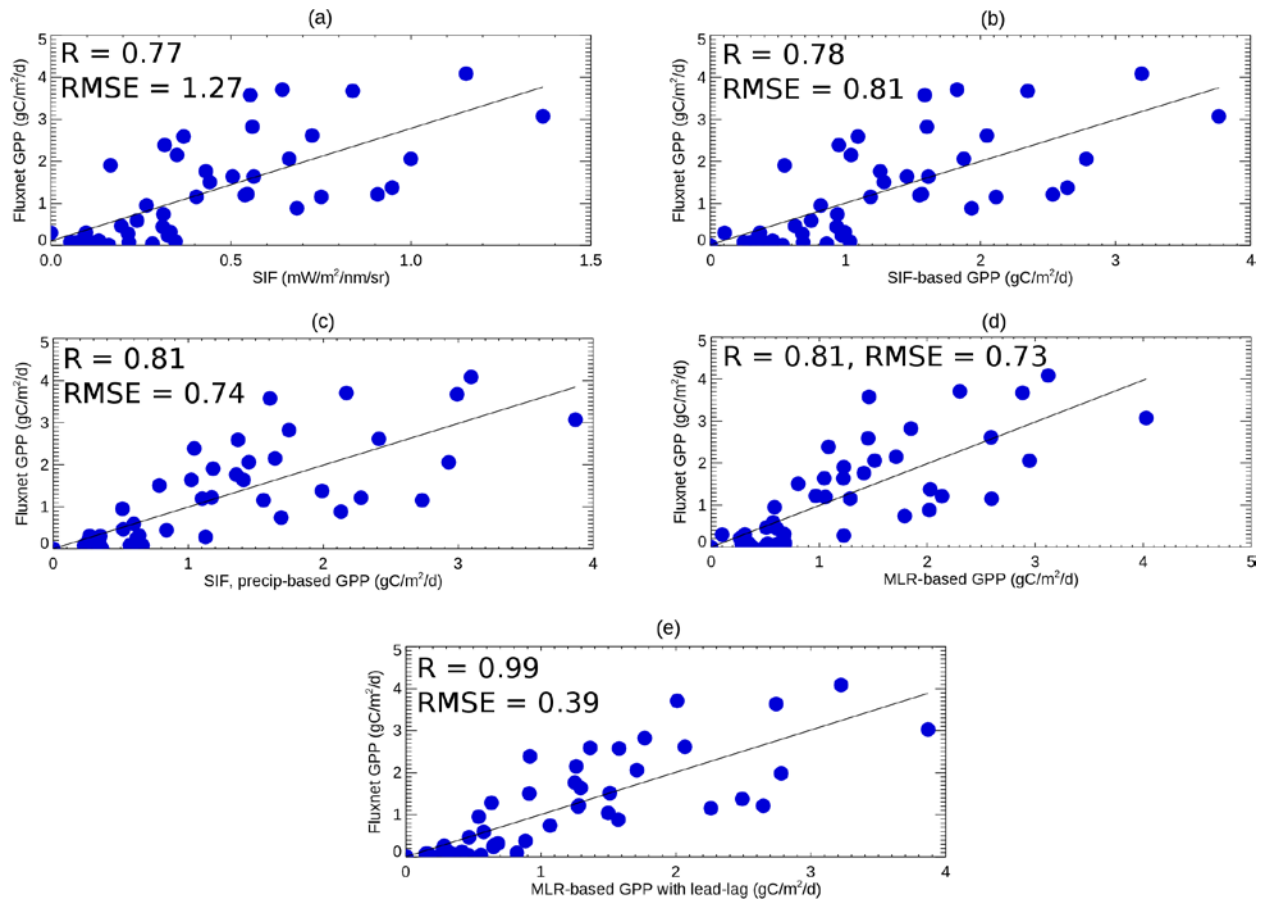


Figure 2.4 Relationship of mean monthly GPP (gC/m²/day) measured at FLUXNET stations with C3 non-arctic grass vegetation (Table 2.1) used in this study and (a) GOME-2 SIF; (b) SIF-based GPP; (c) SIF- and precipitation-based GPP; (d) MLR-based GPP (SIF, precipitation, soil moisture as predictors); (e) MLR-based GPP with lead-lag. The Pearson's correlation coefficient **R** and root-mean-square error **RMSE** are shown.

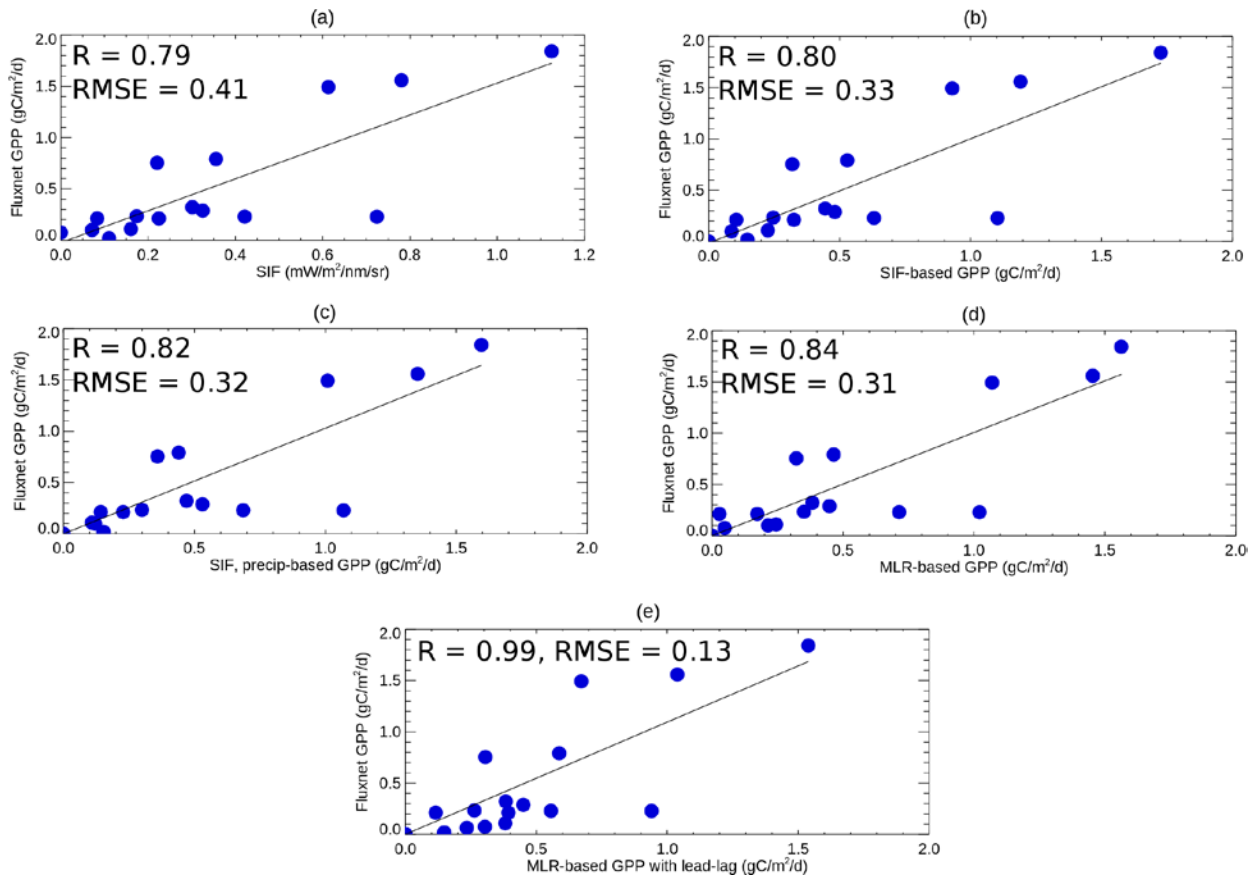


Figure 2.5 Relationship of mean monthly GPP (gC/m²/day) measured at FLUXNET stations with C4 grass vegetation (Table 2.1) used in this study and (a) GOME-2 SIF; (b) SIF-based GPP; (c) SIF- and precipitation-based GPP; (d) MLR-based GPP (SIF, precipitation, soil moisture as predictors); (e) MLR-based GPP with lead-lag. The Pearson's correlation coefficient **R** and root-mean-square error **RMSE** are shown.

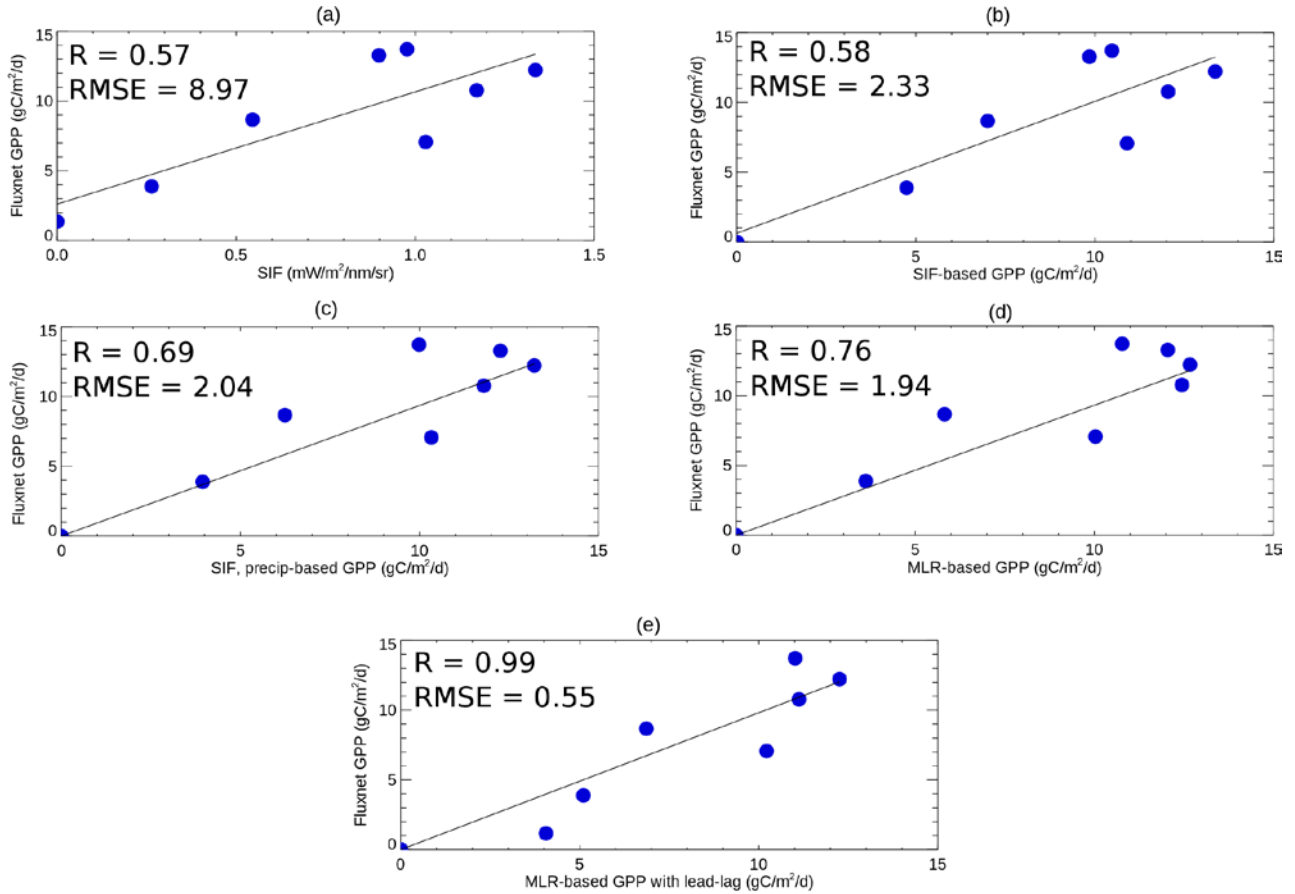


Figure 2.6 Relationship of mean monthly GPP (gC/m²/day) measured at US-Tw3 FLUXNET station characterized by alfalfa vegetation (Table 2.1) and (a) GOME-2 SIF; (b) SIF-based GPP; (c) SIF- and precipitation-based GPP; (d) MLR-based GPP (SIF, precipitation, soil moisture as predictors); (e) MLR-based GPP with lead-lag. The Pearson's correlation coefficient **R** and root-mean-square error **RMSE** are shown.

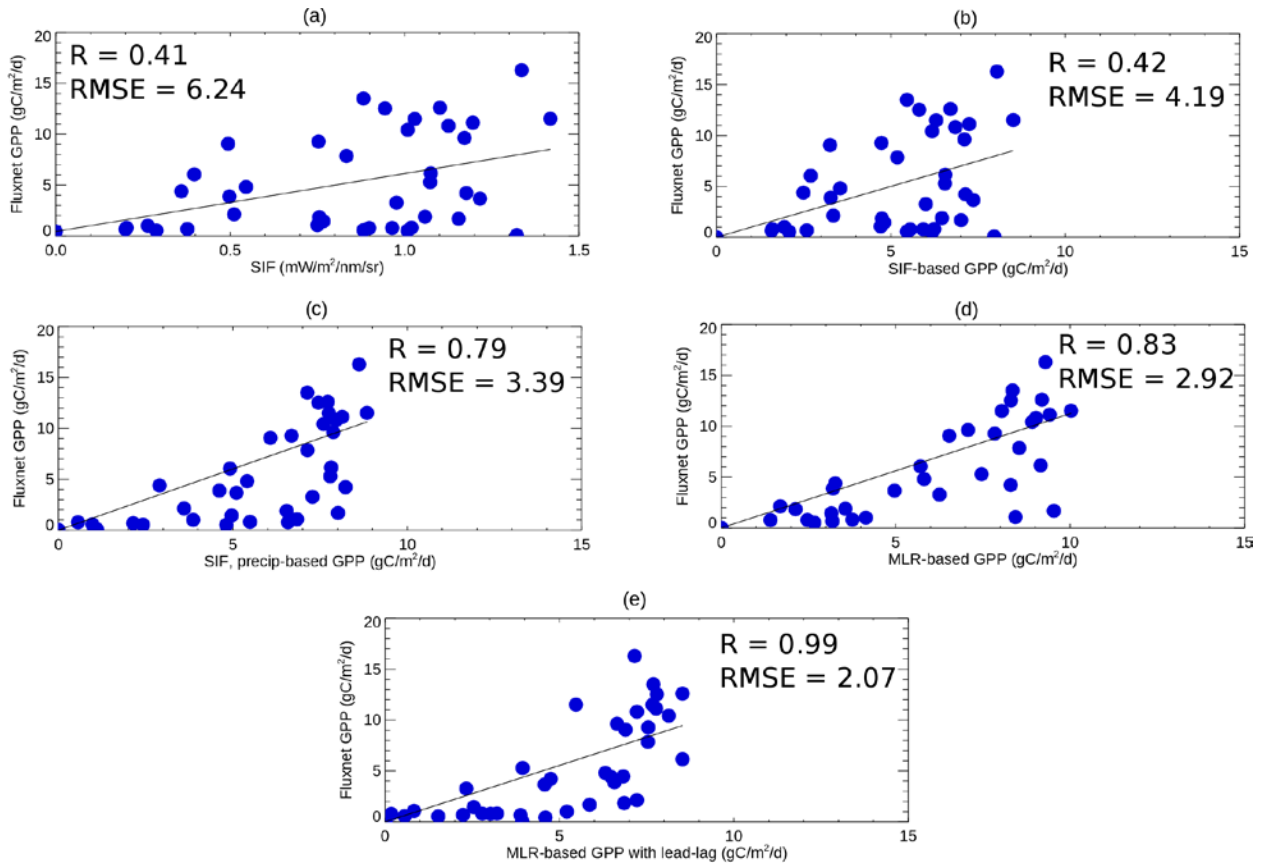


Figure 2.7 Relationship of mean monthly GPP (gC/m²/day) measured at US-Twt FLUXNET station with rice as a characteristic plant species (Table 2.1) and (a) GOME-2 SIF; (b) SIF-based GPP; (c) SIF- and precipitation-based GPP; (d) MLR-based GPP (SIF, precipitation, soil moisture as predictors); (e) MLR-based GPP with lead-lag. The Pearson's correlation coefficient **R** and root-mean-square error **RMSE** are shown.

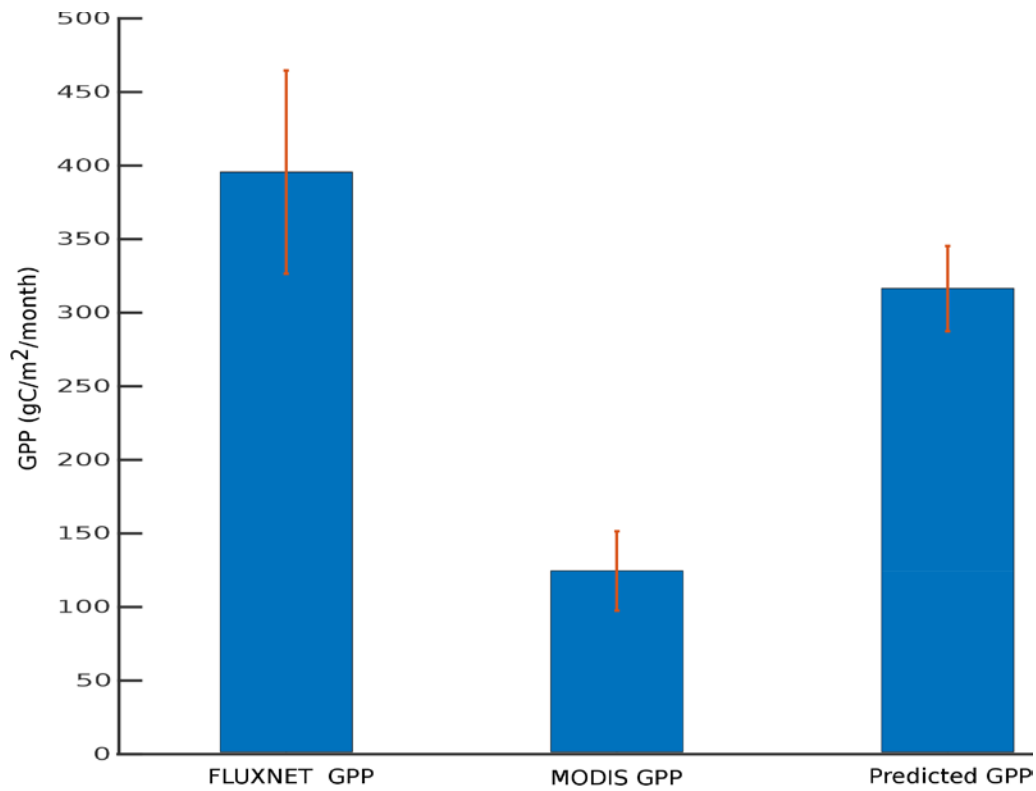


Figure 2.8 Mean total GPP (gC/m²/month) within a CLM grid box surrounding US-ARM, US-AR1 and US-AR2 stations in 2007–2012. Total GPP is calculated as a sum of C3 non-arctic grass GPP, C4 grass GPP and crop GPP.

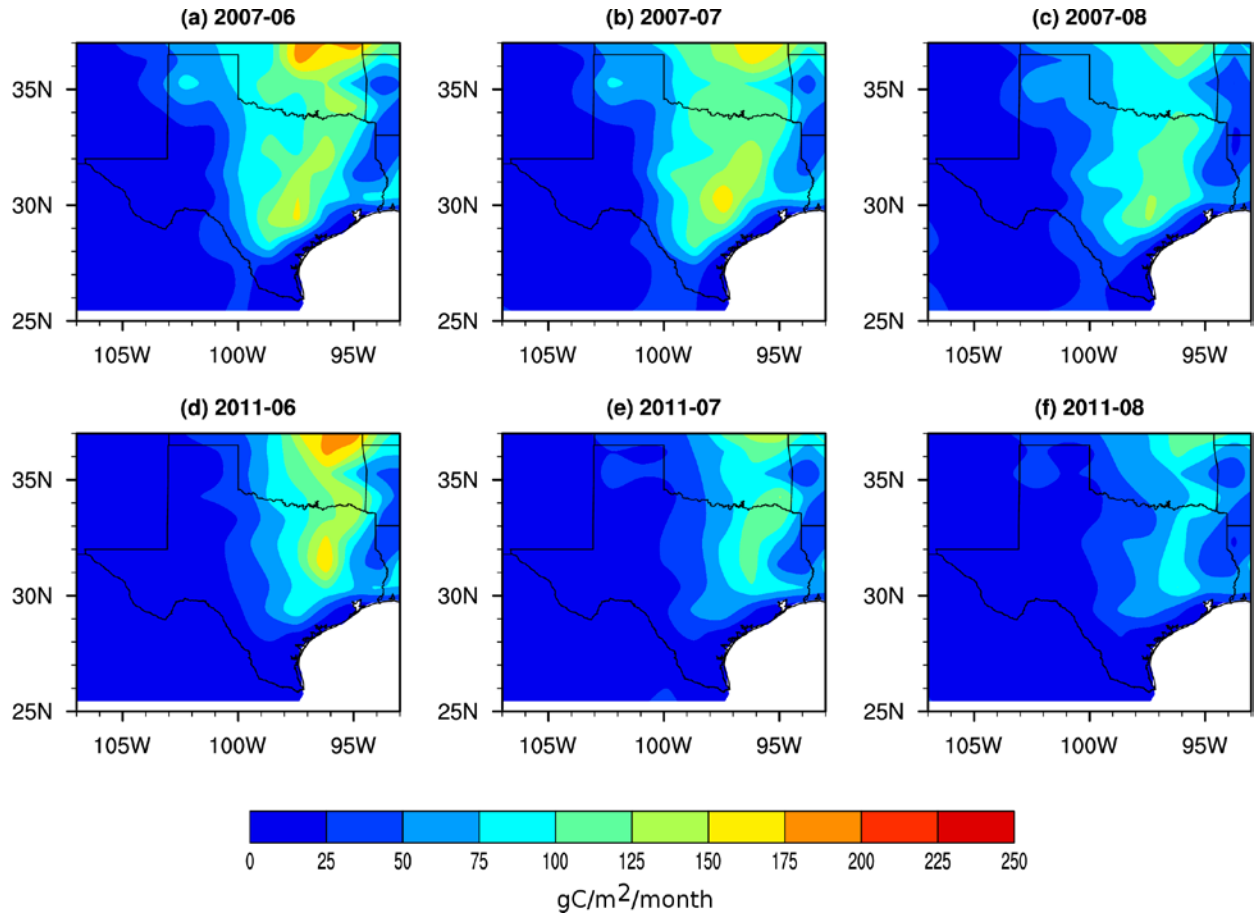


Figure 2.9 Spatial patterns of monthly total (C3/C4 grass plus crop) predicted GPP based on SIF, precipitation and soil moisture (Equation 2.8) over Texas in summer 2007, chosen as reference year (a–c), and summer 2011 – drought year in Texas) (d–f).

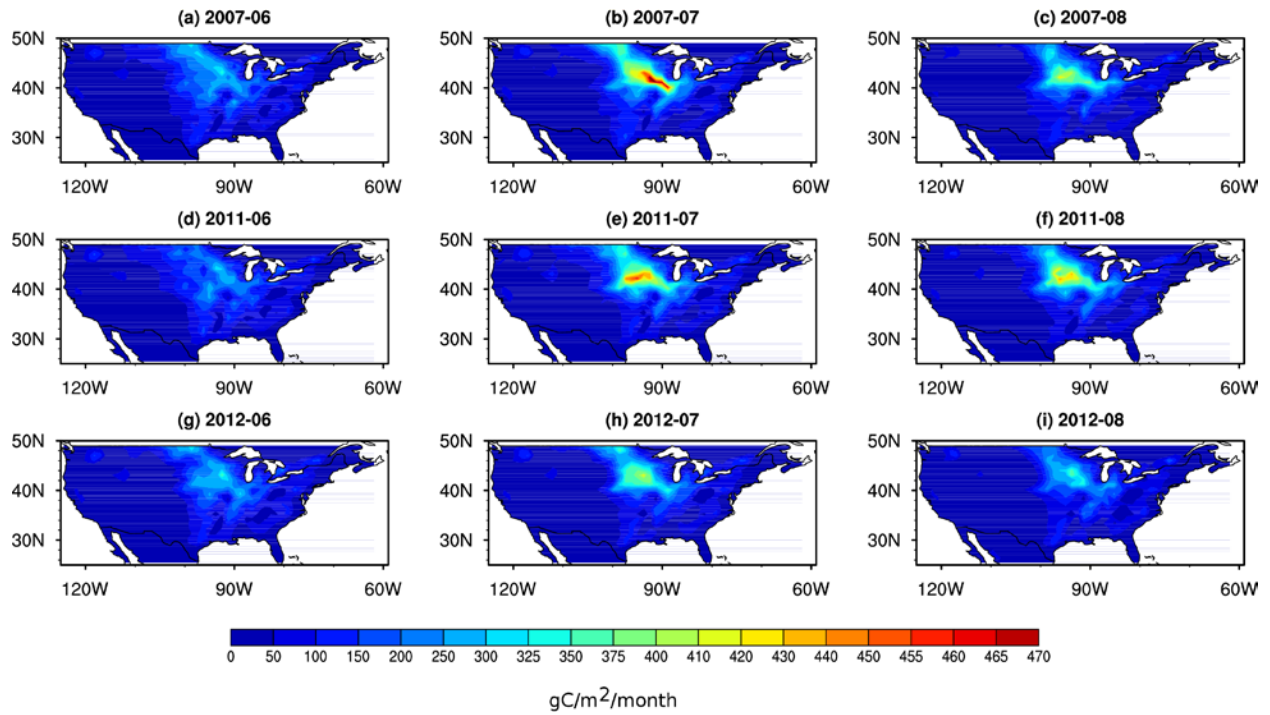


Figure 2.10 Spatial patterns of monthly total (C3/C4 grass plus crop) predicted GPP (Equation 2.8) based on SIF, precipitation and soil moisture for summer 2007, chosen as reference year (a–c); summer 2011 – drought year in Texas (d–f); and summer 2012 – the Great Plains drought (g–i).

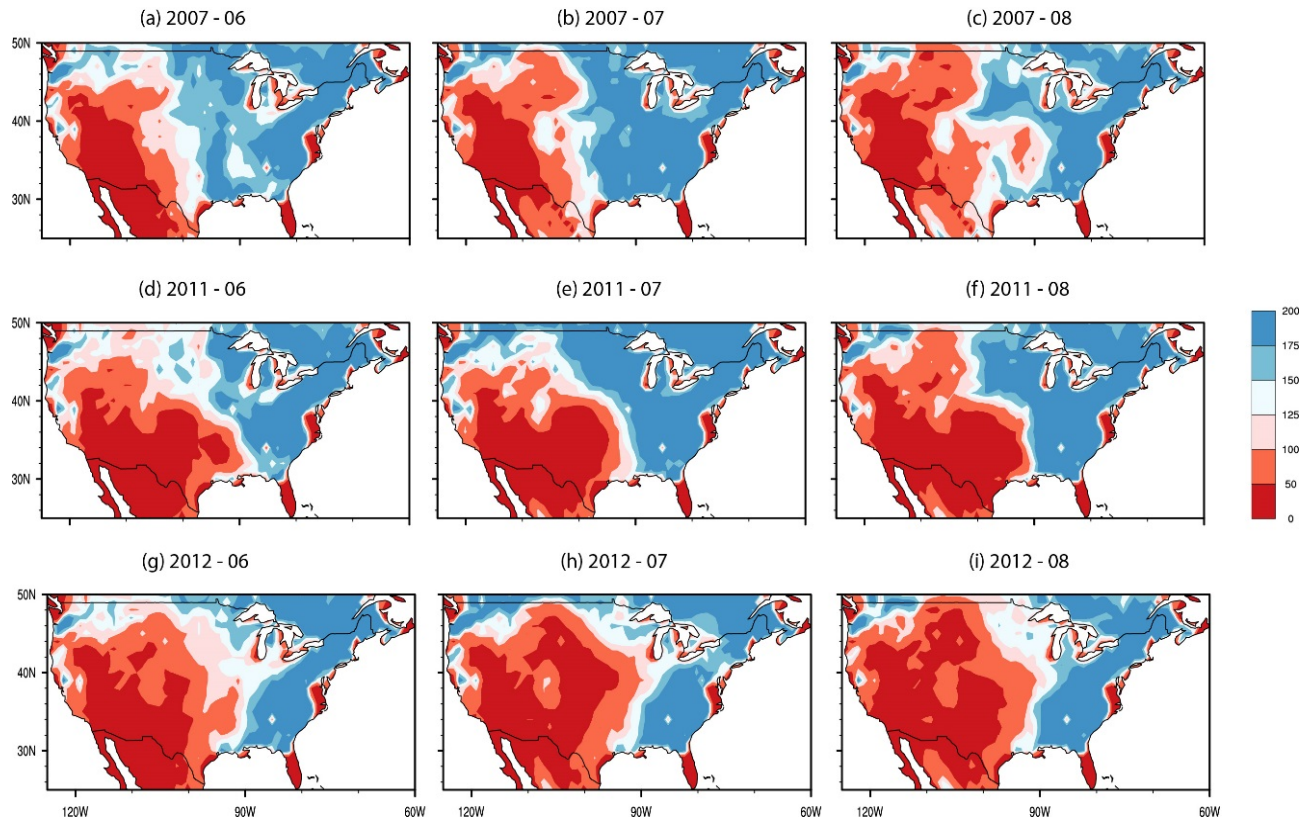


Figure 2.11 Gross primary production ($\text{gC}/\text{m}^2/\text{month}$) from MOD17A2 data product in summer 2007 (a–c), summer 2011 (d–f), and summer 2012 (g–i).

CHAPTER 3: Using SIF as an indicator of drought onset and demise

3.1 ABSTRACT

Using multiple gridded datasets from Moderate Resolution Imaging Spectroradiometer (MODIS), Global Ozone Monitoring Experiment 2 (GOME-2), and NOAA Climate Prediction Center (CPC), we investigate the suitability of using solar-induced chlorophyll fluorescence (SIF) and Normalized Difference Vegetation Index (NDVI) in identification of drought event onset, demise, and duration in the Great Plains and Texas, two regions prone to recurring droughts. Our results show that neither SIF nor NDVI is a good proxy for early meteorological drought detection. SIF lags precipitation by about a month, while NDVI shows a comparable lag. Changes in SIF during dry years show a delayed drought onset or demise as compared to the actual drought onset or demise inferred from rainfall. During the Great Plains drought in 2012 and Texas drought in 2011, precipitation is significantly lower than its climatological mean starting from day of year 135 and 140, respectively. In comparison, SIF shows that drought conditions start from day 181 over the Great Plains in 2012 and day 189 in Texas in 2011. NDVI demonstrates drought start time around day 192 and 176 for the 2012 Great Plains and 2011 Texas droughts respectively. On the other hand, soil moisture over Texas appears to be a good proxy for drought conditions as during both wet (dry) years soil moisture is shown to be higher (lower) than the climatological mean calculated on the basis of ESA soil moisture dataset. Hovmueller plots indicate that changes in SIF are more expressed over the Great Plains than Texas and lag rainfall by about one month. Our GPP estimates based on the method presented in Chapter 2 are shown to capture drought better than SIF.

3.2 INTRODUCTION

Drought is one of the most damaging climate phenomena that has profound natural, economical and societal impacts. Drought occurrence is linked to agricultural losses, water resource shortage, and other economic impacts (Livneh and Hoerling 2016). The Great Plains, a region of national agricultural importance, experienced severe drought in 2012 as per US Drought Monitor classification (Hoerling et al. 2014) that led to losses of over \$30 billion dollars and significant reduction of crop production. Texas 2011 drought, the most severe one-year drought since 1895, caused record losses of \$7.6 billion dollars accompanied by wildfires that burned almost 3.6 million acres of land (Combs, 2012).

Recently, there has been a growing concern that droughts might increase in duration, severity and frequency under changing climate conditions (Sivakumar et al. 2014; Wilhite et al. 2014). According to several studies (Cook et al. 2015; Dai 2013; Sheffield and Wood 2008), drought events are projected to increase over both the US, and Texas in particular (Banner et al. 2010), as well as the other regions. Yet, despite a long record of droughts over the US and Great Plains specifically, identification and prediction of drought development including onset, duration, demise, magnitude and spatial extent still pose a serious challenge (Hoerling et al. 2014; Seager et al. 2014). This difficulty in drought identification and forecasting might explain extensive damages and losses linked to modern-era drought events (Livneh and Hoerling 2016). One aspect to the identification problem is the absence of a clear and universally accepted definition of a drought that might add to the confusion about drought existence and its degree of severity (Wilhite et al. 2014). Drought is broadly understood as a condition of deficient moisture in the land surface and meteorological conditions associated with a drought event are known and include high temperature and substantial precipitation deficits; however, it is suggested that definitions of drought might

need to be more region and application-specific (Wilhite et al. 2014). Secondly, due to droughts being a ‘creeping phenomenon’ whose effect is accumulated over a period of time, it is often challenging to define criteria that must be met in order to identify beginning or end of drought and, therefore, precisely determine the onset, duration and end of a drought event.

A few methods have been used to quantify drought parameters and impacts, including drought indices such as Standardized Precipitation Evapotranspiration Index (SPEI), which is an extension of the widely used Standardized Precipitation Index (SPI), and Palmer Drought Severity Index (PDSI). The drought indices have proven to be a useful tool in studying droughts and their effects; however, there exist certain drawbacks related primarily to the methodology of index calculation. For example, in order to ensure comparison across climates, both SPEI and SPI rely on the selection of a univariate probability distribution (Stagge et al. 2015; Vicente-Serrano et al. 2012). In this case, selection of a proper parametric probability distribution is central to calculation of meaningful index values; otherwise, if a probability distribution is chosen improperly, significant biases might be introduced to the index values leading to minimization or exaggeration of drought effects. One more limitation of SPEI is associated with its sensitivity to the method used for calculation of potential evapotranspiration: in case of limited data availability a simple Thornthwaite method can be used while more complicated calculations including additional variables such as wind speed and solar radiation are performed if data record is long enough. The latter, more sophisticated, method is preferred; however, introduction of additional variables might impart large uncertainties. In addition, SPEI, SPI and PDSI require a long enough base period (30–50+ years) in order to adequately sample natural variability.

As agriculture is often the first and most affected sector that plays a critical role in the entire life of a given economy (Wilhite et al. 2014), it is important to evaluate and quantify drought

impact on plant health and production (Ciais et al. 2005; Zhao and Running 2010). This task remains challenging due to the complexity of plant biophysical and physiological processes associated with droughts (Liao and Zhuang 2015).

For the past couple of decades, vegetation indices (VIs), which are based on reflectance measurements in visible and near-infrared regions of spectrum, have been used in monitoring vegetation on global scale (Myneni et al. 1997). Such indices are instrumental in exploring temporal and spatial variability in vegetation state during large-scale drought events and are also useful for estimation of GPP (Running et al. 2004; Zhao and Running 2010). As VIs are indicators of the amount of green biomass within a satellite pixel, they measure potential photosynthesis or photosynthetic capacity (Yoshida et al. 2015), which makes them only an indirect marker of vegetation functioning.

In this regard, use of solar-induced chlorophyll fluorescence (SIF) might present us with an alternative method of tracking and quantifying drought effects on vegetation as well as timing of drought onset and demise. Due to its link to the photosynthetic efficiency SIF can be regarded as the one of direct indicators of the state of vegetation. SIF measurements are based on the fact that a small fraction of the solar radiation absorbed by vegetation (about 1-2%) is reemitted as fluorescence. SIF variations can provide us with useful insights into plant physiological and biochemical functions under stress conditions since in such conditions an increase in heat dissipation causes a reduction of fluorescence yield which is inevitably reflected in SIF levels. As such, fluorescence has long been used in studies of water stress influence on plant functioning. Flexas et al. (2002) have shown that under water stress conditions, a decrease in fluorescence yield was noted in C3 plants. It was also claimed that during drought episodes (i.e. water-stressed conditions) fluorescence decreased while vegetation indices, such as Normalized Difference

Vegetation Index (NDVI) and Enhanced Vegetation Index (EVI), remained unchanged (Daumard et al. 2010) , which suggests that SIF might detect the development of stress before traditional reflectance-based vegetation indices become capable of capturing it. In addition, while vegetation indices clearly tend to saturate at high gross primary production levels (Yang et al. 2015), such saturation is not characteristic for SIF. However, it is still not clear whether SIF can act as a useful indicator of drought occurrences with regard to precise timing of drought onset and demise.

In this study we focus on several scientific questions; firstly, how effective is SIF in terms of delineating drought timing and effects? How useful is SIF in terms of being an early drought predictor? What kind of insight into drought-related vegetation changes can be gained from using MLR-based gross primary production as calculated according to the method presented in Chapter 2? How is the effectiveness of SIF as an indicator of plant stress compared to that of NDVI?

In order to address the above listed questions we have used Global Ozone Monitoring Experiment 2 (GOME-2) satellite data for SIF, MOD13A2 dataset for NDVI from Moderate Resolution Imaging Spectroradiometer (MODIS), NOAA Climate Prediction Center (CPC) product for precipitation, and European Space Agency Climate Change Initiative (ESA CCI) soil moisture data over the continental US. We have studied drought propagation patterns and other characteristics with the use of Hovmueller diagrams. Also, we have tracked changes in precipitation, soil moisture, SIF and NDVI, and statistically tested the significance of such changes.

3.3 DATA AND METHODOLOGY

3.3.1 Observational Data

GOME-2 SIF, a primary dataset in this study, is retrieved by a medium-resolution nadir-viewing UV-VIS cross-track scanning spectrometer which is a part of the European

Meteorological Satellite (EUMETSAT) Polar System (EPS) MetOp mission series. The sun-synchronous orbital time at an altitude of approximately 820 km with an overpass time around 09:30 local solar time is about 100 min. The instrument was designed and launched by the European Space Agency to measure atmospheric ozone, trace gases and ultraviolet radiation; in addition, it provides retrievals of solar-induced chlorophyll fluorescence starting from 2007. GOME-2 SIF data used in this study span from 2007–2016 and have a spatial resolution of $0.5 \times 0.5^\circ$.

CPC Unified Gauge-Based Analysis of Global Daily Precipitation (hereinafter, CPC precipitation) is the first product of the CPC Unified Precipitation Project that is underway at NOAA Climate Prediction Center (CPC). In this study, it has been used as a source of precipitation data over the continental US. The quality of the data is improved by combining all information sources available at CPC and by taking advantage of the optimal interpolation objective analysis technique (Melnichenko et al. 2014). For the purposes of this study we have used $0.5 \times 0.5^\circ$ CPC precipitation data covering a time period from 1979 to 2016.

European Space Agency Climate Change Initiative Soil Moisture (ESA CCI SM) dataset is a valuable tool in providing information on soil moisture variations under drought conditions. In this study we have used the ESA CCI SM combined dataset which is based on blending active and passive products created by fusing scatterometer and radiometer retrievals respectively. For this research study, selected ESA soil moisture data product spans over 30 years (1984–2014) and provides daily global coverage of soil moisture observations at $2.5 \times 2.5^\circ$ spatial resolution.

NDVI is provided by the Moderate Resolution Imaging Spectroradiometer (MODIS) which is a key instrument onboard the Terra (originally EOS AM-1) satellite. In this study we have used 16-day composite MOD13A2 data product which has 1×1 km spatial resolution.

NDVI is calculated from the visible and near-infrared light reflected by vegetation as follows:

$$NDVI = \frac{R_{NIR} - R_{red}}{R_{NIR} + R_{red}}, \quad (3.1)$$

where R_{NIR} is the reflectance in the near-infrared (NIR) region of the spectrum, and R_{red} is reflectance in the red part of the spectrum. NDVI values are typically contained in an interval from 0 to 1 with the common range for green vegetation being from 0.2 to 0.8.

As a vegetation monitoring tool, NDVI is useful in depicting seasonal and phenologic activity, and quantifying such parameters as length of the growing season, onset of greenness, peak greenness, and leaf turnover or 'dry-down' period (Huete et al. 1994). Myneni et al. (1997) demonstrated that NDVI can be utilized for the growing season change detection and monitoring on the decadal scale. The time integral of NDVI over the growing season exhibited correlation with net primary production (NPP) (Justice et al. 1991; Running and Nemani 1988; Tucker and Sellers 1986).

3.3.2 Methodology

Our study domains include Texas region (24–36° N, 90–110° W) region and the Great Plains region (36–46°N, 90–110° W). Precipitation and soil moisture data are available on daily time scale, whereas SIF and NDVI data sets are on weekly and 16-day scales, respectively. We have first converted the precipitation data into 5-day averages (hereinafter, pentads) with the further aim of detecting the onset and demise of a dry period and calculating its length. Then, we have plotted the obtained pentad rainfall for a period of 1979–2016 to identify eight driest and wettest years. In doing so, we have estimated the May–August rainfall over two domains as stated above. Dry (wet) years are defined as years having the lowest (highest) mean summer time

precipitation (May–August). We have estimated the average rainfall of each of the pentads for the wet and dry years and compare with that computed by averaging all the years. For example, rainfall for each pentad for eight dry years is estimated as follows:

$$Px = \sum_{i=1}^8 Pxi, \quad (3.2)$$

where i is the number of dry years, x is the pentad number from 1-72, and Pxi is the rainfall of pentad number x in a year i .

Similarly, we compute the pentads of soil moisture values and compare with that of the rainfall pentads to test whether soil moisture is capable of providing an early indication of drought before rainfall. We also compute the weekly mean SIF values for the dry, wet, and all years using the same approach. For MODIS NDVI, we have used the 16-day (half-month) composites and obtained 23 half-month values each year.

We have also used the Hovmueller plots for this analysis. We have plotted rainfall, SIF, and NDVI as a function of time (either week or month) with latitude. We have averaged the parameters in the longitudinal direction in order to visualize the propagation of the dry/rainy event over the study areas. We have added composites (2007–2016) of SIF and precipitation data sets to ascertain the relationship between SIF and precipitation and use of SIF as an early drought indicator. We have performed similar calculations for the predicted GPP which was introduced previously (Section 2.4 in Chapter 2) to find out whether our produced GPP values capture any early drought signal over the Great Plains region.

3.4 RESULTS

Firstly, we have looked at the temporal characteristics of rainfall, soil moisture, SIF and NDVI. Figure 3.1 shows that the range of mean pentad rainfall values is approximately the same

for both the Great Plains and Texas, varying from about 0.5 to 4 mm/day. Figure 3.1b shows that rainfall decreases over the Great Plains region during the drought years with the strongest decrease in the year 2012. Similarly to the Great Plains, Texas shows a stronger reduction in mean rainfall over the entire domain in 2011 and 2012. Figures 3.1a and 3.1c show the mean and standard errors of pentad rainfall over all (black line), wet years (blue line), and dry years (red line). As it can be inferred from the standard error values demonstrated in Figures 3.1a and 3.1c, the departure of mean pentad rainfall from the climatological mean becomes significant around day 100 of a year, which is April 9–10 over the Great Plains, during a dry year. Over both regions, a small but significant reduction in rainfall occurs during the 20th pentad followed by a longer and strong reduction in rainfall that begins around 25th pentad (or the month of May).

Likewise, soil moisture values also show a similar trend during dry and wet years (Figs. 3.2b and 3.2d). As it can be seen in Figure 3.2, over the Great Plains there is an increase in soil moisture around the end of summer (weeks 50–65). This could be due to the excessive application of irrigated water for agricultural purposes over this region earlier in the season, especially when the rainfall during the drought is not significantly different from the all year mean (black line) during that period. Over Texas, soil moisture is significantly different during the wet years and is way above the mean value calculated for the period of 1987–2014 (black line). On the other hand, soil moisture over the Texas domain is consistently below the mean soil moisture of all the years. This suggests that soil moisture can be considered an indicator of drought occurrences over Texas. However, soil moisture variations are not particularly useful for the accurate detection of onset or demise of drought over Texas as soil moisture tends to be either consistently low or high as inferred from the ESA CCI SM data.

We have also investigated weekly SIF values over these regions. Unlike soil moisture and precipitation, SIF generally follows a seasonal patterns without substantial intraseasonal variations (Fig. 3.3). Figure 3.3b shows that SIF decreases during 2012 over the Great Plains and remains at low values in 2013. Over Texas, a strong reduction in SIF occurs in 2011 owing to the severe drought and SIF gradually increased after that. This could be due to the differences in the response of different vegetation types and species to the drought impacts. Figure 3.3a shows that SIF during the dry years become significantly different than the SIF during all years in the 24th week (or in the month of June). This shows that SIF lags the rainfall by about one month and its response to drought (as expressed by decrease in rainfall) is delayed. This could potentially be due to many factors. Firstly, soil moisture depletion does not happen instantaneously after the rainfall decreases (Figs. 3.1a and 3.2a). Secondly, air temperature in June (when SIF decreases) is much higher than that of May (when rainfall shows a reduction). According to SIF, drought begins on week 24 and ends on week 37. Both the onset and demise lag actual drought onset and demise as per rainfall. Thus, SIF might not be a suitable parameter to declare onset of a meteorological drought and calculate the duration of such a drought event over the Great Plains and Texas. Interestingly, SIF during both wet years and dry years are below SIF estimated during all the years (2007–2016), potentially in part due to the inability of vegetation to peak up after the drought ended (Fig. 3.3d). One possible explanation might lie in the fact that the categorization of dry and wet years in this study is based on the rainfall values while sensitivity of satellite-based SIF to environmental variables is complicated (Sun et al. 2015) and is indirectly related to both biotic (photosynthetic capacity, vegetation type, etc) and abiotic (CO₂ concentration, nutrient availability) parameters.

Figure 3.4 demonstrates mean 16-day composite NDVI. NDVI values over the Great Plains and Texas are not significantly different as seen in Figures 3.4b and 3.4d. 16-day NDVI during

dry, wet, and all years shows no significant difference over the Great Plains. The NDVI peak is not significantly delayed over both the Great Plains and Texas regions (Figs. 3.4a and 3.4c) as compared to SIF (Figs. 3.3a and 3.3c). Over the Great Plains NDVI demonstrates a statistically significant decrease from the multi-year mean between day 192 and day 240, while in Texas such a decrease is notable between day 176 and 224. Thus, NDVI is not a suitable parameter either to detect the onset and demise, and infer duration of a meteorological drought.

As it can be inferred from the first four figures, both SIF and NDVI are lagging behind precipitation and soil moisture in terms of indicating the start of a drought period. The delay between SIF and precipitation has been previously quantified in Chapter 2 and comprises 2 to 4 weeks depending on presence of grasses or crops, respectively.

To further understand the SIF and rainfall connection to the drought characteristics, we show Hovmueller diagrams of composite (2007–2016) SIF over the Great Plains and Texas regions in Figure 3.5. As it can be seen, seasonal increase in SIF tends to start around April and SIF reaches its maximum in late June or early July. This pattern is characteristic of the Great Plains area, possibly corresponding to the different stages of crop growth and development, e.g. as crop vegetation undergoes developmental changes and reaches the harvesting stage, it is characterized by higher photosynthesizing activity leading to higher SIF values as SIF exhibits a strong linear relationship with plant production under most conditions. The following changes are not that much pronounced for Texas which might be a result of grass being a prevalent type of vegetation in this region. Figure 3.5 also shows that changes in precipitation start occurring a month before that of SIF. Over the Great Plains region, rainfall is 2 mm/day during mid-March and 2.5 mm/day in April, whereas SIF values during the same are around 0.4 mW/m²/nm/sr and reach the peak values around 1.5 mW/m²/nm/sr in June.

We have also looked into applicability of GPP predicted on the basis of MLR relationship (Equations 2.5, 2.6, 2.7 and 2.8) developed in Chapter 2 for drought signal detection (Fig. 3.6). The Hovmueller diagrams demonstrating propagation of SIF and GPP changes are indicative of a strong negative anomaly in both SIF and predicted GPP in summer 2012 over the Great Plains region. Over Texas in 2011 there exists a small negative anomaly in SIF and GPP, which is significantly less prominent as compared to that over the Great Plains region in 2012. Both SIF and GPP are below their respective mean values of ten years (2007–2016); however, GPP shows a stronger negative change during the winter months than that indicated by SIF. It is known that dry winter anomalies might continue through the spring time and intensify as a summer drought event over Texas region (Fernando et al. 2016). Overall, changes in GPP calculated based on the MLR relationship established in the previous chapter are more expressed than those of SIF and show highly negative values during dry years.

With the use of all the parameters employed in this study, i.e. rainfall, soil moisture, SIF and NDVI, we have calculated the timing of the onset and end of drought events as inferred from the multi-year climatology (Table 3.1). These calculations were performed for “dry” and “wet” years that were defined on the basis of statistically significant departure of precipitation from a corresponding multi-year mean for each 5-day period. As seen from the table, both SIF and NDVI cannot serve as early indicators of a meteorological drought as interpreted in terms of the magnitude of precipitation shortage and duration of such shortage. Both variables demonstrate a significant lag compared to precipitation, on the scale of about one month for both SIF and NDVI. It is also demonstrated that SIF does not show significantly higher skill in detecting drought signal as compared to NDVI. For example, over Texas region as calculated from SIF from 2007–2016 and NDVI from 2002–2018 the difference in SIF and NDVI indicating the drought onset is only

one week. As expected, it is to be noted that the demise of a drought is not clearly captured either by any of the variables, which might be related to the severity of drought events in both 2011 and 2012: it might not be possible for the vegetation to recover and respond to further changes in meteorological conditions. At the same time, Sun et al. (2015) have demonstrated that under less severe drought conditions that do not lead to an irreversible vegetation damage, as precipitation and soil moisture recover, departure of the SIF signal from a multi-year mean decreases and, therefore, SIF can be seen responding to the meteorological conditions change and might be useful in characterizing drought temporal dynamics.

Table 3.1. Days of drought onset and demise as inferred from rainfall, SIF and NDVI.

Study domain	Parameter	Onset (day of year)	Demise (day of year)	Length(days)
TX	CPC rainfall	140	185	45
	GOME-2 SIF	189	235	46
	MODIS NDVI	176	224	48
Great Plains	CPC rainfall	135	215	80
	GOME-2 SIF	181	273	92
	MODIS NDVI	192	240	48

3.5 CONCLUSIONS AND DISCUSSION

In this study we aimed to take a quantitative approach in using SIF and NDVI for the purpose of drought detection. We have looked at the significance of mean pentad, weekly and 16-day composite data rainfall, soil moisture, SIF and NDVI respectively. In case a departure of mean pentad values of each variable was significant as indicated by the error bars, we have investigated how dates of drought onset and demise and, therefore, the drought duration, changed depending

on which parameter was used. It was found out that neither SIF nor NDVI responds to the drought-related changes in vegetation quickly enough to be useful as early meteorological drought indicators. The difference in timing of drought onset over Texas in 2011 and the Great Plains in 2012 as indicated by SIF and NDVI is not significant and is comparable to the temporal resolution of NDVI data product.

The lag between precipitation levels reaching a significant departure from multi-year climatology and that of SIF and NDVI is on the scale of up to 4–5 weeks. This finding agrees to a certain extent with the conclusions of Chapter 2 which claims that there exists a lead–lag relationship between a precipitation event and corresponding fluorescence levels on the scale of 2 to 4 weeks for crops and grasses respectively. It turns out that SIF reaches its highest values fairly earlier than NDVI, while SIF is peaking in late June through early July and the maximum of NDVI is found in mid-July.

GPP based on the MLR equations introduced in Chapter 2, however, proves to demonstrate a higher departure from climatology than that of SIF over the Great Plains in 2012. This potentially stems from the MLR formulation of GPP as it includes effects related to both precipitation and soil moisture in addition to SIF, when calculating plant production values.

Certain limitations exist in terms of the application of the statistical calculations; a higher number of data points would be beneficial for the purpose of getting more robust conclusions. It is important to note that years are classified as ‘dry’ or ‘wet’ on the basis of rainfall departure from its climatological mean which is calculated from record covering a period of 1979 to 2016. While statistical methods have provided us with useful insights into the timing of SIF and NDVI response to dry conditions, it is necessary to investigate the underlying physiological mechanisms of such response.

Datasets with variable temporal resolution might introduce an error to the accurate estimation of the drought onset and end dates. For example, NDVI data with a better resolution than 16 days temporal resolution can improve calculation of onset and demise dates by a couple of weeks; however, our results show that NDVI often lags rainfall by more than one month.

One more limitation of the presented research might be related to the usage of the ESA SSI soil moisture dataset. In future it is recommended to use complementary sources of soil moisture data such as Global Modelling and Assimilation Office (GMAO) soil moisture product and other soil moisture products simulated from land surface models.

Acknowledgements

This study was supported by funds from the Jackson School of Geosciences at the University of Texas at Austin. GOME-2 v26 level 3 SIF data are available at <http://avdc.gsfc.nasa.gov>. MODIS NDVI data are publicly available at <https://lpdaac.usgs.gov/>. ESA CCI soil moisture products are provided by the European Space Agency at <http://www.esa-soilmoisture-cci.org/>.

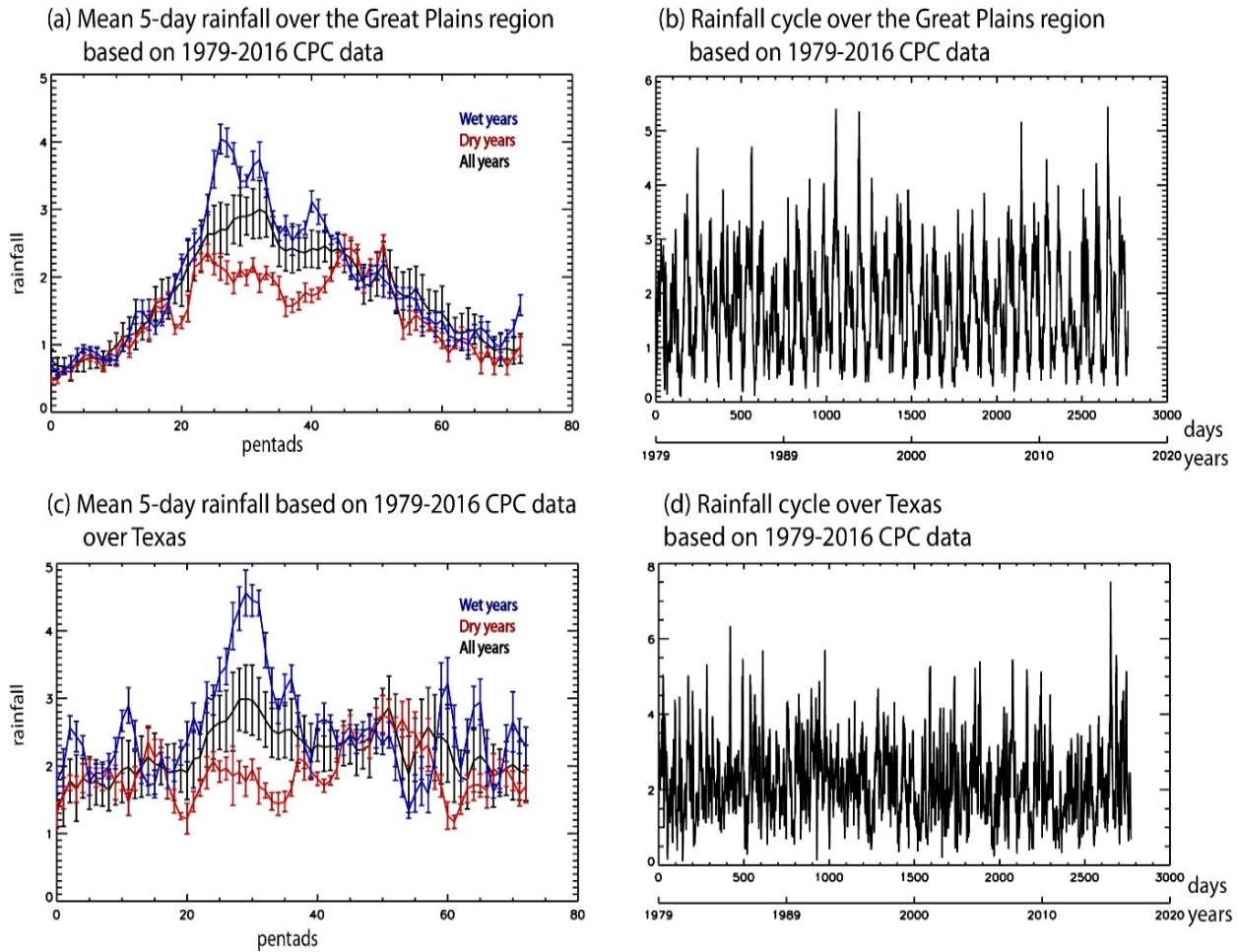


Figure 3.1 Mean pentad rainfall (a,c) and mean rainfall (b,d) over the Great Plains and Texas as per CPC precipitation data from 1979–2016. Rainfall is in mm/day. Dry and wet years are identified on the basis of the departure of rainfall values from multi-year mean for each individual week. The eight driest years over the Great Plains region in 1979–2016 are as follows: 1980, 1985, 1988, 1989, 2002, 2003, 2006, 2012; over Texas region: 1980, 1988, 1998, 2001, 2005, 2006, 2011, 2012. The eight wettest years over the Great Plains region are 1981, 1982, 1990, 1995, 1999, 2008, 2010, 2015; over Texas region: 1979, 1981, 1987, 1989, 1991, 1992, 2004, 2015.

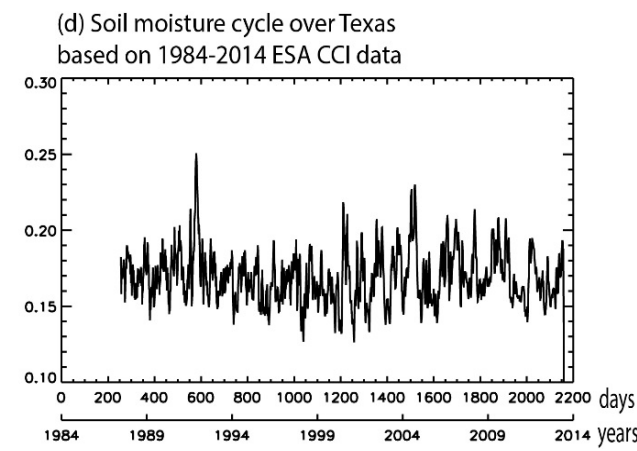
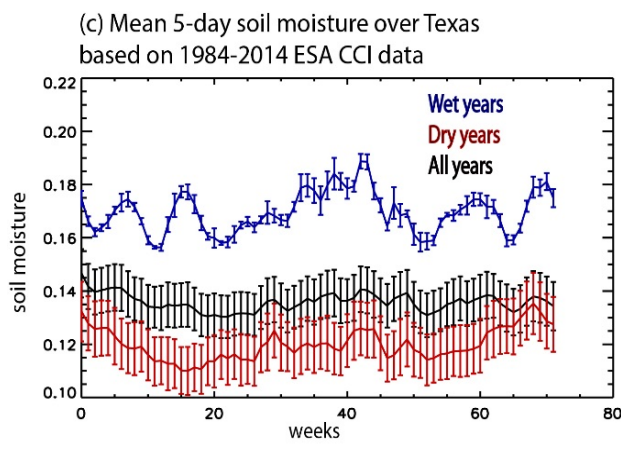
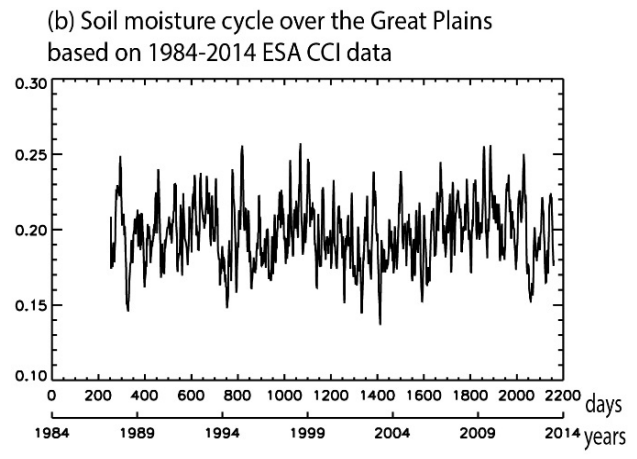
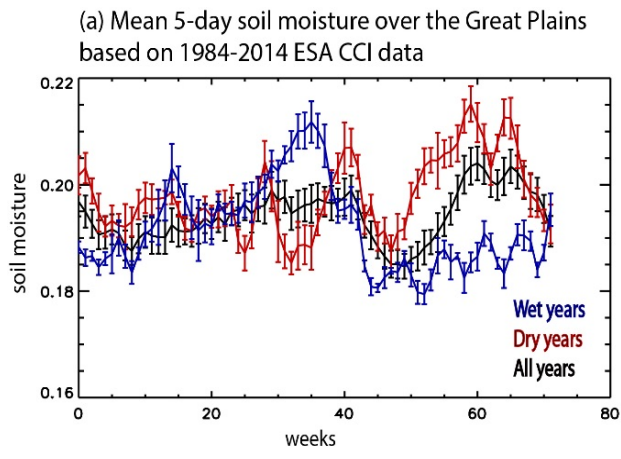


Figure 3.2 Mean pentad soil moisture (a,c) and mean soil moisture (b,d) over the Great Plains and Texas as inferred from ESA CCI data over the period of 1984–2014. Soil moisture is in m^3/m^3 .

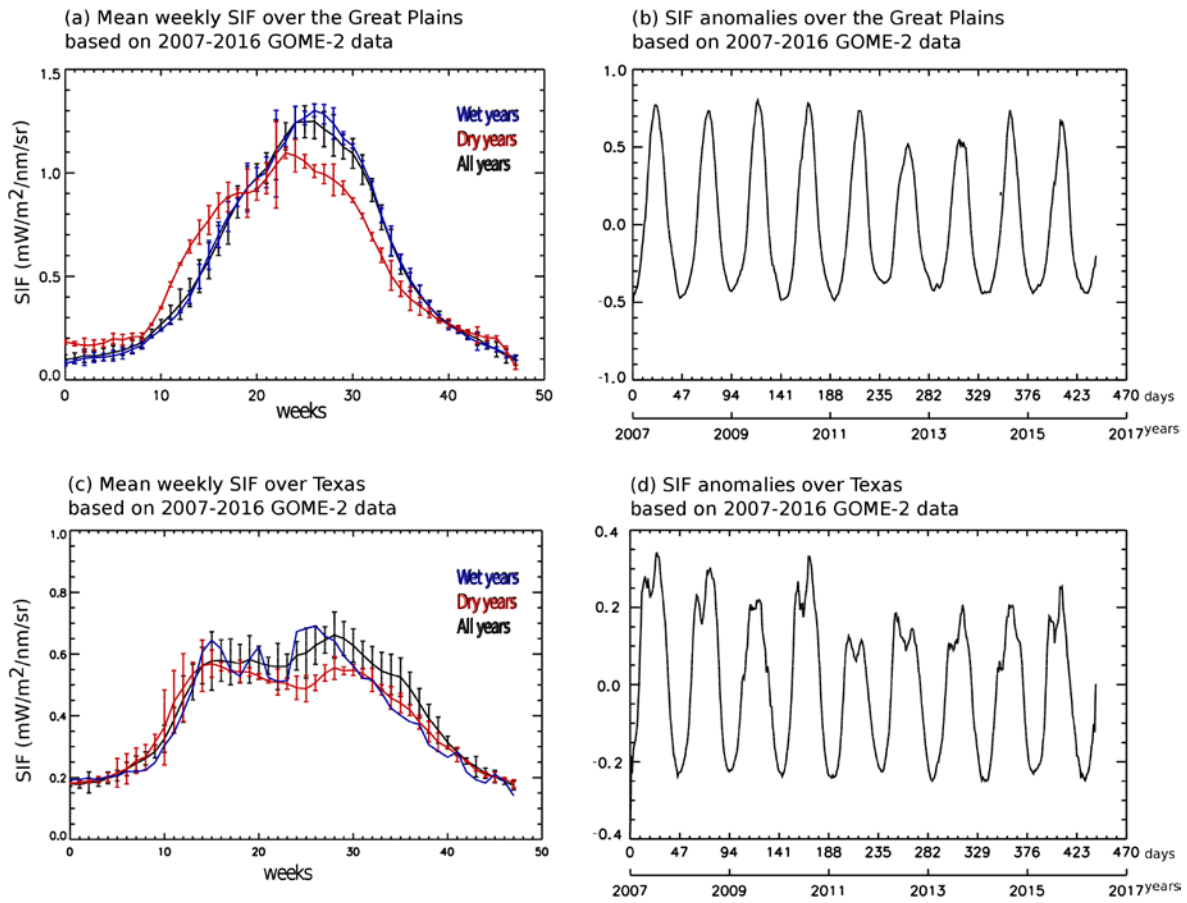


Figure 3.3 Mean weekly SIF (a,c) and SIF anomalies (b,d) over the Great Plains and Texas as inferred from GOME-2 data over the period of 2007–2016.

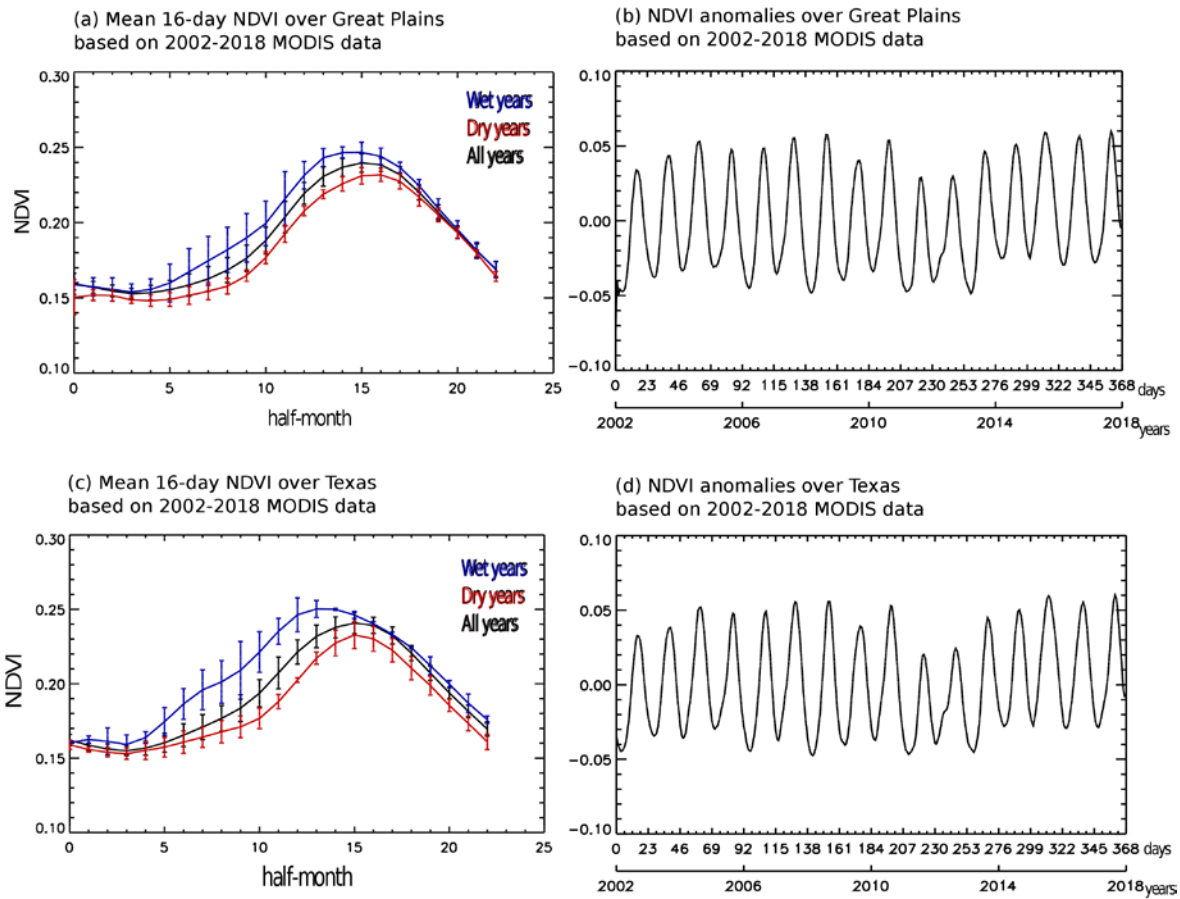


Figure 3.4 Mean 16-day composite NDVI (a,c) and NDVI anomalies (b,d) over the Great Plains and Texas as inferred from MODIS data over the period of 2002–2018.

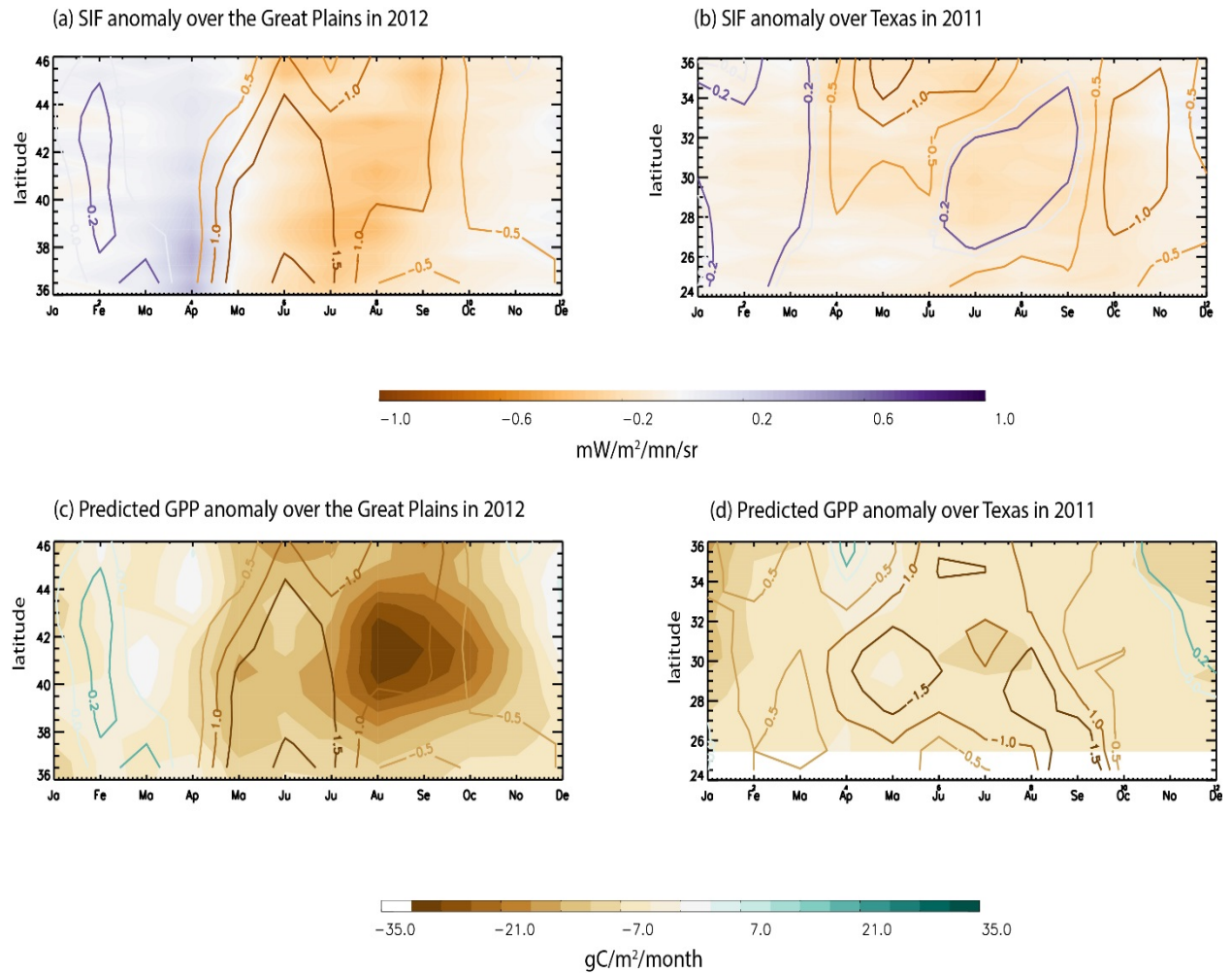


Figure 3.5 Hovmueller diagram showing propagation of drought-related SIF and GPP anomaly. GPP is calculated according to Equations 2.5, 2.6, 2.7, and 2.8 from Chapter 2. Rainfall is represented by contour lines with an interval of 0.5 mm/day.

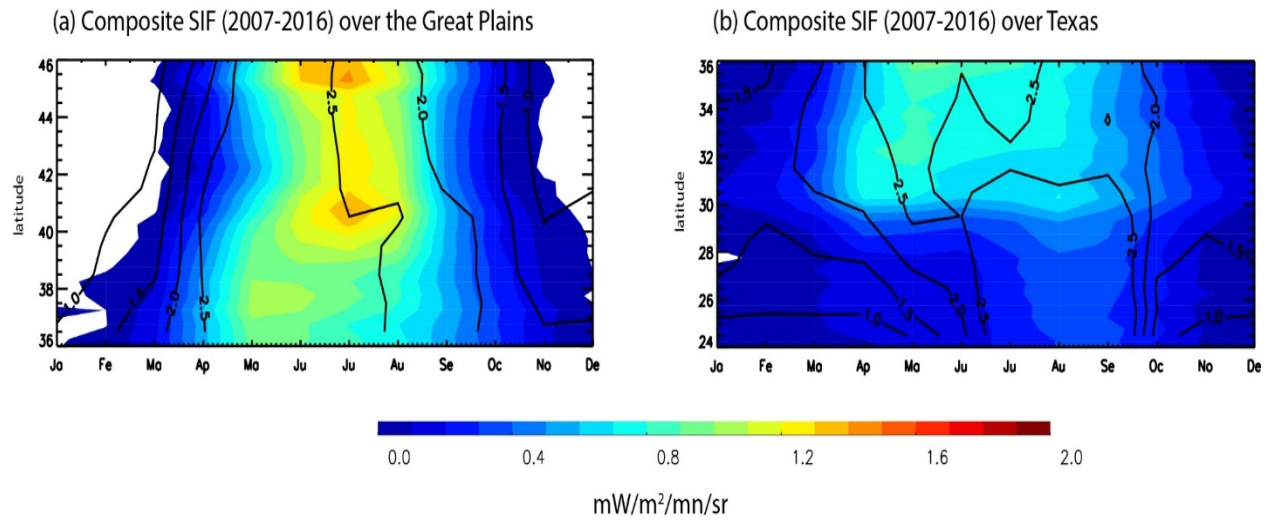


Figure 3.6 Hovmueller diagram of SIF composite (2007–2016) over the Great Plains region (a) and Texas (b). Rainfall is represented by the black contour lines with 0.5 mm/day interval.

CHAPTER 4: A Monte Carlo ray tracing model for simulating canopy-level emissions of solar-induced chlorophyll fluorescence

4.1 ABSTRACT

Efficiency of solar-induced chlorophyll fluorescence satellite observation is evaluated with the use of a model of light transport in a three-dimensional vegetation canopy. Designed and evaluated model employs a Monte Carlo ray tracing technique that offers simple yet rigorous approach of quantifying the photon transport in a plant canopy. This method involves simulation of a chain of scattering and absorption events incurred by a photon on its path from the light source. Implementation of weighting mechanism helps avoid ‘all-or-nothing’ type of interaction between a photon packet and a canopy element, i.e. at each interaction a photon packet is split into three parts, namely, reflected, transmitted and absorbed, instead of assuming complete absorption, reflection or transmission. Canopy scenes in the model are represented by a number of geometric primitives with specified sets of reflectance and transmittance. Our results demonstrate that emitted fluorescence decreases with increasing solar zenith angle (SZA) and leaf angle. However, under extremely high SZA when the sun is near the horizon, an increase in the leaf angle leads to increase in fluorescence. Our results show that satellite observes a fraction of total fluorescence emitted from a canopy; a hypothetical satellite with a scan angle of 32° is capable of “seeing” a maximum of ~50% of total emitted fluorescence. Increasing scan angle to 55° , similar to Moderate Resolution Imaging Spectroradiometer (MODIS) and Global Ozone Monitoring Experiment 2 (GOME-2) scan geometry, leads to the efficiency of up to ~80%. Satellite efficiency in registering fluorescence signal does not change with varying SZA, presumably due to the fact that direction of fluorescent photons emitted from a leaf does not exhibit dependency on the number of photons incident on a leaf. However, such efficiency varies with leaf angle as leaf angles might play a role

in determining directional cosines of the emitted fluorescent photons. The total amount of emitted fluorescence in all directions from a canopy ranges between 1–3 mW/m²/sr/nm, whereas that observed by a hypothetical satellite with a scan angle of 32° is 0–1.5 mW/m²/sr/nm.

4.2 INTRODUCTION

Solar-induced chlorophyll fluorescence is characterized by a broad band emission spectrum with two peaks: the left one in the red area of spectrum around 685 nm and the right one in the far-red region around 740 nm. For the past decades, SIF has been used in the laboratory and field scale studies, providing a non-invasive method for studying plant photosynthesis and plant physiological state in general.

SIF is physiologically related to photosynthesis and has been also shown to track gross primary production (GPP) better than fAPAR in deciduous broadleaf and mixed forests, and in croplands as well (Joiner et al. 2014). It has also been suggested that SIF can provide better estimates of GPP than reflectance-based vegetation indices (Frankenberg et al. 2011; Walther et al. 2016). Thus, SIF might be of importance in quantifying and modeling GPP which is a significant part of the terrestrial carbon cycle and is the largest global land carbon flux (Beer et al. 2010).

SIF was first associated with photosynthesis in 1931 through the illumination of dark-adapted leaves and its correlation with CO₂ assimilation (Kautsky and Hirsch 1931). The discovered effect was named after Kautsky and can be explained as follows: when a dark-adapted plant is exposed to the continuous light, chlorophyll fluorescence demonstrates characteristic changes in intensity, namely, a fast increase on a time scale of micro- to milliseconds, followed by a relatively slow decreasing phase until reaching a steady-state level. This phenomenon has

allowed for introduction of different types of fluorometers which have been actively used for ground-based kinetic fluorescence studies.

With the advent of satellite missions, the global scale observations of SIF have become available over the past two decades. Due to the strong absorption lines caused by telluric atmosphere absorption and the Fraunhofer lines in the solar spectrum, SIF can be retrieved from remotely sensed hyperspectral measurements (Meroni et al. 2009; Zhao et al. 2016). Another means of measuring fluorescence signal from satellite instrumentation is based on utilization of oxygen A and B bands which absorb at wavelengths where chlorophyll fluorescence is emitted (Joiner et al. 2013).

While satellite SIF retrievals proved to be useful for evaluating plant physiological conditions and estimating GPP, there exist certain limitations associated with satellite-based SIF data, presumably due to instrumental and algorithmic effects. For example, GOME-2 retrieval approach, employed to derive the primary dataset used in Chapter 2 and 3, relies on several simplifying assumptions such as negligible atmospheric scattering in the modeling of water vapor absorption in 710-745 nm region and modeling of fluorescence spectral signatures with the use of only a few parameters (Joiner et al. 2013). In addition, GOME-2 dataset is inherently noisy owing to low signal levels. This leads to the appearance of negative SIF values which are biologically unreasonable and should be accounted for in data processing. Also, in high latitudes in winter slightly positive or negative SIF values have been noted (while zero fluorescence is expected) which indicates an issue with SIF data at high solar zenith angles. GOSAT SIF data, that are produced with the use of a simpler approach that is also less prone to systematic error (Joiner et al. 2013; Joiner et al. 2011), are well characterized due to higher spatial resolution but cannot provide the spatial coverage of GOME-2 (Frankenberg et al. 2014). SIF retrievals from GOME-2

have been compared to those of GOSAT and showed an excellent spatial agreement. However, it is important to note that there exist drawbacks to such type of evaluations since GOME-2 SIF data have undergone only a limited amount of validation (Yang et al. 2015) and GOSAT retrievals were evaluated using indirect methods only such as simulations experiments and plausibility checks (Joiner et al. 2013). A possible solution to this problem might include validation using aircraft-, ground-based, and modeled SIF data.

Another issue that might be associated with the observational SIF data is the influence of satellite scan geometry and, namely, scan angles. Satellites observe the earth at certain scan angle, e.g. scan angle of GOME-2 sensor is up to $\pm 54^\circ$ (He et al. 2017). MODIS instrument, whose fPAR measurements together with ancillary data are used to provide GPP, has a scan angle of $\pm 55^\circ$. However, photons emitted from a leaf can propagate in any direction between -90 to 90° from the sides, top and bottom of a canopy. Thus, a satellite due to its configuration is only capable of capturing a part of SIF determined by the scan angle. This can severely impact the estimation of other parameters related to SIF, such as GPP.

Many studies have tried to estimate SIF using empirical and process-based models. Complementary to satellite SIF retrievals are vegetation fluorescence models developed for both leaf and canopy levels. The Scattering by Arbitrarily Inclined Leaves (SAIL) was a four-stream radiative transfer canopy model developed by Verhoef (1984) and further extended by Rosema et al. (1991) to include the fluorescence component modeled via doubling method. The FluorMOD project, launched in 2002 by ESA, focuses on addressing the need for an integrated canopy model that would capitalize on recent advances in leaf-level fluorescence modeling in conjunction with laboratory and field measurements. In the FluorMOD framework, canopy FluorSAIL model based on SAIL was developed to simulate chlorophyll fluorescence effects on the canopy reflectance

using inputs from FluorMODleaf. The Soil Canopy Observation of Photochemistry and Energy fluxes (SCOPE) model has integrated radiative transfer (RT), energy balance and photosynthesis calculations based on RT modules adapted from SAIL and FluorSAIL (van der Tol et al. 2009). All the above mentioned models represent canopies as structurally homogeneous entities for which a four stream model would be a reasonable approximation (Zhao et al. 2016). However, that poses a question as to how accurately these models estimate the effects of vegetation structure on SIF retrievals (Porcar-Castell et al. 2014) and specifically, how adequate the common “one-leaf” canopy approximation is in terms of modeling of vegetation-related parameters including SIF.

Thus, the purpose of this study is twofold: while developing a SIF RT model with an explicit three-dimensional canopy we would also use the model outputs to introduce corrections to the satellite data. Therefore, it would be possible to alleviate the drawbacks in satellite retrievals related to the instrumental configuration, in particular limited field of view. We have employed a Monte Carlo ray tracing approach to describe the processes of fluorescence absorption, transmission and reflection in a physically meaningful way. As such, Monte Carlo methods have been widely used to model light transport in different types of media and for various purposes, such as biomedical imaging (North 1996; Wang et al. 1995), radiation therapy and others. Recently, Monte Carlo techniques have been recognized as a valid and rigorous method of simulating the light interaction within vegetated surfaces (Govaerts and Verstraete 1998; North 1996; Zhao et al. 2015). It was shown that three-dimensional radiation transfer models are virtually the only ones capable of describing the heterogeneity of the media and its effect on the propagation of photons (Govaerts et al. 1996). As ray tracing techniques require a detailed description of canopy geometric properties, we have generated a vegetated scene represented by three-dimensional spherical canopies which would be further discussed in the following sections.

Sections 4.3 provides description of the model and its methodology. Section 4.4 presents and evaluates the model simulation results; section 4.5 summarizes the findings of the study and ends with the directions for the future research.

4.3 MODEL DESCRIPTION

This section discusses a method of SIF estimation with the Monte Carlo solution of a radiative transfer model.

Traditionally two methods of photon tracing are used: forward and backward. The forward method sends photon from the light source and traces its path until the photon is absorbed or scattered out of the scene. Respectively, the backward method generates photons from the sensor to the scene and traces them to the light source. In order to improve the efficiency of photon sampling we have used a combined ray tracing approach which employs both forward and backward ray tracing methods.

Prior to tracking the photons a canopy scene is generated. Forest structure is represented by a set of geometric primitives that are positioned in three dimensions over a horizontal plane (North 1996). The primitives define the shape and size of canopies within the scene. Within each canopy, foliage is defined by leaf size and angular distribution and optical properties of reflectance, transmittance and absorbance. These parameters are identical and homogeneous for all the canopies within the scene. For any leaf size the number of photons incident per square cm surface is $2.9 \cdot 10^{15}$ based on a solar irradiance of 1300 W/m^2 .

The model operates as follows (Fig. 4.1): the photon packet is initialized and direction of the emitted photon is determined by position of the light source described by x,y,z coordinates and directional cosines μ_x , μ_y , μ_z depending on solar zenith angle. We assume that the light source

emits photons in a spectral range spanning 400–750 nm. Therefore, we start the model simulation with the non-fluorescent photon flux from the sun which can be further scattered or absorbed by the canopy elements.

Having entered the canopy scene generated prior to the start of the radiative transfer part of the model, photons are tested for intersection with the leaves within the canopy. Upon the photon packet interaction with the first leaf on its path, the packet splits into three parts, namely, absorbed (N_{abs}), reflected (N_{ref}), and transmitted (N_{tran}). The number of photons of each new packet depends on the spectral properties of the canopy and the original energy of the photon packet:

$$N_{ref} = N_{init} \times \rho_l \quad (4.1)$$

$$N_{tran} = N_{init} \times \tau_l \quad (4.2)$$

$$N_{abs} = N_{init} \times (1 - \rho_l - \tau_l), \quad (4.3)$$

where N_{init} is the initial number of the photons sent from the light source, ρ_l and τ_l are leaf reflectance and transmittance respectively.

The direction of a newly generated packet is determined by the position of the leaf where the interaction happened and the new directional cosines that are a function of the scattering angle Θ and azimuth angle φ . The relationships are as follows:

$$\cos \theta = 1 - 2k \quad (4.4)$$

$$\varphi = 2\pi k \quad (4.5)$$

$$\mu_x = \frac{\sin \theta \times ((\mu_x \times \mu_z \times \cos \varphi) - (\mu_y \times \sin \varphi))}{\sqrt{(1 - \mu_z^2)}} + \mu_x \times \cos \theta \quad (4.6)$$

$$\mu_y = \frac{\sin \theta \times ((\mu_y \times \mu_z \times \cos \varphi) + (\mu_x \times \sin \varphi))}{\sqrt{(1 - \mu_z^2)}} + \mu_y \times \cos \theta \quad (4.7)$$

$$\mu_z = -1 \times (\sqrt{1 - \mu_z^2}) \times \sin \theta \times \cos \varphi + \mu_z \times \cos \theta, \quad (4.8)$$

where k is a random number between 0 and 1.

As the incident photon packet hits the leaf it excites fluorescence from both upper (adaxial) and lower (abaxial) sides of a leaf (represented by red lines in Fig. 4.1). We assume a bi-Lambertian emission in the model, i.e. leaf emits isotropic fluorescent radiance, and therefore, the number of photons and correspondingly fluorescence emitted from adaxial and abaxial side of a leaf is the same.

After the fluorescence has been excited in a leaf, the same processes happen to the newly generated fluorescent flux as in the case of the non-fluorescent flux: reflection, transmission and absorption, from both sides of the leaf. Thus, we can calculate the number of reflected, transmitted and absorbed fluorescent photons similarly to the non-fluorescent ones, except the leaf spectral properties ρ and τ should be replaced with those for fluorescent flux. In general, for every leaf except for the first one there are four types of processes taking place: absorption, transmission and reflection of both fluorescent and non-fluorescent photon packets and emission of fluorescence from both backward and forward sides of a leaf. These processes are repeated for each leaf until and unless number of photon hitting a leaf is less than one.

It is important to note that for convenience ‘photon’ and ‘photon packet’ are used interchangeably in the study. A photon packet refers to many photons traveling simultaneously along the same path (Zhao et al. 2016). As mentioned before, after having interacted with a canopy element, in our case a leaf, a photon packet can be divided into new packets characterized with new energies. However, for the purposes of ray tracing having a photon with direction would suffice. Therefore, we have used the concepts of ‘photon’ and ‘photon packet’ interchangeably.

After all the fluorescent photons escaping the canopy have been registered, we have calculated the total fluorescence in $\text{W/m}^2/\text{nm}/\text{sr}$. In order to obtain fluorescence values at 740 nm, we followed approach formulated by Lee et al. (2015) and applied a coefficient k to account for the

conversion of SIF integrated over all the fluorescence emission spectrum and SIF at 740 nm retrieved by GOME-2.

In addition, we explore the opportunity of quantifying satellite efficiency in terms of fluorescence registered by a satellite of interest. We use the common knowledge stating that photons emitted from all the leaves can travel in any random direction after an interaction with canopy elements which in this study are represented by circular leaves.

As photons are emitted, they are also associated with a certain angle at which they are emitted. Photons that are directed within the scan angle of a satellite can be viewed, others will escape the satellite even if the satellite is a nadir pointing one. We estimate satellite efficiency in capturing fluorescence as the fraction of the photons registered within the scan angle of a satellite out of the total number of photons emitted by a tree canopy in all possible directions from -90 to 90° (Fig. 4.2). The equations for satellite efficiency is as follows:

$$\eta_{sat} = 100 \times \frac{\sum_{scan\ angle\ lower\ limit}^{scan\ angle\ upper\ limit} N_i}{\sum_{-90}^{90} N_i}, \quad (4.9)$$

where η_{sat} is the efficiency of a given satellite in capturing fluorescence emission, N is a number of photon and i is the scan angle.

4.4 RESULTS

We started the model run with initializing a number of photons sent from a light source whose position is determined by SZA and SAA. Firstly, it is important to recognize the influence of the solar zenith angle of the light source on the distribution of SIF photons emitted by the canopy leaves. For this purpose we have run simulations with the constant leaf angle and other parameters on one side and varying SZA on the other. Figure 4.3 demonstrates that as solar zenith angle increases, which translates to the sun being lower over the horizon, fluorescence emitted by the

canopy decreases. Maximum fluorescence is emitted when the sun is at the top ($SZA = 0^\circ$) and gradually decreases as SZA increases.

As the SZA reaches 75° , almost no fluorescence can be registered escaping the canopy which looks valid, especially in the light of the fact that GOME-2 SIF data with SZA greater than 70° are eliminated in the process of quality control (Joiner et al. 2013). These results are expected because at higher SZA , density of incident photons per square unit area of leaf surface decreases.

Leaf angle distribution (LAD) is an essential factor influencing reflection and absorption of solar radiation within the canopy which in its turn has significant impact on the growth and development processes and, thus, plant productivity. In addition, plant canopies can exhibit a range of LADs – from planophile with leaves maintaining relatively horizontal position to erectophile with mostly vertical leaves. At different stages of plant development LAD might undergo changes, e.g., in the process of wilting LAD tends to acquire more erectophile traits. Therefore, introduction of LAD into fluorescence calculations is absolutely necessary. We have modeled SIF for several cases of different leaf angles while keeping all the other model parameters, including SZA , constant. As it can be seen from Figures 4.4a–4c, with the increase of leaf angle from 0 to 45° which corresponds to the leaf position change from horizontal to inclined, the average values of fluorescence decreases from about $2 \text{ mW/m}^2/\text{nm}$ to less than 1. With higher SZA of 30° , such decrease in fluorescence emission is even more prominent, e.g., at $SZA = 30^\circ$ and leaf angle = 45° there is practically no registered fluorescence. This is presumably because of the fact that leaves oriented in a direction perpendicular to the sunlight receive more photons. Increasing leaf angle

makes the leaves to receive photons at an inclined angle (Fig. 4.6). Figure 4.6 shows the photon intensity of a solar beam with SZA equals to α on a leaf surface with inclination of β .

However, high SZA combined with high leaf angle does not necessarily lead to extremely low SIF emission. As shown in Figure 4.5, SIF values are higher in the case of leaf angle equal to 45° rather than 0° when SZA equal to 75° . This is related to the fact that number of fluorescent photons emitted by the canopy depends on the cosine of the sum of solar zenith and leaf angle (Fig. 4.6). Since in the second case (Fig. 4.5b), the value of cosine of 120° is higher than that of 75° , the emitted fluorescence tends to be less significant than in the first case. Thus, under high SZA conditions the leaf angle distribution plays an especially important role in determining fluorescence emission from the top of the canopy.

We have also investigated the influence of canopy size on the emitted fluorescence. While regardless of the size and structural peculiarities of various canopies the underlying physical processes related to radiative transfer remain the same, canopy size might affect the amount of emitted fluorescence. We have compared the outputs of two model runs with three-dimensional canopies of two different sizes: with 30 and 100 leaves in x, y and z-direction, respectively, assuming same number of photons incident on the leaves of both trees. Figure 4.7 shows the top-canopy view of the canopies and indicates that regardless of the canopy size spatial distribution of fluorescence emitted from the top of the canopy remains relatively unchanged as well as the absolute SIF values. These results show that the general response to SZA and leaf angle is the same for both types of trees - fluorescence emitted from the top of the canopy decreases as SZA and leaf angle increase. Highest fluorescence is emitted from both trees at $\text{SZA} = 0^\circ$ and leaf angle $= 0^\circ$. At higher SZA ($\text{SZA} = 60^\circ$) with leaf angle of 15° , fluorescence is very low. Fluorescence values (see color bar) are consistent as well for both trees.

After exploring the effects of SZA and leaf angle on canopy level fluorescence, we have looked into the role of satellite configuration in quantifying SIF emission. It is well known that satellite tool parameters can be considered a limiting factor on how much information about a particular phenomenon under study can be retrieved. In this paper we focus on evaluating the effects of satellite scan angle on the modeled fluorescence emission.

Photons emitted from the top of the canopy propagate to different directions. These photons are traveling in the upward direction (to the sky) and directions of these photons can be random between 0 to 180° (or first two quadrants). To estimate the fraction of photons that are captured by the satellites compared to all the total number of photons emitted from the canopy, we have selected two values for the scan angle: 32 and 55°. These particular values were chosen based on the configuration of GOME-2 and MODIS missions since both of these two missions are indispensable sources of information on vegetation state parameters. According to He et al. 2017, in the nadir viewing mode the maximum across-track scan angle is $\pm 54^\circ$ for GOME-2 spectrometer; for MODIS mission whose info is used to provide global-scale GPP estimates, the scan angle is $\pm 55^\circ$. A hypothetical satellite with a lower scan angle of 32° was introduced in order to investigate the details of how satellite scan angle affects efficiency of registering photons escaping from a canopy. We have performed a model run for this hypothetical satellite with a smaller scan angle of 32° and a model run configured to account for MODIS scan angle. Figures 4.8 and 4.9 display percentage of modeled top-of-canopy fluorescence that is registered by a satellite depending on its scan angle.

The results are indicative of the importance of scan angle: as it increases from 32 to 55°, the model outputs demonstrate similar increase is noted in the percentage of fluorescence that is “seen” by the satellite instrumentation. The spatial pattern of SIF from the top of the canopy

remains relatively unchanged, with SIF being emitted rather uniformly from the canopy with the highest emission zones closer to the center of the canopy top. With increasing SZA, fraction of photons observed by satellites does not show a notable change. As seen in Figures 4.9a and 4.9b, fractions of photons seen by the satellite with scan angle of 32° are relatively same or can be insignificantly different. Similar patterns are observed in case of the satellite with scan angle of 55° (Fig. 4.8); however, as it was noted, in general, higher scan angle enables a greater fraction of photons to be registered as seen in Figures 4.8 and 4.9. A satellite with a higher scan angle of about 55° effectively sweeps out a 110° Earth field of view in each scan while a satellite with a scan angle of 32° is able to scan a 64° FOV.

We have also plotted the modeled SIF values across the top of the canopy (Fig. 4.10). Figure 4.10 shows the mean fluorescence emitted from a canopy in all directions (black line), fluorescence observed by satellite (blue line) and the ratio of fluorescence registered by satellite to the actual or total fluorescence emitted (red line). Leaf numbers 0 and 100 represent position of the leaves at the edge of canopy and 50 represents the center leaf at the top along the X direction.

As demonstrated in Figures 4.8 and 4.9, the absolute values of fluorescence emission registered by the satellite and satellite efficiency increase as the satellite scan angle becomes higher. Such increase is not characteristic for the total TOC fluorescence as its formulation is independent from satellite configuration variables. With the increase in SZA, the number of photons emitted and that of photons registered by satellite decreases; however, efficiency of the satellites does not display notable variations. This finding indicates that directions of photons emitted from a leaf do not change or depend on the number of photons entering the tree.

As we investigated the effect of solar zenith, leaf, tree size, and satellite scan angle on fluorescence emission modeling, we have discovered a curious feature of the relationship between

SIF captured by a satellite and the above mentioned parameters (Fig. 4.11). It can be inferred that with the increase in SZA, fluorescence tend to exhibit lower values in both cases – that of total TOC modeled fluorescence and fluorescence registered by the satellite. However, it is apparently the leaf angle that plays a more significant role in determining the satellite efficiency in capturing fluorescence and the absolute values of fluorescence captured by the satellite instrumentation. As it can be seen from Figures 4.9a and 4.9c, under the same SZA = 0° and satellite scan angle = 32° increase in leaf angle leads to a more pronounced reduction in fluorescence measured by satellite and satellite efficiency. It can be thus inferred that changes in leaf angle are more essential to the quantification of SIF retrieval by satellites than solar zenith angle. This is presumably because of the fact that inclined leaves tend to redirect the photons in a way that the photons have a higher probability to enter the inside of the trees and then be absorbed and reemitted as fluorescence. This finding might have important implications as leaf angle distribution is known to vary for various tree species and that potentially may exert influence on how SIF retrievals should be approached.

4.5 CONCLUSIONS AND DISCUSSION

This study represents an effort to quantify the top-of-canopy fluorescence as viewed by the satellite instrumentation using the Monte Carlo ray tracing approach. It was discovered that canopy size is not a significant parameter for SIF emission quantification, while SZA and leaf angle distribution proved to exert more influence on the total TOC fluorescence modeling results. Our results show that fluorescence emitted from a canopy decreases with increasing SZA and leaf angle; however, higher leaf angle might be more beneficial than horizontal leaves when SZA is very high (>70°). At the same time, the combined SZA and leaf angle are of great importance as the number of photons from the light source (in our case, the sun) that can be further absorbed and

reemitted as fluorescence from the canopy, depends on the cosine of the sum of solar zenith and leaf angle.

Exploring the influence of satellite configuration parameters, namely the scan angle, has provided us with some valuable insights: as expected, the total modeled SIF registered by a satellite increases with the rise in the scan angle; however, it was found that under the same scan angle conditions, a change in leaf angle is more likely to substantially influence the satellite viewed total fluorescence and satellite efficiency as well. Our results conclude that satellite efficiency of registering fluorescence tends to depend on leaf angle rather than SZA.

This study can be extended by the use of the input sunlight and skylight density provided as TOC measurements or the atmospheric radiative transfer simulation software such as MODTRAN. Future work on the model improvement includes (but is not limited to) adjustments in the representation of the canopy itself such as addition of clumping/clustering of leaves. Currently, the model simulates photon transport in the canopy only, therefore, future work will be also aimed at modeling photon interactions within the other parts of a tree and its surroundings, e.g. interaction with trunk, soil surface and between adjacent canopies. In addition, in reality while leaves remain the main source of emitted fluorescence, other canopy elements such as stems and stalks might contribute to fluorescence emission as well. For the purposes of this study we haven't included into consideration any canopy elements except for leaves; however, further research might be required to quantify potential contribution of various canopy sources to the emitted fluorescence.

This study calculates a fraction of total TOC fluorescence that is actually registered by a satellite and shows that under a scan angle approaching 60° a higher fraction of emitted fluorescence can be captured as compared to that retrieved by the current day satellites with lower

scan angle values. Thus, incorporation of the findings of this paper in future satellite designs or application of a correction factor can help improving the calculation of SIF and parameters related to it.

This photon transport model can potentially be coupled to a leaf level solar-induced chlorophyll fluorescence model with the aim of further advancing of accuracy of the modeled SIF, which, in its turn, has a potential of improving our predictive capability of terrestrial carbon uptake.

Acknowledgements

This study was supported by funds from the Oak Ridge National Laboratory in Oak Ridge, TN. We thank Dr. Lianhong Gu for his valuable and constructive suggestions during the planning and development of this research work. We also thank Dr. Zhao from Beihang University for the clarifications and suggestions on Monte Carlo methods application in this study.

Start of the model at TOC

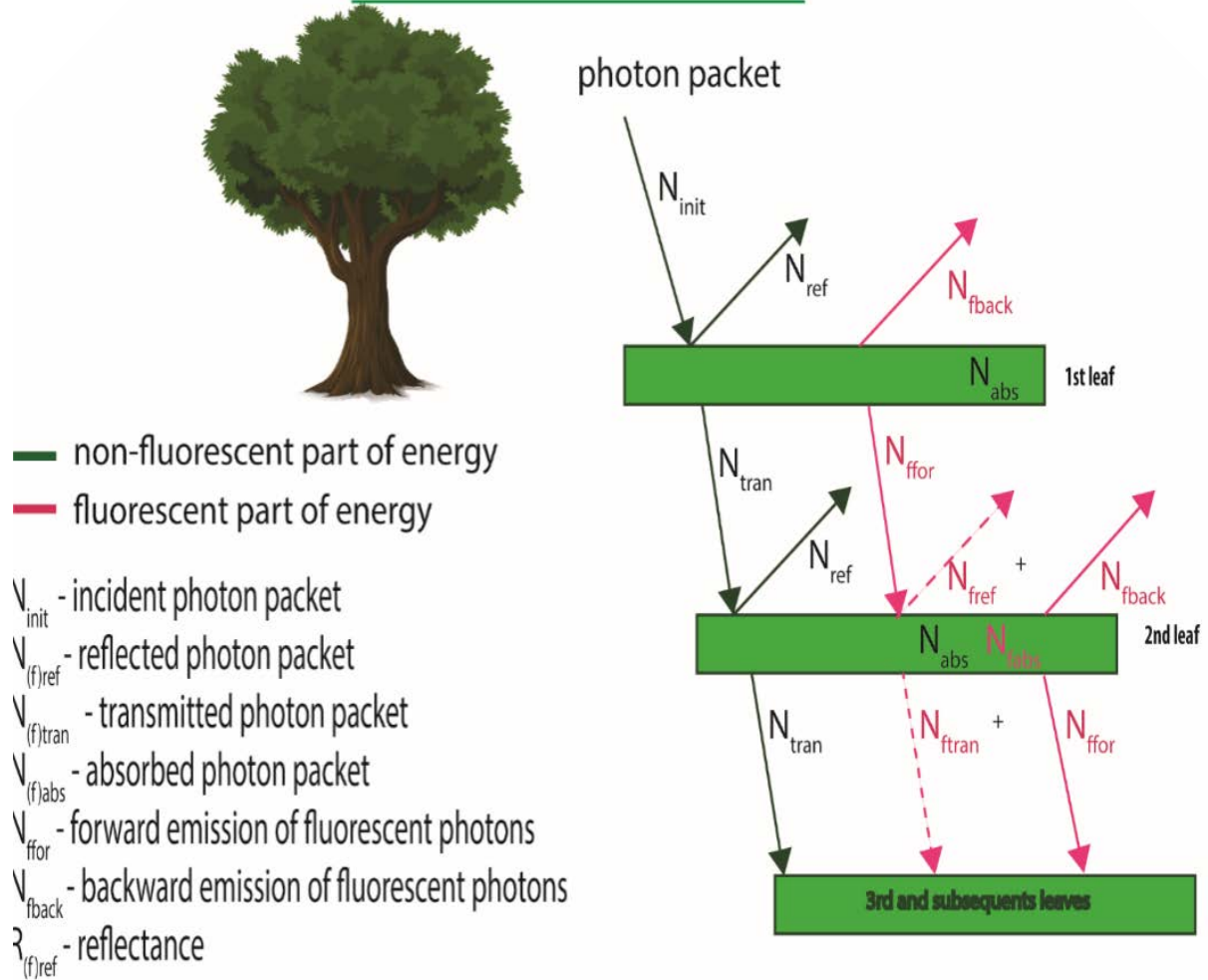


Figure 4.1 Schematic diagram showing the layout of the Monte Carlo ray tracing model presented in this study.

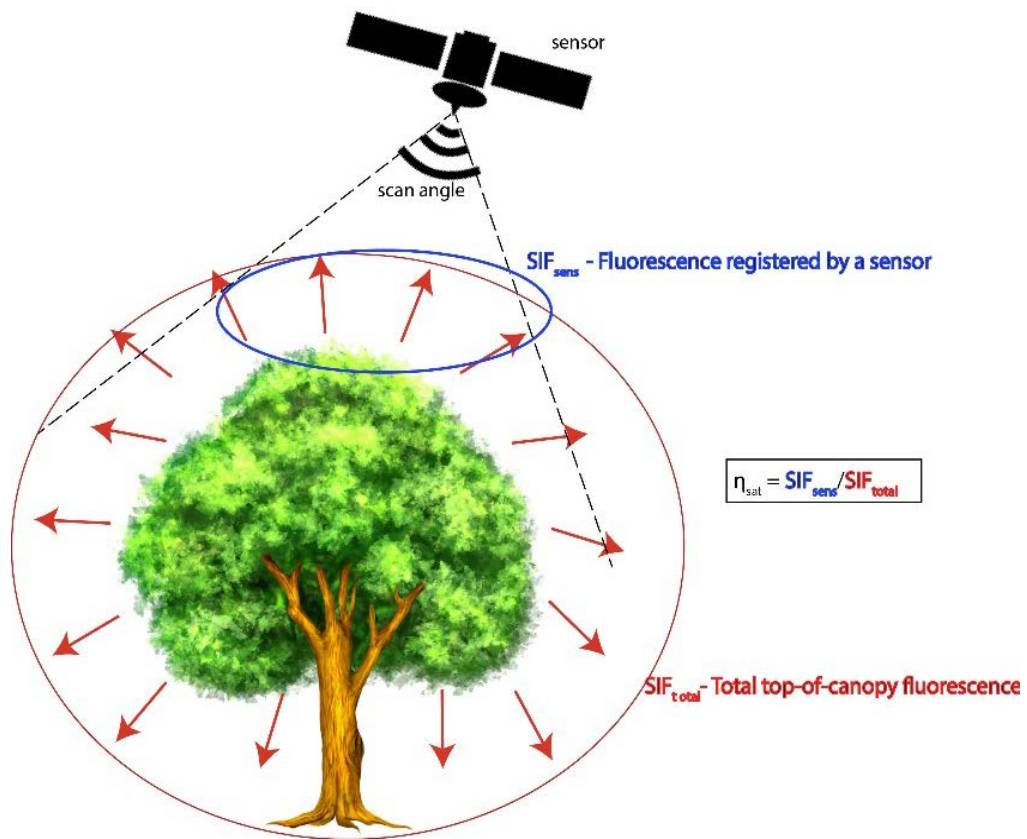


Figure 4.2 Schematic diagram of calculations for satellite efficiency for fluorescence.

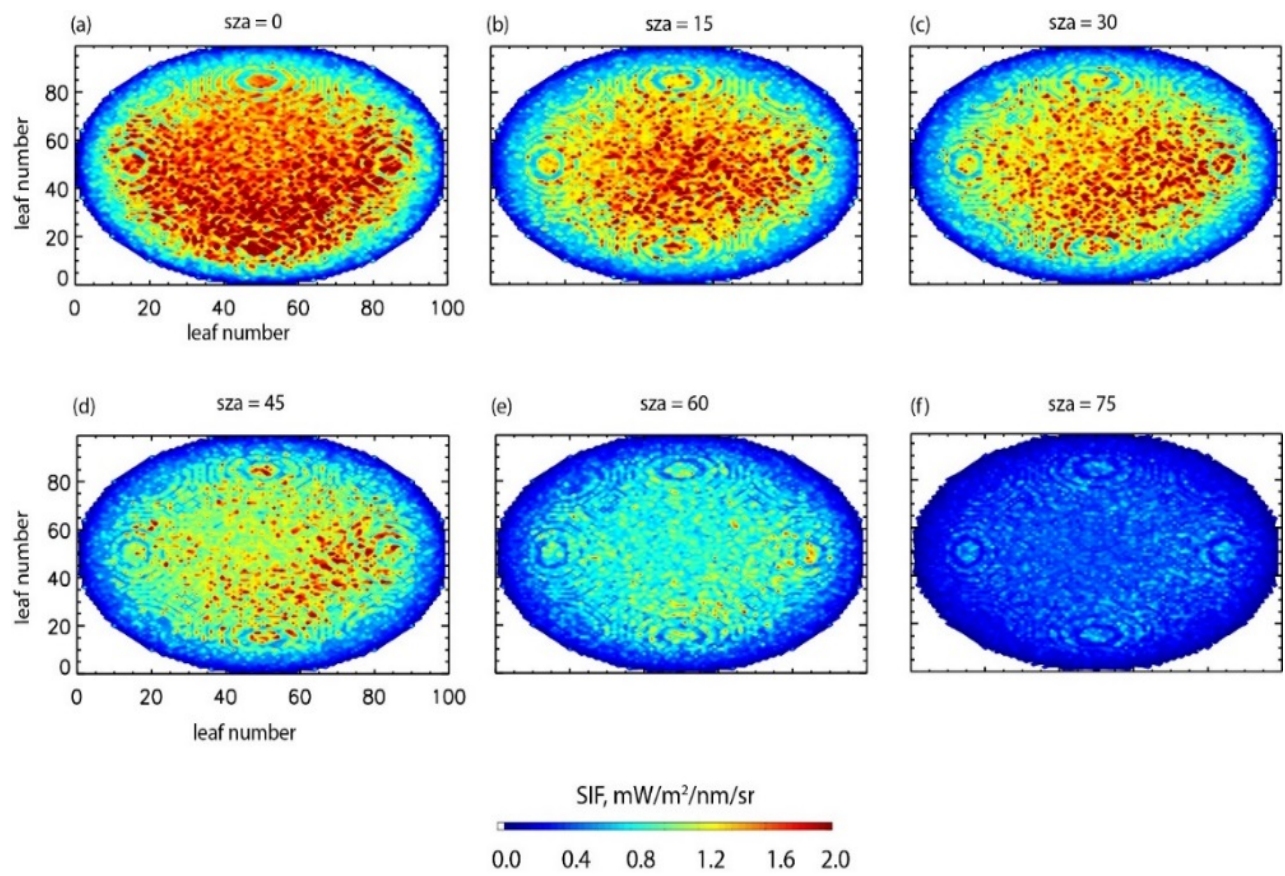


Figure 4.3 Top view of canopy emitting fluorescent photons under different solar zenith angle conditions.

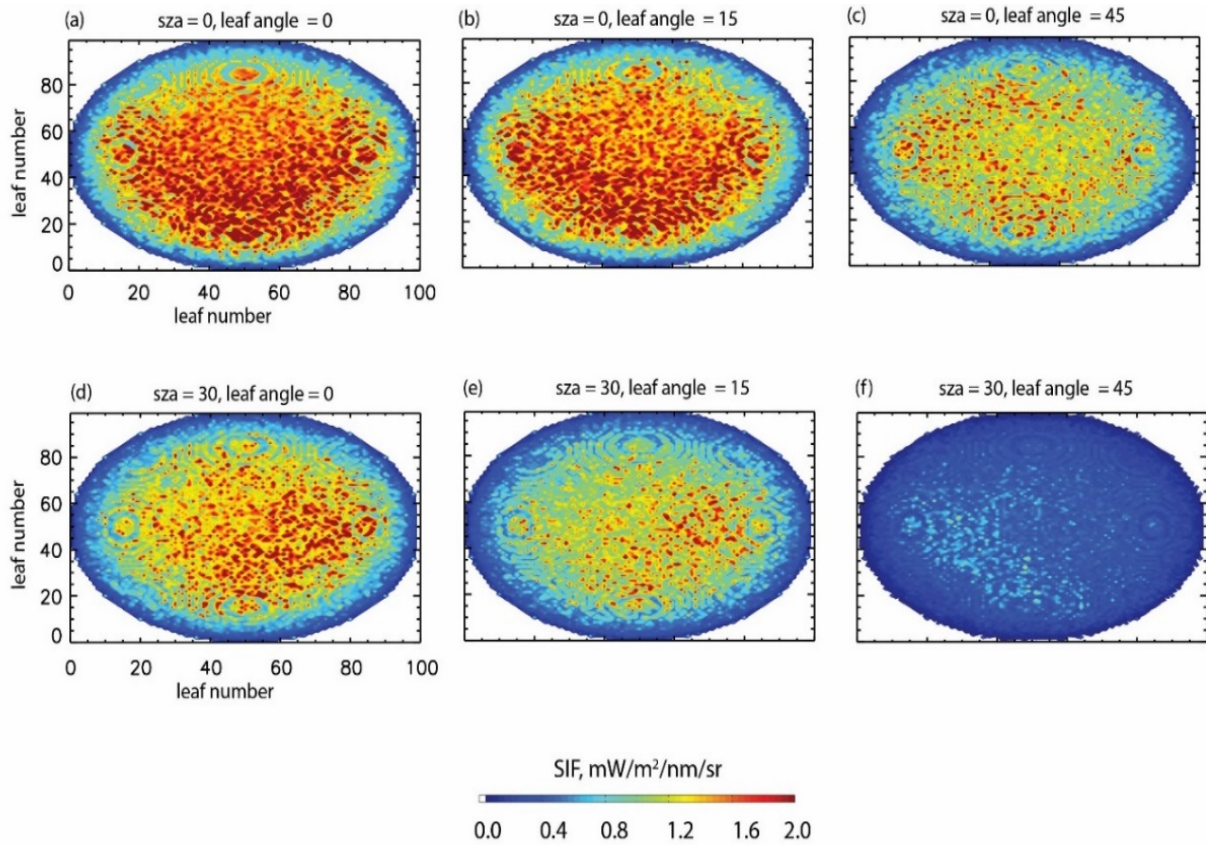


Figure 4.4 Modeled top canopy fluorescence dependence on leaf angle distribution.

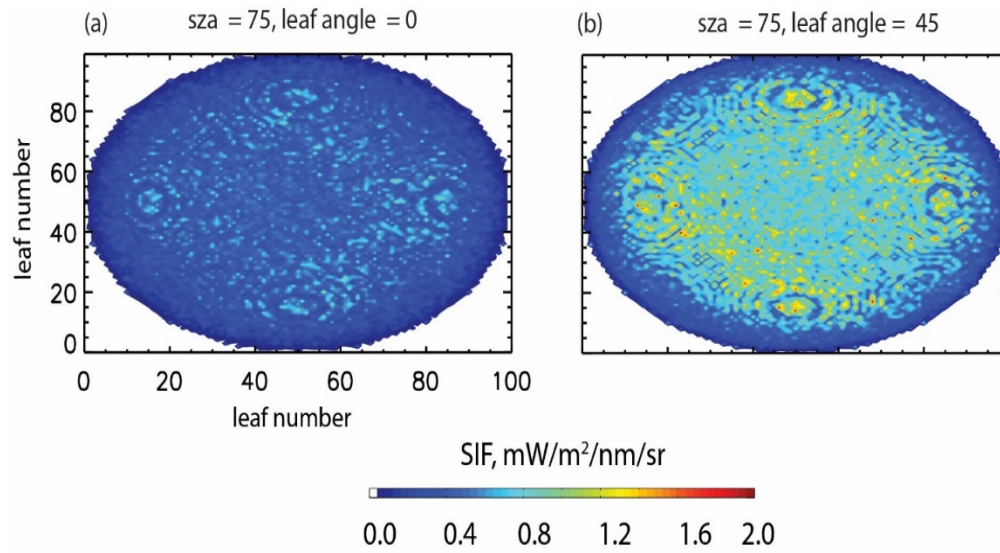


Figure 4.5 Fluorescence emitted from the top of the canopy a) leaf angle = 0°, SZA = 75°;
 b) leaf angle = 45°, SZA = 75°.

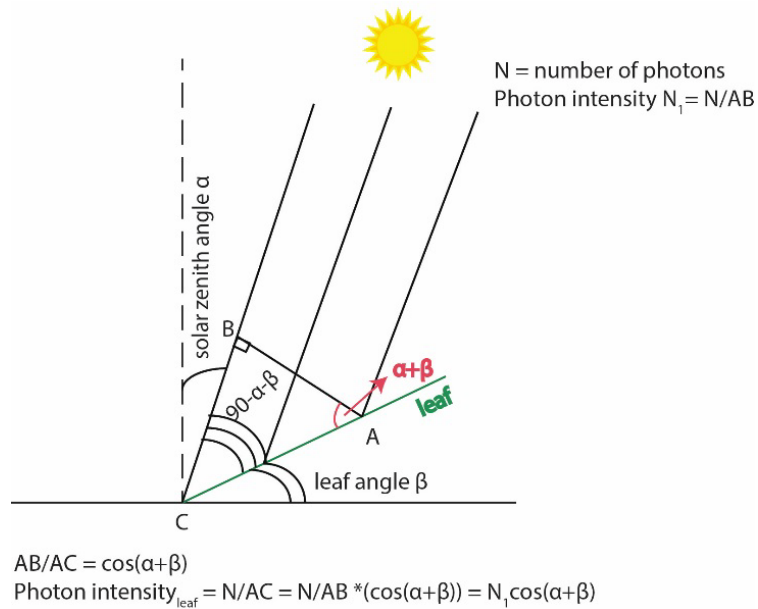


Figure 4.6 Schematic of photon intensity dependence of SZA and leaf angle cosines.

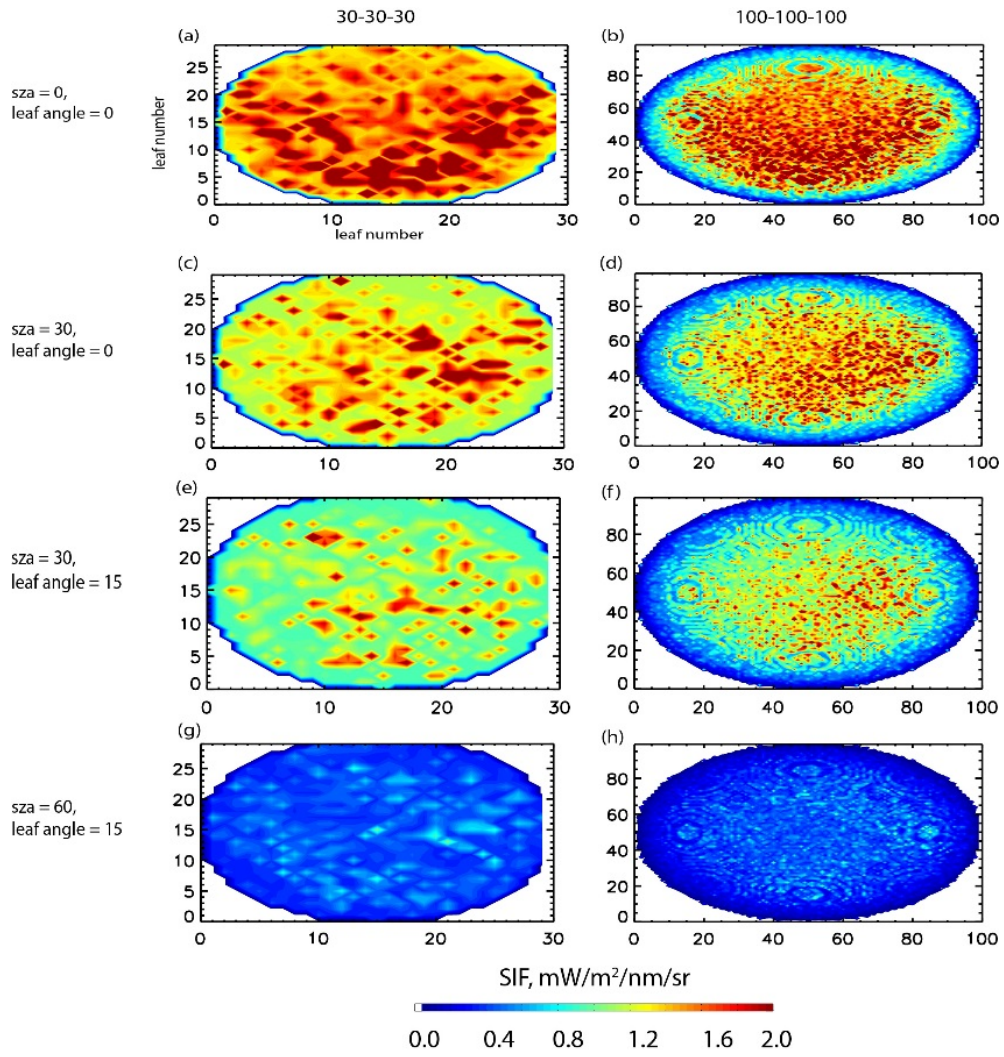


Figure 4.7 Fluorescence emitted from the top of the spherical canopy of different size.

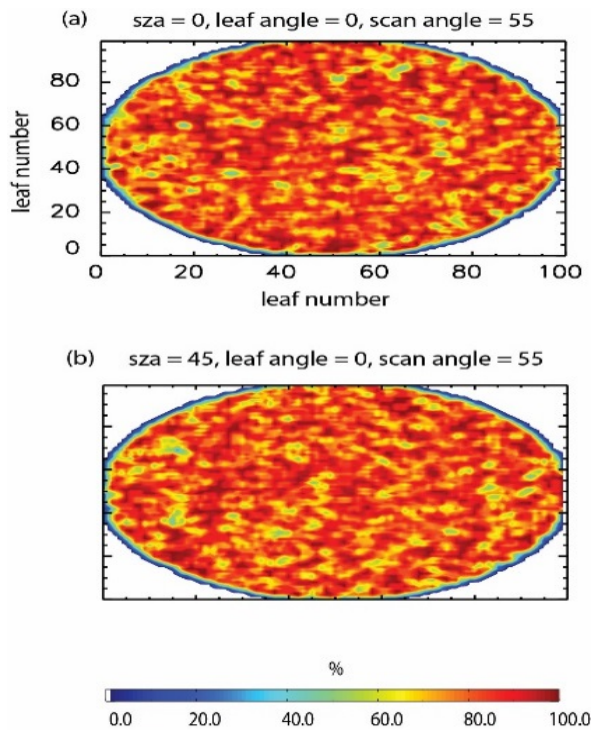


Figure 4.8 Percentage of modeled top-of-canopy SIF as registered by satellites, assuming scan angle of 55° .

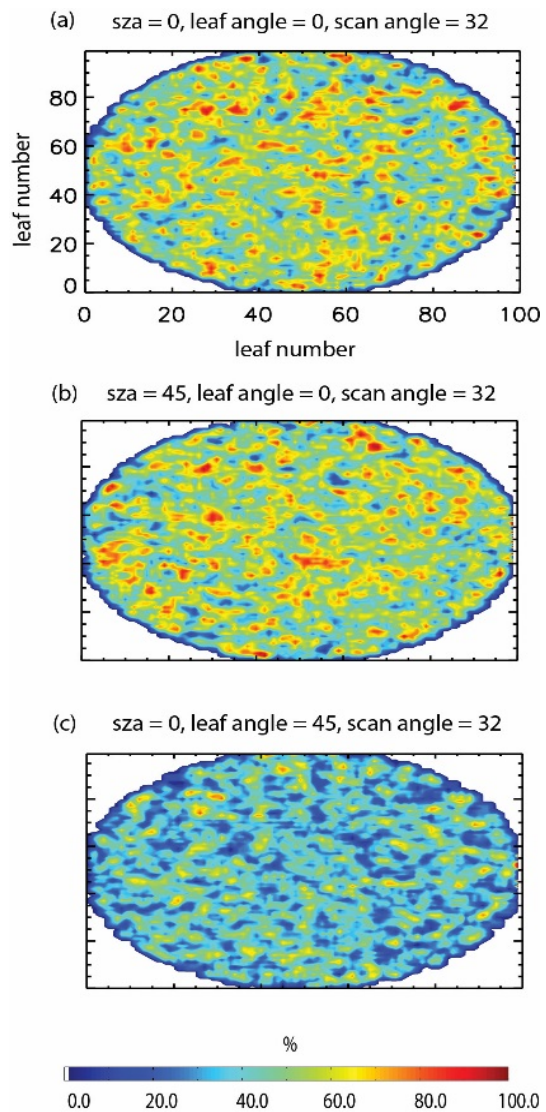


Figure 4.9 Percentage of modeled top-of-canopy SIF as registered by satellites, assuming scan angle of 32° .

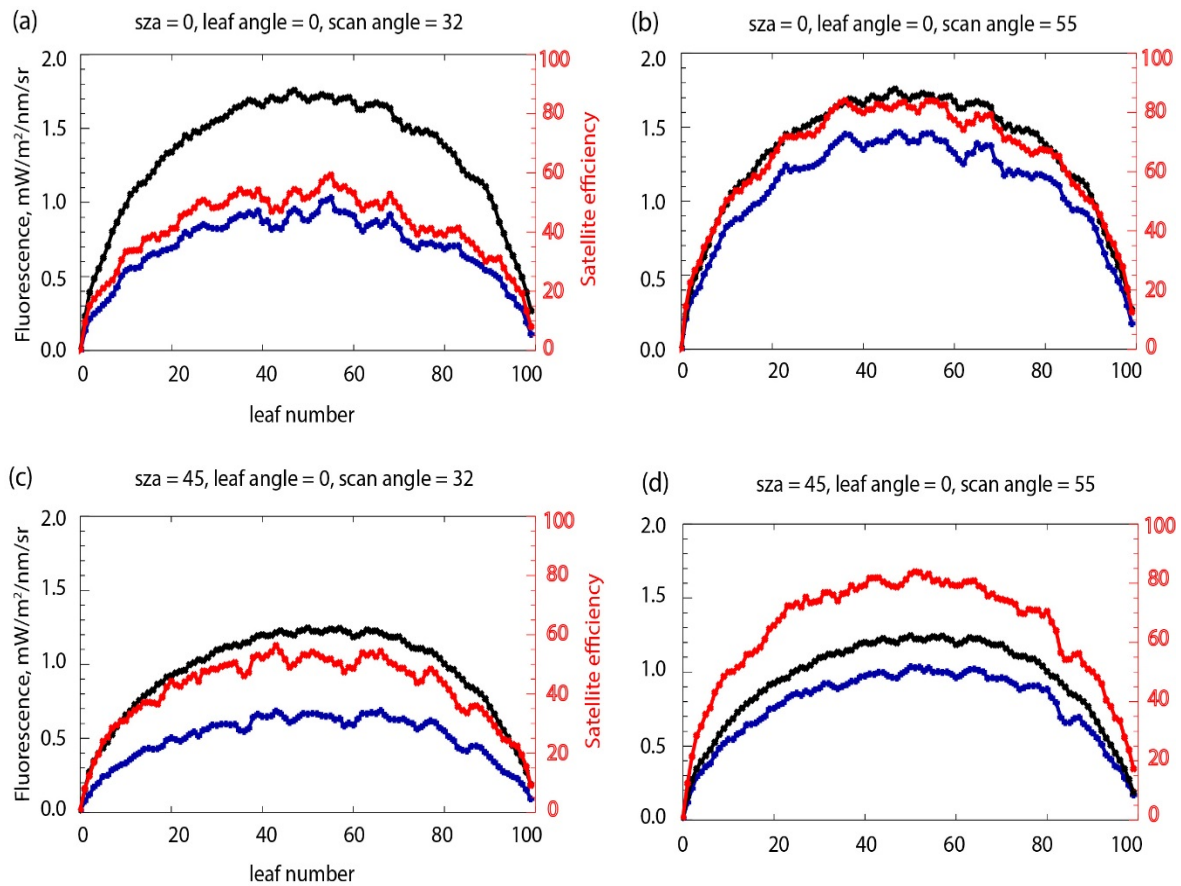


Figure 4.1 Top-of-canopy fluorescence at z-direction cross section with leaf and solar zenith angle changing from 0 to 45°: black color indicates total modeled fluorescence (in mW/m²/nm/sr); blue color – fluorescence registered by a satellite (mW/m²/nm/sr), red color – satellite efficiency equal to the percentage of total TOC fluorescence registered by satellite.

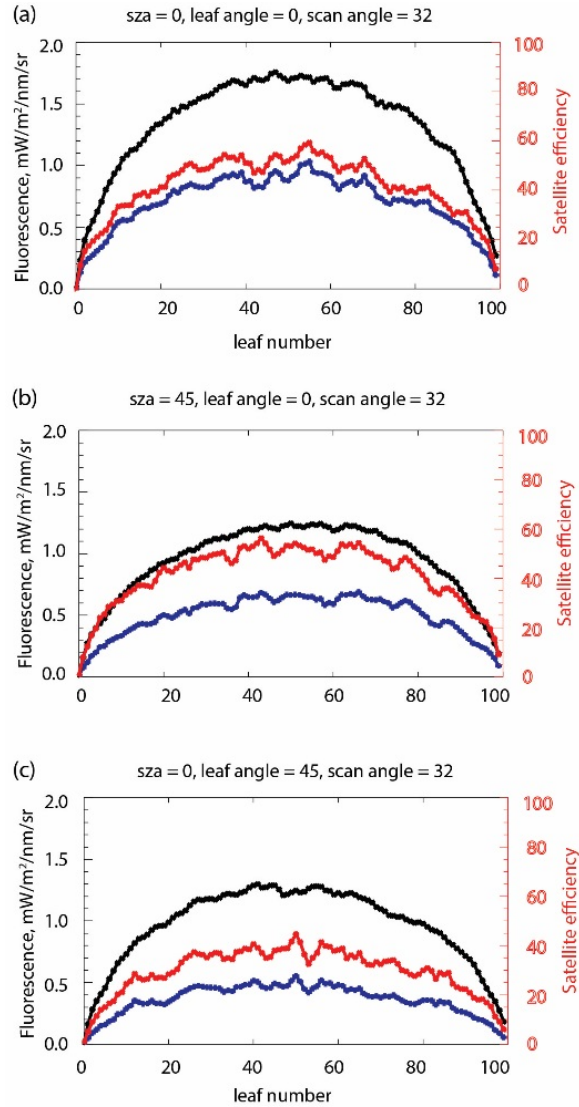


Figure 4.11 Top-of-canopy fluorescence at z-direction cross section with leaf and solar zenith angle changing from 0 to 45°: black color indicates total modeled fluorescence (in mW/m²/nm/sr); blue color - fluorescence registered by a satellite (mW/m²/nm/sr), red color – satellite efficiency calculated as percentage of total TOC fluorescence registered by satellite.

CHAPTER 5: Conclusions and future research

5.1 SUMMARY

The scientific findings presented in this research are mainly based on the multi-year satellite data analysis and aim at establishing and clarifying the relationships between SIF, GPP and other parameters, as well as exploring the potential of SIF in detailed drought characterization, with the focus on the drought onset and demise, from which duration of a drought event can be inferred. In addition, this dissertation presents a modeling effort in SIF simulation with the use of a combination of Monte Carlo backward and forward ray tracing.

This dissertation consists of four parts. Chapter 1 introduces the subject matter and establishes the importance of SIF in the context of plant functioning and connection to plant production.

Chapter 2 focuses on the estimation of gross plant production with the use of SIF, precipitation and soil moisture data over the continental US. In this chapter we have introduced a new method of GPP quantification that is based on the usage of multiple linear regression technique. While previously it has been claimed that information provided by SIF is sufficient to estimate plant productivity even without ancillary data, we have shown that introduction of additional parameters that might have independent impact on GPP (not through SIF) has a potential to improve GPP estimates and bring them close to the ground-based values taken as ground truth.

When deriving the equations for crop and grass GPP estimation we have taken into account the differences in grass and crop plant functional types (as their response to precipitating and soil moisture variations might differ) and precipitation and soil moisture conditions over the continental US. Our analysis based on several MLR cases revealed a curious tendency: when

GPP estimates are produced on the basis of SIF only, they tend to be underestimated; however, when SIF, precipitation and soil moisture retrieved simultaneously are used to derive the MLR equation, GPP values are significantly higher as compared to the ground-based observations. Our analysis indicates that using a discovered lead–lag relationship between SIF on one side and precipitation and soil moisture helps provide GPP estimates that are more consistent with the ground-based flux tower observations. We have estimated the lead–lag between SIF and precipitation at 2 to 4 weeks for crop and grass vegetation respectively. We presume that such difference in the timing of SIF response to a precipitation event might stem from how plant water need varies according to the stage of plant development: plants are typically most sensitive to water deficit in the development period. Therefore, their productivity around the end of the lifecycle, i.e. at the ripening and harvesting stages, would demonstrate a dependence on the precipitation they received in earlier life stages. Apparently, the life cycle of crops and grasses are different enough to cause a difference in lead–lag relationship between SIF and precipitation for these two vegetation types. Based on the findings of Chapter 2, for future applications it is necessary to consider plant water uptake fluctuations within the plant lifecycle stage in order to obtain valid plant production estimates. To our knowledge, this is the first study to demonstrate both importance of inclusion of other parameters influencing plant productivity (along with SIF) and that of accounting for the plant physiological variations linked to plant water need at different stages of its lifecycle. It is to be noted that GPP estimates produced by the MLR equations agree well with the drought trends over Texas in 2011 and the Great Plains in 2012.

Chapter 3 aims at investigating the usefulness of SIF and another vegetation-related indicator – NDVI – in delineating drought timing characteristics such as onset, demise and duration. Our analysis indicates that while SIF tends to demonstrate an earlier response to

drought conditions (as inferred by significant departure of rainfall from climatological values based on the precipitation record spanning from 1979–2016) as compared to that of NDVI, neither SIF nor NDVI can serve as a reliable early drought indicator as there is a significant lag between changes in rainfall and respective changes in these two variables. The findings from Chapter 3 show that a typical lag between precipitation decrease and corresponding SIF level change is on scale of about one month which is consistent with the findings regarding lead–lag from Chapter 2. In addition, our results demonstrate that even though drought conditions are present in both 2012 (over the Great Plains region) and 2011 (Texas region) negative SIF anomalies are more prominent over the Great Plains region. It was also found that GPP values produced according to the MLR approach with lead–lag consideration tend to be more sensitive to drought conditions than SIF itself. This is likely due to how MLR-based GPP was formulated – by definition it takes into account precipitation, soil moisture and SIF relationship with GPP while also taking care of the interdependence between all these variables.

Chapter 4 introduces a Monte Carlo ray tracing model to provide estimates of top-of-canopy fluorescence and its variations with changes in solar zenith angle and leaf angle. It also aims at quantifying the effect of satellite configuration, namely scan angle, on the efficiency of fluorescence registering by a given satellite. Our modeled SIF values are of plausible magnitude; they also demonstrate an expected inverse relationship with solar zenith angle while the link between modeled fluorescence emission and leaf angle distribution is not trivial. As we have looked at the impact of satellite scan angle on registration of fluorescence at the top of the canopy, our findings showed that importance of leaf angle distribution compared to that of solar zenith angle is higher in terms of how much of emitted fluorescence is captured by a satellite with a

certain scan angle. Potentially, research finding presented in Chapter 4 can help us in validating satellite SIF retrievals or introducing corrections to them.

5.2 FUTURE WORK

Some of the remaining scientific questions are discussed at the end of each chapter. In general, to address the uncertainties and limitations of this research, future work is to be done.

Firstly, as recommended in Chapter 2, in order to create more realistic estimates of GPP according to the presented method, it is necessary to include other vegetation types into consideration as currently only crop and grass vegetation are analyzed. As it is known that SIF-GPP relationship is a biome-dependent one, MLR formulations for crops and grasses might not be suitable for other vegetation types – therefore, equations need to be formulated separately for the remaining types. If to go to a greater level of detail, inclusion of specific crops might be beneficial as well.

As evident from Chapter 3, there is a need for SIF and NDVI retrievals of higher temporal resolution. Better tracking of SIF variations might be enabled if sub-daily retrievals are available. In addition to employing statistically-based method for investigating drought parameters such as drought initiation and cessation, it is necessary to look into the underlying mechanisms of vegetation-based SIF and NDVI response to the drought conditions.

Further research is warranted on the Monte Carlo model presented in this dissertation. While it has successfully captured the impact of certain parameters on emitted fluorescence, it is necessary to provide more realistic representation of the environment. For instance, while canopies are present in the generated three-dimensional scene, there is no interaction with the trunk or soil surface due to the absence of the latter. As remotely-sensed SIF is likely to be significantly

influenced by three-dimensional structure of the canopy, it would be needed to create a more realistic rendering of canopies as well as finer details such as clumping and clustering of leaves. Stems and stalks are considered negligible fluorescence sources for the purpose of this study. Further validation of the Monte Carlo model is necessary in order to identify areas (e.g. model parameterization, necessary input data) that need improvement.

References

- Al-Kaisi, M.M., Broner, I., & Colorado State University. Extension. (2009). Crop water use and growth stages. In, *Crop series Irrigation no 4 715* (p. 1 PDF (4 unnumbered pages 489 KB)). Fort Collins, Colo.: Colorado State University Extension,
- Baker, N.R. (2008). Chlorophyll fluorescence: A probe of photosynthesis in vivo. *Annual Review of Plant Biology*, 59, 89-113
- Baldocchi, D.D. (2003). Assessing the eddy covariance technique for evaluating carbon dioxide exchange rates of ecosystems: past, present and future. *Global Change Biology*, 9, 479-492
- Beer, C., Reichstein, M., Tomelleri, E., Ciais, P., Jung, M., Carvalhais, N., Rodenbeck, C., Arain, M.A., Baldocchi, D., Bonan, G.B., Bondeau, A., Cescatti, A., Lasslop, G., Lindroth, A., Lomas, M., Luyssaert, S., Margolis, H., Oleson, K.W., Rouspard, O., Veenendaal, E., Viovy, N., Williams, C., Woodward, F.I., & Papale, D. (2010). Terrestrial Gross Carbon Dioxide Uptake: Global Distribution and Covariation with Climate. *Science*, 329, 834-838
- Behrenfeld, M.J., & Milligan, A.J. (2013). Photophysiological Expressions of Iron Stress in Phytoplankton. *Annual Review of Marine Science*, Vol 5, 5, 217-246
- Bi, Y.B., & Xie, H.J. (2015). C3 Vegetation Mapping and CO2 Fertilization Effect in the Arid Lower Heihe River Basin, Northwestern China. *Remote Sensing*, 7, 16384-16397
- Bonan, G.B., Levis, S., Kergoat, L., & Oleson, K.W. (2002). Landscapes as patches of plant functional types: An integrating concept for climate and ecosystem models. *Global Biogeochemical Cycles*, 16
- Brouwer, C., & Heibloem, M. (1986). Irrigation water management: irrigation water needs. *Training manual*, 3
- Chakraborty, S., Fu, R., Wright, J.S., & Massie, S.T. (2015). Relationships between convective structure and transport of aerosols to the upper troposphere deduced from satellite observations. *Journal of Geophysical Research-Atmospheres*, 120, 6515-6536
- Churkina, G., & Running, S.W. (1998). Contrasting climatic controls on the estimated productivity of global terrestrial biomes. *Ecosystems*, 1, 206-215
- Ciais, P., Reichstein, M., Viovy, N., Granier, A., Ogee, J., Allard, V., Aubinet, M., Buchmann, N., Bernhofer, C., Carrara, A., Chevallier, F., De Noblet, N., Friend, A.D., Friedlingstein, P., Grunwald, T., Heinesch, B., Keronen, P., Knohl, A., Krinner, G., Loustau, D., Manca, G., Matteucci, G., Miglietta, F., Ourcival, J.M., Papale, D., Pilegaard, K., Rambal, S., Seufert, G., Soussana, J.F., Sanz, M.J., Schulze, E.D., Vesala, T., & Valentini, R. (2005). Europe-wide reduction in primary productivity caused by the heat and drought in 2003. *Nature*, 437, 529-533
- Cook, B.I., Ault, T.R., & Smerdon, J.E. (2015). Unprecedented 21st century drought risk in the American Southwest and Central Plains. *Science Advances*, 1
- Dai, A.G. (2013). Increasing drought under global warming in observations and models. *Nature Climate Change*, 3, 52-58
- Damm, A., Elbers, J., Erler, A., Gioli, B., Hamdi, K., Hutjes, R., Kosvancova, M., Meroni, M., Miglietta, F., Moersch, A., Moreno, J., Schickling, A., Sonnenschein, R., Udelhoven, T., van der

- Linden, S., Hostert, P., & Rascher, U. (2010). Remote sensing of sun-induced fluorescence to improve modeling of diurnal courses of gross primary production (GPP). *Global Change Biology*, *16*, 171-186
- Damm, A., Guanter, L., Paul-Limoges, E., van der Tol, C., Hueni, A., Buchmann, N., Eugster, W., Ammann, C., & Schaepman, M.E. (2015). Far-red sun-induced chlorophyll fluorescence shows ecosystem-specific relationships to gross primary production: An assessment based on observational and modeling approaches. *Remote Sensing of Environment*, *166*, 91-105
- Daumard, F., Champagne, S., Fournier, A., Goulas, Y., Ounis, A., Hanocq, J.F., & Moya, I. (2010). A Field Platform for Continuous Measurement of Canopy Fluorescence. *Ieee Transactions on Geoscience and Remote Sensing*, *48*, 3358-3368
- Dhar, O.N., & Nandargi, S. (2003). Hydrometeorological aspects of floods in India. *Natural Hazards*, *28*, 1-33
- Dorigo, W., de Jeu, R., Chung, D., Parinussa, R., Liu, Y., Wagner, W., & Fernandez-Prieto, D. (2012). Evaluating global trends (1988-2010) in harmonized multi-satellite surface soil moisture. *Geophysical Research Letters*, *39*
- Dyer, J.M. (2006). Revisiting the Deciduous Forests of Eastern North America. *Bioscience*, *56*, 341-352
- Falge, E., Baldocchi, D., Tenhunen, J., Aubinet, M., Bakwin, P., Berbigier, P., Bernhofer, C., Burba, G., Clement, R., Davis, K.J., Elbers, J.A., Goldstein, A.H., Grelle, A., Granier, A., Guomundsson, J., Hollinger, D., Kowalski, A.S., Katul, G., Law, B.E., Malhi, Y., Meyers, T., Monson, R.K., Munger, J.W., Oechel, W., Paw, K.T., Pilegaard, K., Rannik, U., Rebmann, C., Suyker, A., Valentini, R., Wilson, K., & Wofsy, S. (2002a). Seasonality of ecosystem respiration and gross primary production as derived from FLUXNET measurements. *Agricultural and Forest Meteorology*, *113*, 53-74
- Falge, E., Tenhunen, J., Baldocchi, D., Aubinet, M., Bakwin, P., Berbigier, P., Bernhofer, C., Bonnefond, J.M., Burba, G., Clement, R., Davis, K.J., Elbers, J.A., Falk, M., Goldstein, A.H., Grelle, A., Granier, A., Grunwald, T., Gudmundsson, J., Hollinger, D., Janssens, I.A., Keronen, P., Kowalski, A.S., Katul, G., Law, B.E., Malhi, Y., Meyers, T., Monson, R.K., Moors, E., Munger, J.W., Oechel, W., U, K.T.P., Pilegaard, K., Rannik, U., Rebmann, C., Suyker, A., Thorgeirsson, H., Tirone, G., Turnipseed, A., Wilson, K., & Wofsy, S. (2002b). Phase and amplitude of ecosystem carbon release and uptake potentials as derived from FLUXNET measurements. *Agricultural and Forest Meteorology*, *113*, 75-95
- Fernando, D.N., Mo, K.C., Fu, R., Pu, B., Bowerman, A., Scanlon, B.R., Solis, R.S., Yin, L., Mace, R.E., Mioduszewski, J.R., Ren, T., & Zhang, K. (2016). What caused the spring intensification and winter demise of the 2011 drought over Texas? *Climate Dynamics*, *47*, 3077-3090
- Flexas, J., Escalona, J.M., Evain, S., Gulias, J., Moya, I., Osmond, C.B., & Medrano, H. (2002). Steady-state chlorophyll fluorescence (Fs) measurements as a tool to follow variations of net CO₂ assimilation and stomatal conductance during water-stress in C₃ plants. *Physiologia Plantarum*, *114*, 231-240
- Fourty, T., & Baret, F. (1997). Vegetation water and dry matter contents estimated from top-of-the-atmosphere reflectance data: A simulation study. *Remote Sensing of Environment*, *61*, 34-45

- Frankenberg, C., Fisher, J.B., Worden, J., Badgley, G., Saatchi, S.S., Lee, J.E., Toon, G.C., Butz, A., Jung, M., Kuze, A., & Yokota, T. (2011). New global observations of the terrestrial carbon cycle from GOSAT: Patterns of plant fluorescence with gross primary productivity. *Geophysical Research Letters*, 38
- Frankenberg, C., O'Dell, C., Berry, J., Guanter, L., Joiner, J., Kohler, P., Pollock, R., & Taylor, T.E. (2014). Prospects for chlorophyll fluorescence remote sensing from the Orbiting Carbon Observatory-2. *Remote Sensing of Environment*, 147, 1-12
- Friedlingstein, P., Cox, P., Betts, R., Bopp, L., Von Bloh, W., Brovkin, V., Cadule, P., Doney, S., Eby, M., Fung, I., Bala, G., John, J., Jones, C., Joos, F., Kato, T., Kawamiya, M., Knorr, W., Lindsay, K., Matthews, H.D., Raddatz, T., Rayner, P., Reick, C., Roeckner, E., Schnitzler, K.G., Schnur, R., Strassmann, K., Weaver, A.J., Yoshikawa, C., & Zeng, N. (2006). Climate-carbon cycle feedback analysis: Results from the (CMIP)-M-4 model intercomparison. *Journal of Climate*, 19, 3337-3353
- Garofalo, G., Palermo, S., Principato, F., Theodosiou, T., & Piro, P. (2016). The Influence of Hydrologic Parameters on the Hydraulic Efficiency of an Extensive Green Roof in Mediterranean Area. *Water*, 8
- Gitelson, A.A., Peng, Y., Masek, J.G., Rundquist, D.C., Verma, S., Suyker, A., Baker, J.M., Hatfield, J.L., & Meyers, T. (2012). Remote estimation of crop gross primary production with Landsat data. *Remote Sensing of Environment*, 121, 404-414
- Govaerts, Y.M., Jacquemoud, S., Verstraete, M.M., & Ustin, S.L. (1996). Three-dimensional radiation transfer modeling in a dicotyledon leaf. *Applied Optics*, 35, 6585-6598
- Govaerts, Y.M., & Verstraete, M.M. (1998). Raytran: A Monte Carlo ray-tracing model to compute light scattering in three-dimensional heterogeneous media. *Ieee Transactions on Geoscience and Remote Sensing*, 36, 493-505
- Guan, K.Y., Berry, J.A., Zhang, Y.G., Joiner, J., Guanter, L., Badgley, G., & Lobell, D.B. (2016). Improving the monitoring of crop productivity using spaceborne solar-induced fluorescence. *Global Change Biology*, 22, 716-726
- Guanter, L., Frankenberg, C., Dudhia, A., Lewis, P.E., Gomez-Dans, J., Kuze, A., Suto, H., & Grainger, R.G. (2012). Retrieval and global assessment of terrestrial chlorophyll fluorescence from GOSAT space measurements. *Remote Sensing of Environment*, 121, 236-251
- Guanter, L., Rossini, M., Colombo, R., Meroni, M., Frankenberg, C., Lee, J.E., & Joiner, J. (2013). Using field spectroscopy to assess the potential of statistical approaches for the retrieval of sun-induced chlorophyll fluorescence from ground and space. *Remote Sensing of Environment*, 133, 52-61
- Guanter, L., Zhang, Y.G., Jung, M., Joiner, J., Voigt, M., Berry, J.A., Frankenberg, C., Huete, A.R., Zarco-Tejada, P., Lee, J.E., Moran, M.S., Ponce-Campos, G., Beer, C., Camps-Valls, G., Buchmann, N., Gianelle, D., Klumpp, K., Cescatti, A., Baker, J.M., & Griffis, T.J. (2014). Global and time-resolved monitoring of crop photosynthesis with chlorophyll fluorescence. *Proceedings of the National Academy of Sciences of the United States of America*, 111, E1327-E1333

- He, L.M., Chen, J.M., Liu, J., Mo, G., & Joiner, J. (2017). Angular normalization of GOME-2 Sun-induced chlorophyll fluorescence observation as a better proxy of vegetation productivity. *Geophysical Research Letters*, *44*, 5691-5699
- Heinsch, F.A., Zhao, M.S., Running, S.W., Kimball, J.S., Nemani, R.R., Davis, K.J., Bolstad, P.V., Cook, B.D., Desai, A.R., Ricciuto, D.M., Law, B.E., Oechel, W.C., Kwon, H., Luo, H.Y., Wofsy, S.C., Dunn, A.L., Munger, J.W., Baldocchi, D.D., Xu, L.K., Hollinger, D.Y., Richardson, A.D., Stoy, P.C., Siqueira, M.B.S., Monson, R.K., Burns, S.P., & Flanagan, L.B. (2006). Evaluation of remote sensing based terrestrial productivity from MODIS using regional tower eddy flux network observations. *Ieee Transactions on Geoscience and Remote Sensing*, *44*, 1908-1925
- Hirschi, M., Mueller, B., Dorigo, W., & Seneviratne, S.I. (2014). Using remotely sensed soil moisture for land-atmosphere coupling diagnostics: The role of surface vs. root-zone soil moisture variability. *Remote Sensing of Environment*, *154*, 246-252
- Hoerling, M., Eischeid, J., Kumar, A., Leung, R., Mariotti, A., Mo, K., Schubert, S., & Seager, R. (2014). Causes and Predictability of the 2012 Great Plains Drought. *Bulletin of the American Meteorological Society*, *95*, 269-282
- Huete, A., Justice, C., & Liu, H. (1994). Development of Vegetation and Soil Indexes for Modis-Eos. *Remote Sensing of Environment*, *49*, 224-234
- Joiner, J., Guanter, L., Lindstrot, R., Voigt, M., Vasilkov, A.P., Middleton, E.M., Huemmrich, K.F., Yoshida, Y., & Frankenberg, C. (2013). Global monitoring of terrestrial chlorophyll fluorescence from moderate-spectral-resolution near-infrared satellite measurements: methodology, simulations, and application to GOME-2. *Atmospheric Measurement Techniques*, *6*, 2803-2823
- Joiner, J., Yoshida, Y., Guanter, L., & Middleton, E.M. (2016). New methods for the retrieval of chlorophyll red fluorescence from hyperspectral satellite instruments: simulations and application to GOME-2 and SCIAMACHY. *Atmospheric Measurement Techniques*, *9*, 3939-3967
- Joiner, J., Yoshida, Y., Vasilkov, A., Schaefer, K., Jung, M., Guanter, L., Zhang, Y., Garrity, S., Middleton, E.M., Huemmrich, K.F., Gu, L., & Marchesini, L.B. (2014). The seasonal cycle of satellite chlorophyll fluorescence observations and its relationship to vegetation phenology and ecosystem atmosphere carbon exchange. *Remote Sensing of Environment*, *152*, 375-391
- Joiner, J., Yoshida, Y., Vasilkov, A.P., Middleton, E.M., Campbell, P.K.E., Yoshida, Y., Kuze, A., & Corp, L.A. (2012). Filling-in of near-infrared solar lines by terrestrial fluorescence and other geophysical effects: simulations and space-based observations from SCIAMACHY and GOSAT. *Atmospheric Measurement Techniques*, *5*, 809-829
- Joiner, J., Yoshida, Y., Vasilkov, A.P., Yoshida, Y., Corp, L.A., & Middleton, E.M. (2011). First observations of global and seasonal terrestrial chlorophyll fluorescence from space. *Biogeosciences*, *8*, 637-651
- Jung, M., Reichstein, M., Margolis, H.A., Cescatti, A., Richardson, A.D., Arain, M.A., Arneth, A., Bernhofer, C., Bonal, D., Chen, J.Q., Gianelle, D., Gobron, N., Kiely, G., Kutsch, W., Lasslop, G., Law, B.E., Lindroth, A., Merbold, L., Montagnani, L., Moors, E.J., Papale, D., Sottocornola, M., Vaccari, F., & Williams, C. (2011). Global patterns of land-atmosphere fluxes

- of carbon dioxide, latent heat, and sensible heat derived from eddy covariance, satellite, and meteorological observations. *Journal of Geophysical Research-Biogeosciences*, 116
- Jung, M., Reichstein, M., Schwalm, C.R., Huntingford, C., Sitch, S., Ahlstrom, A., Arneeth, A., Camps-Valls, G., Ciais, P., Friedlingstein, P., Gans, F., Ichii, K., Ain, A.K.J., Kato, E., Papale, D., Poulter, B., Raduly, B., Rodenbeck, C., Tramontana, G., Viovy, N., Wang, Y.P., Weber, U., Zaehle, S., & Zeng, N. (2017). Compensatory water effects link yearly global land CO₂ sink changes to temperature. *Nature*, 541, 516-520
- Justice, C.O., Eck, T.F., Tanre, D., & Holben, B.N. (1991). The Effect of Water-Vapor on the Normalized Difference Vegetation Index Derived for the Sahelian Region from Noaa Avhrr Data. *International Journal of Remote Sensing*, 12, 1165-1187
- Kautsky, H., & Hirsch, A. (1931). Energy transformations in boundary layers, IV. Announcement.: Interaction between excited pigment molecules and oxygen. *Berichte Der Deutschen Chemischen Gesellschaft*, 64, 2677-2683
- Kohler, P., Guanter, L., & Joiner, J. (2015). A linear method for the retrieval of sun-induced chlorophyll fluorescence from GOME-2 and SCIAMACHY data. *Atmospheric Measurement Techniques*, 8, 2589-2608
- Krause, G.H., & Weis, E. (1991). Chlorophyll Fluorescence and Photosynthesis - the Basics. *Annual Review of Plant Physiology and Plant Molecular Biology*, 42, 313-349
- Kumar, K.K., Rajagopalan, B., & Cane, M.A. (1999). On the weakening relationship between the Indian monsoon and ENSO. *Science*, 284, 2156-2159
- Lee, J.E., Berry, J.A., Van der Tol, C.S., Yang, X., Guanter, L., Damm, A., Baker, I., & Frankenberg, C. (2015). Simulations of chlorophyll fluorescence incorporated into the Community Land Model version 4. *Global Change Biology*, 21, 3469-3477
- Lee, J.E., Frankenberg, C., van der Tol, C., Berry, J.A., Guanter, L., Boyce, C.K., Fisher, J.B., Morrow, E., Worden, J.R., Asefi, S., Badgley, G., & Saatchi, S. (2013). Forest productivity and water stress in Amazonia: observations from GOSAT chlorophyll fluorescence. *Proceedings of the Royal Society B-Biological Sciences*, 280
- Leff, B., Ramankutty, N., & Foley, J.A. (2004). Geographic distribution of major crops across the world. *Global Biogeochemical Cycles*, 18
- Liao, C., & Zhuang, Q.L. (2015). Reduction of Global Plant Production due to Droughts from 2001 to 2010: An Analysis with a Process-Based Global Terrestrial Ecosystem Model. *Earth Interactions*, 19
- Livneh, B., & Hoerling, M.P. (2016). The Physics of Drought in the US Central Great Plains. *Journal of Climate*, 29, 6783-6804
- MacBean, N., Maignan, F., Bacour, C., Lewis, P., Peylin, P., Guanter, L., Kohler, P., Gomez-Dans, J., & Disney, M. (2018). Strong constraint on modelled global carbon uptake using solar-induced chlorophyll fluorescence data (vol 8, 1973, 2018). *Scientific Reports*, 8
- Mao, J.F., Thornton, P.E., Shi, X.Y., Zhao, M.S., & Post, W.M. (2012). Remote Sensing Evaluation of CLM4 GPP for the Period 2000-09. *Journal of Climate*, 25, 5327-5342

- Maxwell, K., & Johnson, G.N. (2000). Chlorophyll fluorescence - a practical guide. *Journal of Experimental Botany*, 51, 659-668
- Mena-Petite, A., Gonzalez-Moro, B., Gonzalez-Murua, C., Lacuesta, M., & Munoz-Rueda, A. (2000). Sequential effects of acidic precipitation and drought on photosynthesis and chlorophyll fluorescence parameters of *Pinus radiata* d. don seedlings. *Journal of Plant Physiology*, 156, 84-92
- Meroni, M., Picchi, V., Rossini, M., Cogliati, S., Panigada, C., Nali, C., Lorenzini, G., & Colombo, R. (2008). Leaf level early assessment of ozone injuries by passive fluorescence and photochemical reflectance index. *International Journal of Remote Sensing*, 29, 5409-5422
- Meroni, M., Rossini, M., Guanter, L., Alonso, L., Rascher, U., Colombo, R., & Moreno, J. (2009). Remote sensing of solar-induced chlorophyll fluorescence: Review of methods and applications. *Remote Sensing of Environment*, 113, 2037-2051
- Monteith, J.L. (1972). Solar-Radiation and Productivity in Tropical Ecosystems. *Journal of Applied Ecology*, 9, 747-766
- Myneni, R.B., Nemani, R.R., & Running, S.W. (1997). Estimation of global leaf area index and absorbed par using radiative transfer models. *Ieee Transactions on Geoscience and Remote Sensing*, 35, 1380-1393
- Nemani, R.R., Keeling, C.D., Hashimoto, H., Jolly, W.M., Piper, S.C., Tucker, C.J., Myneni, R.B., & Running, S.W. (2003). Climate-driven increases in global terrestrial net primary production from 1982 to 1999. *Science*, 300, 1560-1563
- Nicolai-Shaw, N., Hirschi, M., Mittelbach, H., & Seneviratne, S.I. (2015). Spatial representativeness of soil moisture using in situ, remote sensing, and land reanalysis data. *Journal of Geophysical Research-Atmospheres*, 120
- North, P.R.J. (1996). Three-dimensional forest light interaction model using a Monte Carlo method. *Ieee Transactions on Geoscience and Remote Sensing*, 34, 946-956
- Plascyk, J.A., & Gabriel, F.C. (1975). Fraunhofer Line Discriminator Mkii - Airborne Instrument for Precise and Standardized Ecological Luminescence Measurement. *Ieee Transactions on Instrumentation and Measurement*, 24, 306-313
- Porcar-Castell, A., Tyystjarvi, E., Atherton, J., van der Tol, C., Flexas, J., Pfundel, E.E., Moreno, J., Frankenberg, C., & Berry, J.A. (2014). Linking chlorophyll a fluorescence to photosynthesis for remote sensing applications: mechanisms and challenges. *Journal of Experimental Botany*, 65, 4065-4095
- Pratola, C., Barrett, B., Gruber, A., & Dwyer, E. (2015). Quality Assessment of the CCI ECV Soil Moisture Product Using ENVISAT ASAR Wide Swath Data over Spain, Ireland and Finland. *Remote Sensing*, 7, 15388-15423
- Pratola, C., Barrett, B., Gruber, A., Kiely, G., & Dwyer, E. (2014). Evaluation of a Global Soil Moisture Product from Finer Spatial Resolution SAR Data and Ground Measurements at Irish Sites. *Remote Sensing*, 6, 8190-8219
- Rosema, A., Verhoef, W., Schroote, J., & Snel, J.F.H. (1991). Simulating Fluorescence Light Canopy Interaction in Support of Laser-Induced Fluorescence Measurements. *Remote Sensing of Environment*, 37, 117-130

- Running, S.W., & Nemani, R.R. (1988). Relating Seasonal Patterns of the Avhrr Vegetation Index to Simulated Photosynthesis and Transpiration of Forests in Different Climates. *Remote Sensing of Environment*, 24, 347-367
- Running, S.W., Nemani, R.R., Heinsch, F.A., Zhao, M.S., Reeves, M., & Hashimoto, H. (2004). A continuous satellite-derived measure of global terrestrial primary production. *Bioscience*, 54, 547-560
- Schwalm, C.R., Williams, C.A., Schaefer, K., Arneeth, A., Bonal, D., Buchmann, N., Chen, J.Q., Law, B.E., Lindroth, A., Luysaert, S., Reichstein, M., & Richardson, A.D. (2010). Assimilation exceeds respiration sensitivity to drought: A FLUXNET synthesis. *Global Change Biology*, 16, 657-670
- Seager, R., Goddard, L., Nakamura, J., Henderson, N., & Lee, D.E. (2014). Dynamical Causes of the 2010/11 Texas-Northern Mexico Drought*. *Journal of Hydrometeorology*, 15, 39-68
- Sheffield, J., & Wood, E.F. (2008). Projected changes in drought occurrence under future global warming from multi-model, multi-scenario, IPCC AR4 simulations. *Climate Dynamics*, 31, 79-105
- Sitch, S., Huntingford, C., Gedney, N., Levy, P.E., Lomas, M., Piao, S.L., Betts, R., Ciais, P., Cox, P., Friedlingstein, P., Jones, C.D., Prentice, I.C., & Woodward, F.I. (2008). Evaluation of the terrestrial carbon cycle, future plant geography and climate-carbon cycle feedbacks using five Dynamic Global Vegetation Models (DGVMs). *Global Change Biology*, 14, 2015-2039
- Sitch, S., Smith, B., Prentice, I.C., Arneeth, A., Bondeau, A., Cramer, W., Kaplan, J.O., Levis, S., Lucht, W., Sykes, M.T., Thonicke, K., & Venevsky, S. (2003). Evaluation of ecosystem dynamics, plant geography and terrestrial carbon cycling in the LPJ dynamic global vegetation model. *Global Change Biology*, 9, 161-185
- Sivakumar, M.V.K., Wilhite, D.A., Pulwarty, R.S., & Stefanski, R. (2014). The High-Level Meeting on National Drought Policy. *Bulletin of the American Meteorological Society*, 95, Es85-Es88
- Soukharev, B.E., & Hood, L.L. (2006). Solar cycle variation of stratospheric ozone: Multiple regression analysis of long-term satellite data sets and comparisons with models. *Journal of Geophysical Research-Atmospheres*, 111
- Stagge, J.H., Tallaksen, L.M., Gudmundsson, L., Van Loon, A.F., & Stahl, K. (2015). Candidate Distributions for Climatological Drought Indices (SPI and SPEI). *International Journal of Climatology*, 35, 4027-4040
- Sun, K., Liu, X., Nowlan, C.R., Cai, Z., Chance, K., Frankenberg, C., Lee, R.A.M., Pollock, R., Rosenberg, R., & Crisp, D. (2017a). Characterization of the OCO-2 instrument line shape functions using on-orbit solar measurements. *Atmospheric Measurement Techniques*, 10, 939-953
- Sun, Y., Frankenberg, C., Wood, J.D., Schimel, D.S., Jung, M., Guanter, L., Drewry, D.T., Verma, M., Porcar-Castell, A., Griffis, T.J., Gu, L., Magney, T.S., Kohler, P., Evans, B., & Yuen, K. (2017b). OCO-2 advances photosynthesis observation from space via solar-induced chlorophyll fluorescence. *Science*, 358

- Sun, Y., Fu, R., Dickinson, R., Joiner, J., Frankenberg, C., Gu, L.H., Xia, Y.L., & Fernando, N. (2015). Drought onset mechanisms revealed by satellite solar-induced chlorophyll fluorescence: Insights from two contrasting extreme events. *Journal of Geophysical Research-Biogeosciences*, *120*, 2427-2440
- Tucker, C.J., & Sellers, P.J. (1986). Satellite Remote-Sensing of Primary Production. *International Journal of Remote Sensing*, *7*, 1395-1416
- Turner, D.P., Ritts, W.D., Cohen, W.B., Maeirsperger, T.K., Gower, S.T., Kirschbaum, A.A., Running, S.W., Zhao, M.S., Wofsy, S.C., Dunn, A.L., Law, B.E., Campbell, J.L., Oechel, W.C., Kwon, H.J., Meyers, T.P., Small, E.E., Kurc, S.A., & Gamon, J.A. (2005). Site-level evaluation of satellite-based global terrestrial gross primary production and net primary production monitoring. *Global Change Biology*, *11*, 666-684
- Turner, D.P., Ritts, W.D., Zhao, M.S., Kurc, S.A., Dunn, A.L., Wofsy, S.C., Small, E.E., & Running, S.W. (2006). Assessing interannual variation in MODIS-based estimates of gross primary production. *Ieee Transactions on Geoscience and Remote Sensing*, *44*, 1899-1907
- van der Tol, C., Verhoef, W., & Rosema, A. (2009). A model for chlorophyll fluorescence and photosynthesis at leaf scale. *Agricultural and Forest Meteorology*, *149*, 96-105
- Verhoef, W. (1984). Light-Scattering by Leaf Layers with Application to Canopy Reflectance Modeling - the Sail Model. *Remote Sensing of Environment*, *16*, 125-141
- Vicente-Serrano, S.M., Begueria, S., Lorenzo-Lacruz, J., Camarero, J.J., Lopez-Moreno, J.I., Azorin-Molina, C., Revuelto, J., Moran-Tejeda, E., & Sanchez-Lorenzo, A. (2012). Performance of Drought Indices for Ecological, Agricultural, and Hydrological Applications. *Earth Interactions*, *16*
- Wagle, P., Xiao, X.M., & Suyker, A.E. (2015). Estimation and analysis of gross primary production of soybean under various management practices and drought conditions. *Isprs Journal of Photogrammetry and Remote Sensing*, *99*, 70-83
- Wagle, P., Xiao, X.M., Torn, M.S., Cook, D.R., Matamala, R., Fischer, M.L., Jin, C., Dong, J.W., & Biradar, C. (2014). Sensitivity of vegetation indices and gross primary production of tallgrass prairie to severe drought. *Remote Sensing of Environment*, *152*, 1-14
- Wagle, P., Zhang, Y., Jin, C., & Xiao, X. (2016). Comparison of solar-induced chlorophyll fluorescence, light-use efficiency, and process-based GPP models in maize. *Ecological Applications*, *26*, 1211-1222
- Wagner, W., Hahn, S., Gruber, A., & Dorigo, W. (2012). Identification of Soil Moisture Retrieval Errors: Learning from the Comparison of Smos and Ascet. *2012 Ieee International Geoscience and Remote Sensing Symposium (Igarss)*, 3795-3798
- Walther, S., Voigt, M., Thum, T., Gonsamo, A., Zhang, Y., Kohler, P., Jung, M., Varlagin, A., & Guanter, L. (2016). Satellite chlorophyll fluorescence measurements reveal large-scale decoupling of photosynthesis and greenness dynamics in boreal evergreen forests. *Glob Chang Biol*, *22*, 2979-2996
- Wang, G.L. (2005). Agricultural drought in a future climate: results from 15 global climate models participating in the IPCC 4th assessment. *Climate Dynamics*, *25*, 739-753

- Wang, L.H., Jacques, S.L., & Zheng, L.Q. (1995). Mcml - Monte-Carlo Modeling of Light Transport in Multilayered Tissues. *Computer Methods and Programs in Biomedicine*, 47, 131-146
- Wilhite, D.A., Sivakumar, M.V.K., & Pulwarty, R. (2014). Managing drought risk in a changing climate: The role of national drought policy. *Weather and Climate Extremes*, 3, 4-13
- Xu, M., & Hoffman, F. (2015). Evaluations of CMIP5 simulations over cropland. *Remote Sensing and Modeling of Ecosystems for Sustainability Xii*, 9610
- Yang, X., Tang, J.W., Mustard, J.F., Lee, J.E., Rossini, M., Joiner, J., Munger, J.W., Kornfeld, A., & Richardson, A.D. (2015). Solar-induced chlorophyll fluorescence that correlates with canopy photosynthesis on diurnal and seasonal scales in a temperate deciduous forest. *Geophysical Research Letters*, 42, 2977-2987
- Yoshida, Y., Joiner, J., Tucker, C., Berry, J., Lee, J.E., Walker, G., Reichle, R., Koster, R., Lyapustin, A., & Wang, Y. (2015). The 2010 Russian drought impact on satellite measurements of solar-induced chlorophyll fluorescence: Insights from modeling and comparisons with parameters derived from satellite reflectances. *Remote Sensing of Environment*, 166, 163-177
- Zhang, Y., Xiao, X.M., Wu, X.C., Zhou, S., Zhang, G.L., Qin, Y.W., & Dong, J.W. (2017). Data Descriptor: A global moderate resolution dataset of gross primary production of vegetation for 2000-2016. *Scientific Data*, 4
- Zhao, F., Dai, X., Verhoef, W., Guo, Y.Q., van der Tol, C., Li, Y.G., & Huang, Y.B. (2016). FluorWPS: A Monte Carlo ray-tracing model to compute sun-induced chlorophyll fluorescence of three-dimensional canopy. *Remote Sensing of Environment*, 187, 385-399
- Zhao, F., Li, Y.G., Dai, X., Verhoef, W., Guo, Y.Q., Shang, H., Gu, X.F., Huang, Y.B., Yu, T., & Huang, J.X. (2015). Simulated impact of sensor field of view and distance on field measurements of bidirectional reflectance factors for row crops. *Remote Sensing of Environment*, 156, 129-142
- Zhao, M.S., Heinsch, F.A., Nemani, R.R., & Running, S.W. (2005). Improvements of the MODIS terrestrial gross and net primary production global data set. *Remote Sensing of Environment*, 95, 164-176
- Zhao, M.S., & Running, S.W. (2010). Drought-Induced Reduction in Global Terrestrial Net Primary Production from 2000 Through 2009. *Science*, 329, 940-943
- Zhou, Y., Wu, X., Ju, W., Chen, J.M., Wang, S., Wang, H., Yuan, W., Andrew Black, T., Jassal, R., Ibrom, A., Han, S., Yan, J., Margolis, H., Rouspard, O., Li, Y., Zhao, F., Kiely, G., Starr, G., Pavelka, M., Montagnani, L., Wohlfahrt, G., D'Odorico, P., Cook, D., Arain, M.A., Bonal, D., Beringer, J., Blanken, P.D., Loubet, B., Leclerc, M.Y., Matteucci, G., Nagy, Z., Olejnik, J., Paw U, K.T., & Varlagin, A. (2016). Global parameterization and validation of a two-leaf light use efficiency model for predicting gross primary production across FLUXNET sites. *Journal of Geophysical Research: Biogeosciences*, 121, 1045-1072
- Zhu, H., Lin, A., Wang, L., Xia, Y., & Zou, L. (2016). Evaluation of MODIS Gross Primary Production across Multiple Biomes in China Using Eddy Covariance Flux Data. *Remote Sensing*, 8, 395

Vita

Maryia Halubok was born in Minsk, Belarus. Upon graduation from Lyceum No. 2 in 2007 she entered the Geography Department of the Belarusian State University. She earned a B.Sc. degree in hydrometeorology from the Belarusian State University in June 2012. During the following year, she was employed as a research assistant at the National Ozone Monitoring Research Educational Center and the Scientific Research Laboratory of Limnology. In August 2013 she enrolled in a PhD program in Jackson School of Geosciences at the University of Texas at Austin to work in the fields of climate science and biogeophysics.

Permanent email address: m.halubok@gmail.com

This dissertation was typed by the author.